MASS MEASUREMENTS OF SOME PROTON-RICH NUCLEI

Thesis by
Richard Graham Miller

In Partial Fulfillment of the Requirements
For the Degree of
Doctor of Philosophy

California Institute of Technology
Pasadena, California
1966
(Submitted March 14, 1966)

ACKNOWLEDGMENTS

The author wishes to thank all the faculty and technical staff of Kellogg and Sloan Radiation Laboratories without whose help this thesis would not have been possible. Particular thanks are due to Dr. R. W. Kavanagh who is the other half of the "we" used throughout this thesis. It was a long, hard struggle, but he may finally have taught me the meaning of the word "precision". I would also like to thank Dr. W. A. Fowler who wanted to know the mass of Ni^{56} and thereby instigated this project.

This research was supported by the Office of Naval Research [Nonr - 220(47)].

ABSTRACT

The Q values and 0^{o} cross sections of (He^{3}, n) reactions forming seven proton-rich nuclei have been measured with accuracies varying from 6 to 18 keV. The Q values (in keV) are: Si^{26}(85), S^{30}(-573), Ar^{34}(-759), Ti^{42}(-2865), Cr^{48}(5550), Ni^{56}(4513) and Zn^{60}(818). At least one excited state was found for all but Ti^{42}. The first four nuclei complete isotopic spin triplets; the results obtained agree well with charge-symmetry predictions. The last three, all multiples of of the α particle, are important in the α and e-process theories of nucleo-synthesis in stars. The energy available for β decay of these three was found by magnetic spectrometer measurements of the (He^{3}, p) Q values of reactions leading to V^{48}, Co^{56} and Cu^{60}. Many excited states were seen: V^{48}(3), Co^{56}(15), Cu^{60}(23). The first two states of S^{30} are probably 0^{+} and 2^{+} from (He^{3}, n) angular distribution measurements. Two NaI γ- ray measurements are described: the decay of Ar^{34} (measured $\tau_{1/2} = 1.2 \pm 0.3$s) and the prompt γ-ray spectrum from $Fe^{54}(He^{3}, n\gamma)Ni^{56}$. Possible collective structure in Ni^{56} and Ca^{40}, both doubly magic, is discussed.

The (He^{3}, n) neutron energy and yield measurements utilized neutron-induced nuclear reactions in a silicon semiconductor detector. Cross sections for the most important detection processes, $Si^{28}(n,\alpha)Mg^{25}$ and $Si^{28}(n, p)Al^{28}$, are presented for reactions leading to the first four states of both residual nuclei for neutron energies from 7.3 to 16.4 MeV. Resolution and pulse-height anomalies associated with recoil Mg^{25} and Al^{28} ions are discussed. The 0^{o} cross section for $Be^{9}(\alpha, n)C^{12}$, used to provide calibration neutrons, has been measured with a stilbene spectrometer for $n_{o}(5.0 \leq E_{\alpha} \leq 12$ MeV), $n_{1}(4.3 \leq E_{\alpha} \leq 12.0$ MeV) and $n_{2}(6.0 \leq E_{\alpha} \leq 10.1$ MeV). Resonances seen in the n_{o} yield may correspond to nine new levels in C^{13}.

TABLE OF CONTENTS

I. INTRODUCTION

The nucleus Ni^{56} has several properties which make it unusual and particularly interesting. It is doubly magic (Z = N = 28, $f_{7/2}$ shell closure) and is the most tightly bound of all nuclei containing equal numbers of protons and neutrons. Despite its unusual nuclear stability, it beta decays to Co^{56} which in turn beta decays to Fe^{56}, nearly the most bound of all nuclei. There is a very large peak in the cosmic element abundance centered at Fe^{56} and, if one accepts the view that the elements are synthesized inside stars, one must find a mechanism to produce this peak. The α - and e - process theories of Fowler and Hoyle (1964) provide such a mechanism: In the advanced evolution of a massive star just before it becomes a supernova, Ni^{56} is made from lighter elements by α- particle capture (the α- process). Some of the Ni^{56} decays by electron capture to Co^{56} before the explosion and is rapidly transmuted to other iron group elements, including Fe^{56} (the e-process). The remainder of the Ni^{56} decays to Fe^{56} after the explosion. The result is that the relative abundances of the iron group elements are largely determined by the half life of the Ni^{56} decay. Chapter II gives a more detailed outline of these theories.

The stellar value of the Ni^{56} half life, which is much shorter than the terrestrial value because of the increased electron density at the nucleus, is mainly determined by the amount of energy available in the Ni^{56} decay i. e. the Ni^{56} - Co^{56} mass difference. The work described in this thesis began as an attempt to measure the Ni^{56} mass, the Co^{56} mass being already known. This mass had not been measured previously for two reasons: Ni^{56} is two positions from the line of stability on the proton-rich side which

makes direct study via nuclear reactions difficult, and it appears to decay entirely by electron capture (see e. g. Wells, Blatt and Meyerhof (1961)) so that β endpoint energy measurements cannot be made. According to Wells et al., the gamma rays seen following the decay indicate that electron capture proceeds to a state in Co^{56} at 1. 74 MeV with possible branches to lower-lying states. Thus the Ni^{56} - Co^{56} mass difference must be greater than 1. 74 MeV and, since no positrons are seen, cannot be much more than 2 MeV.

In our study, the mass of Ni^{56} was deduced from the Q value measured for the reaction $Fe^{54}(He^3, n)Ni^{56}$. To overcome the Coulomb barrier, the He^3 beam energy must be 10 MeV or more and the reaction Q value was estimated to be about 5 MeV. Thus it was necessary to measure the energy of a 15-MeV neutron -- too high to be able to achieve the desired resolution with neutron time-of-flight techniques.

Following a suggestion by Dr. G. Goldring, the neutron energy was measured by means of charged-particle-producing reactions induced by neutrons in the silicon of the active volume of a semiconductor detector. In this way, the problem of measuring the neutron energy was reduced to the much simpler problem of measuring a charged particle energy. However, several complications remain. The spectrum produced by a monoenergetic neutron in a semiconductor detector is very complex because of the different isotopes of silicon present, the different reactions possible with each, and the many final states populated in each residual nucleus. The strongest groups observed are due to the reactions $Si^{28}(n, \alpha)Mg^{25}$ and $Si^{28}(n, p)Al^{28}$. Cross sections for these reactions leading to the first four states of the two residual

nuclei were measured in steps of 25 to 50 keV over the neutron energy range 7.3 to 16.4 MeV. The methods involved are described in detail in Chapter IV. Also discussed are a differential pulse-height defect observed when comparing peaks from the reactions $Si^{28}(n, \alpha)Mg^{25}$ with peaks from $Si^{28}(n, p)Al^{28}$ and the anomalously poor resolution of these peaks when compared with the resolutions of α particles or protons alone.

The Ni^{56} nucleus is composed of an integral number of alpha particles (14), which is one reason for its large binding energy. Although all such nuclei possess large nuclear stability compared to their neighbors, Ca^{40} is the heaviest alpha nucleus stable against beta decay. The alpha nuclei above Mg^{24} are important stepping stones on the way to Ni^{56} in the α-process. No mass measurement had been made on one of them (Cr^{48}) nor on the first alpha nucleus above Ni^{56} (Zn^{60}). Since both Cr^{48} and Zn^{60} could be made by (He^3, n) reactions, they were investigated using the techniques developed for the Ni^{56} measurement. The data obtained for all three nuclei were used to locate excited states and obtain an estimate of the 0^o reaction cross section as well as to measure masses.

In the course of the Zn^{60} measurements, two unknown contaminants were observed to build up on the target during bombardment. Kinematic considerations eliminated all but two elements which might reasonably be expected: Si^{28} (from O-ring grease) and S^{32} (from O-rings). However, neither the mass of S^{30} (from $Si^{28}(He^3, n)$) nor Ar^{34} (from $S^{32}(He^3, n)$) was known. Targets of O-ring grease and natural silicon were bombarded and the identification of Si^{28} as one of the contaminant peaks was confirmed. At the same time an accurate measurement of the

S^{30} mass was obtained. Next, targets of natural sulfur and Sb_2S_3 were bombarded and the mass of Ar^{34} was determined. The result was such as to preclude S^{32} being the second contaminant. The periodic table was searched again, this time (He^3, n) reactions on all stable nuclei being considered. All possibilities were eliminated kinematically except the reaction $Mg^{24}(He^3, n)Si^{26}$, but again no accurate measurement of the Si^{26} mass existed. Natural magnesium targets were bombarded and the mass of Si^{26} determined, the measurements indicating that Mg^{24} was indeed responsible for the second contaminant peak. How did it get there? It turns out that all commercial aluminum is alloyed with a small amount of magnesium ($\approx$ 1%). Further, at low pressures ($\approx 5 \times 10^{-6}$ mm Hg) and high temperatures ($\approx 500^{\circ}$ C), the magnesium may readily evaporate from the alloy. The target holder used for the Zn^{60} measurements was made of aluminum and the target was observed to become red hot under bombardment. The Ni^{56} data was obtained using the same target holder and upon re-examination also showed peaks from Si^{26} (and S^{30} too). Other accurate measurements of both the Si^{26} and S^{30} masses were published at about this time and agree well with the values found here. The search of the nuclides made while trying to identify the contaminants discussed above suggested that one more new isotope could easily be made: Ti^{42} via the reaction $Ca^{40}(He^3, n)Ti^{42}$. This was done. The four nuclei Si^{26}, S^{30}, Ar^{34} and Ti^{42} all complete isotopic spin triplets of which they are the proton-rich members. The results obtained agree well with the predictions of charge symmetry. An additional measurement was made on the $Si^{28}(He^3, n)S^{30}$ reaction: the angular distributions of neutrons to the ground and first excited states were measured in a semiconductor detector. Probable spin and parity assignments are made.

The procedure and results for all the (He^3, n) measurements are given in Chapter V. One detail of the procedure should be mentioned here: The reaction $Be^9(\alpha, n)C^{12}$ was used to provide neutrons of known energy for calibration purposes, thus avoiding the problem of absolute energy measurement. Calibration spectra obtained in this way could also be used to unfold complex spectra by subtracting out the family of peaks associated with each neutron group, starting with the group of highest energy. Many excited states were found by this method.

As well as being used for energy calibration purposes, the $Be^9(\alpha, n)C^{12}$ reaction was used to provide 10.6 to 16.4-MeV neutrons for the semiconductor-detector-efficiency measurements (see Chapter IV, section 4). For these reasons, it was investigated in some detail. Absolute cross sections at 0^o were measured for n_o, n_1, and n_2 over most of the bombarding energy range of 4 to 12 MeV using a stilbene crystal as the neutron detector. The n_o yield curve has prominent resonances which may correspond to up to nine new levels of C^{13}. These measurements are described in Chapter II.

As already mentioned, one of the most important parameters in the e-process theory is the Ni^{56} - Co^{56} mass difference. With this in mind, it was decided to check the Co^{56} mass, a measurement which could be made with the reaction $Fe^{54}(He^3, p)Co^{56}$ using the same target material and even the same targets as used for the Ni^{56} experiment. Fifteen excited states of Co^{56} were found, most of them verifying earlier work. At the same time mass and level measurements were made on Cu^{60} and V^{48} which are the β-decay daughters of Zn^{60} and Cr^{48}, the other two alpha nuclei whose masses had been measured. Twenty-three levels were seen

in Cu^{60}, all previously unreported. The (He^3, p) measurements are described in Chapter VI.

The last chapter, Chapter VII, describes two gamma-ray measurements. First, the half life of Ar^{34} was found, a measurement made possible by the discovery of an allowed β-decay branch to the 0.67-MeV level of Cl^{34} which takes place in addition to the superallowed transition to the ground state of Cl^{34}. Second, the prompt gamma-ray spectrum from the reaction $Fe^{54}(He^3, n)Ni^{56}$ was measured and the gamma rays seen identified with levels of Ni^{56} found in the (He^3, n) Q-value measurements. The data are consistent with a collective interpretation of the levels of Ni^{56} discussed in section 4 of the chapter.

Before the $Fe^{54}(He^3, n)$ reaction was tried, attempts were made to produce Ni^{56} with reactions using a heavy ion beam of either Ne^{20} or S^{32}. To get a beam of high enough energy to surmount the Coulomb barriers involved, it was first necessary to produce a negatively-charged beam from the negative ion source of the ONR-CIT tandem. These attempts were not successful but some useful information about heavy-ion-beam production was obtained and is given in appendix 2.

II. ASTROPHYSICS AND Ni^{56}

The importance of Ni^{56} to astrophysics can best be explained by giving a brief life history of a massive star (mass thirty times that of the sun) as envisioned by Fowler and Hoyle (1964). The star comes into existence through the condensation of a large gas cloud, composed mostly of hydrogen, and is slowly warmed by the release of gravitational energy. Neglecting radiation pressure, exactly one half the gravitational energy released is radiated away and the other half converted into internal energy.

After about 3×10^5 years, the temperature near the center of the cloud becomes so high that protons there have sufficient kinetic energy to undergo nuclear reactions. Hydrogen is transformed to helium with the release of energy. Gravitational contraction ceases and the core temperature remains essentially constant (about 4×10^7 degrees) until all the hydrogen is converted to helium, a process which takes about 3×10^7 years. When the hydrogen is exhausted, the core again shrinks, warming further as it does so. At a temperature of about 2×10^8 degrees, helium burning commences and the core is converted to O^{16}, a process taking about 3×10^5 years. Further contraction and heating take place and in about one day the oxygen is burned by nuclear fusion reactions at a temperature of about 2×10^9 degrees to form heavier nuclei, primarily S^{32}.

Up to this point, the nuclear evolution of the star has been cyclic in character. As long as a particular fuel is being burned, the star remains quite stable in gross structure. Small changes in the physical condition of the star's core regulate the nuclear energy generation rate so that it just balances radiation losses. In the brief interval between fuels, energy balance is maintained by gravitational

contraction which also increases the core temperature to the point where the product of the last process can become the fuel of the next. A fuel is first exhausted in the core of the star where the temperature is highest; the same fuel continues to be burned in a shell around the core even after the core has switched to a heavier fuel.

During oxygen burning, two qualitatively new features become important: energy loss by neutrino emission and photodisintegration reactions. Anytime a neutrino is produced, it is almost certain to escape from the star without further interaction. Such an energy loss must be made up by an increase in the nuclear reaction rate. The CVC theory suggests the existence of the reaction $e^+ + e^- \rightarrow \nu + \bar{\nu}$ and allows one to calculate the rate, a calculation which shows that this reaction, if it exists, is by far the most important source of neutrinos in massive stars at high temperatures and that its rate increases very rapidly with temperature. At temperatures above 5×10^8 degrees, neutrino losses exceed photon losses and in fact shorten the oxygen burning time scale by a factor of 10^7. Almost all the nuclear energy generated is now being used to balance the neutrino loss and this loss rate will therefore determine the evolutionary time scale.

The second new feature is that at the higher temperatures now present many electromagnetic photons will have energies high enough to produce photodissociation reactions. Toward the end of oxygen burning ($T = 2.5 \times 10^9$ degrees), some of the S^{32} produced will be photodisintegrated, primarily by (γ, p) reactions but occasionally by (γ, α) or (γ, n) reactions. The residual nuclei are rapidly broken down by further (γ, n) and (γ, p) reactions to Si^{28}, a nucleus which is too stable to photodisintegrate at the prevailing

temperature. The protons and neutrons released recombine into α particles because of the large energy release. These, in turn, are captured by S^{32} to form Ar^{36}. The total effect is summed up by

$$2S^{32} \rightarrow Si^{28} + Ar^{36} - 0.31 \text{ MeV}$$

and forms a slight energy drain on the star. The reverse reaction also occurs and the system comes into equilibrium with the number density of S^{32} approximately equal to that of $Si^{28} + Ar^{36}$. Note that S^{32} and Ar^{36} can exist only because Si^{28} is stable against photodisintegration. Small amounts of Ca^{40} and Ti^{44} may also be made by α capture but the temperature is not high enough for this to be very significant. This cycle of reactions marks the first step of the α-process.

After oxygen burning, the core contracts until a temperature is reached ($\approx 3 \times 10^9$ degrees) at which Si^{28} is photodisintegrated and is effectively transformed into $Mg^{24} + \alpha$. The Mg^{24} lifetime to effective α-particle loss is less than 10% that of Si^{28}; Ne^{20}, O^{16} and C^{12} have even shorter lifetimes and Be^8 is spontaneously unstable. Thus, once the Si^{28} structure is broken, it is almost immediately transformed into seven α particles. Most of these α particles will be captured by the remaining heavy nuclei to form heavier nuclei and the center of the mass distribution will shift to ever-higher values of atomic weight. Although the analogy is not very accurate, one could view the core of the star as being a vast sea of α particles making up a Maxwell - Boltzmann statistical ensemble. The α particles will group into clusters (nuclei) of varying size, the number of clusters of a given size being

proportional to exp(B/kT) where B is the binding energy of the cluster. Of course the clusters are being continually broken up by photodissociation reactions but there will be some equilibrium distribution determined by the Boltzmann factor. That combination of α particles which has the most binding energy per nucleon (and is therefore most abundantly produced) is Ni^{56}. Thus the main effect of the α-process may be summed up as

$$2Si^{28} \rightarrow Ni^{56} + 11.0 \text{ MeV} .$$

The very complicated chain of reactions implied by this expression produces enough energy to maintain stellar equilibrium but the neutrino drain is so great at the existing temperatures ($3 - 3.5 \times 10^9$ degrees) that the fuel is exhausted in about one hour.

At this point, energy generation by nuclear reactions ceases since Ni^{56} has the maximum binding energy per nucleon in a medium in which the number of protons and neutrons is equal. One source of energy remains: the beta decay of the heavier elements to the line of stability, in particular the transformation of ${}_{28}Ni^{56}_{28}$ to the more tightly bound isobar, ${}_{27}Co^{56}_{29}$. After slight core contraction, the temperature rises to 3.8×10^9 degrees and this and subsequent reactions are able to maintain equilibrium. This is the e-process.

On earth, Ni^{56} decays to Co^{56} by electron capture with a half life of 6.1 days. In the stellar core, the electron density at the nucleus is much greater than on earth because of the high temperature and pressure so that the decay rate is greatly enhanced (by a factor of about 300 for our particular star). Once Co^{56} is formed, it is immediately transmuted to more stable nuclei by rapid nuclear reactions e. g. ,

$$2Co^{56} \rightarrow Fe^{54} + Ni^{58} + 4.45 \text{ MeV}.$$

These two nuclei, although both stable, can capture electrons to form Mn^{54} and Co^{58} which in turn are immediately transmuted to more stable nuclei e. g..

$$2Fe^{54} + 2e^{-} \rightarrow 2Mn^{54} - 1.39 \text{ MeV} \rightarrow Cr^{52} + Fe^{56} + 3.53 \text{ MeV}$$
(net release),

$$2Ni^{58} + 2e^{-} \rightarrow 2Co^{58} - 0.78 \text{ MeV} \rightarrow Fe^{56} + Ni^{60} + 4.62 \text{ MeV}$$
(net release)

and so on.

Once the stellar core has converted to Fe^{56}, its nuclear energy reserves are nearly exhausted. The attempt to balance neutrino energy losses by core contraction only brings on a worse fate: at temperatures above 4×10^{9} degrees, the Fe^{56} is photodisintegrated, first into α particles and neutrons and finally into protons and neutrons. Gravitational contraction can provide no where near enough energy to balance this enormous energy drain. The inner core goes into free fall and completely implodes in less than a second. The mantle and envelope of the star explode soon thereafter. The result - a supernova. Much of the stellar material immediately outside the imploded inner core will be expelled from the star. It will have undergone the e-process but will not have suffered photodisintegration. The implosive instability, once started, develops so rapidly that there is insufficient time for it to consume the whole core. This ejected material (about two solar masses) is presumably the source of the large peak in cosmic element abundance centered at Fe^{56}.

Two tests of the theory immediately suggest themselves:

1) Can the α- and e-processes produce the correct relative abundances of the elements in the iron group?
2) If the answer to 1) is "yes" (it is), is there sufficient time for the e-process to operate before the star blows up?

This second question is considerably more complicated. The time available for the e-process to operate is set by the neutrino loss rate and is about 6000 sec for the star being considered. The rate of the e-process is largely determined by the rate of the $Ni^{56} \rightarrow Co^{56}$ electron capture. This in turn depends sensitively on the Ni^{56} - Co^{56} mass difference, a number which was not experimentally available when Fowler and Hoyle first performed their calculations. Using nuclear and beta decay systematics, they guessed a value of 2.1 MeV. The initial stimulus for the work described in this thesis was to measure this value. In Chapters V and VI, experiments are described in which it was found to be 2.115 ± 0.017 MeV - amazingly close to the original guess! This mass difference leads to a mean electron capture life time, τ, of 2700 sec for the ground state of Ni^{56} in the e-process. The presence of a state in Ni^{56} at 2.69 MeV which is probably 2^+ may enhance the decay by 20-50%. Fowler and Hoyle adopted $\tau = 2000$ sec.

The influence of this number on the relative abundances of the iron group elements may be seen in the following way. Suppose the Ni^{56} lifetime were very long (several days). Then very little Ni^{56} would decay before the star exploded. The expelled material cools very rapidly and all nuclear reactions cease. Thus the Ni^{56} beta decays entirely to Fe^{56}. The result would be a very sharp peak in the abundance curve at Fe^{56}, and Fe^{56} only, contrary to observation. A very short Ni^{56} lifetime (a few seconds) would produce a different effect. There would be enough time before the explosion

for electron captures and subsequent fast nuclear reactions to move the nuclear material to positions of greater neutron excess and slightly greater stability e. g., the relative abundance of Fe^{58} (which is slightly more stable than Fe^{56}) would increase relative to Fe^{56}. On the other hand, if the Ni^{56} mean life were about equal to the time available for the e-process to operate, there would be a sharp fall in the final Fe^{56} abundance and a sharp rise in the abundances of elements such as Fe^{54} and Ni^{58} (see reactions given above). Using this chain of reasoning and some computer calculations performed by Clifford and Tayler (1965), Fowler and Hoyle made estimates of the final relative abundances of the different isotopes of iron as a function of the time available for electron capture using the calculated Ni^{56} lifetime. Their calculations reproduce the cosmic abundance curve if the time available for electron captures is 3.2×10^4 sec. This is about five times longer than the time given above for the operation of the e-process. However, the two time scales can be brought into agreement in a variety of ways e. g., by assuming the e-process material responsible for the iron group elements to have come from stars slightly less massive than the thirty-solar-mass star assumed in the calculation or by making reasonable (and small) changes in the model of the physical structure of the star.

III. THE REACTION $Be^9(\alpha, n)C^{12}$

1. Introduction

The reaction $Be^9(\alpha, n)C^{12}$ (Q = 5.704 MeV) is a convenient source of fast neutrons for calibration purposes. The neutron group leading to the ground state of C^{12} is well separated in energy from the neutron group leading to the first excited state (at 4.43-MeV excitation) and the gamma ray from the decay of this state is the only gamma ray present. Pure targets are readily available since beryllium is monoisotopic and are easily made using standard bell-jar evaporation techniques. Furthermore, the targets are quite rugged whether used as self-supporting foils or on thick backings.

This chapter reports 0^o cross-section measurements performed with a stilbene detector for the production of the first three levels of C^{12}: $Be^9(\alpha, n_o)C^{12}$ (gnd) for $5.0 \leq E_\alpha \leq 12.0$ MeV (section 4.1); $Be^9(\alpha, n_1)C^{12}$ (4.43) for $4.3 \leq E_\alpha \leq 12.0$ MeV (section 4.2); and $Be^9(\alpha, n_2)C^{12}$ (7.66) for $6.0 \leq E_\alpha \leq 10.1$ MeV (section 4.3). Deduced levels in C^{13} are given in section 4.4.

2. Procedure

The neutron and gamma-ray yield at 0^o was measured in a stilbene crystal for alpha-particle bombarding energies from 4 to 12 MeV. From the spectra obtained, it was possible to deduce the neutron yield to the ground state of C^{12} from 5 to 12 MeV and the neutron yield to the first and second excited states of C^{12} over much of the same range, although with much less precision. The step size was 100 keV except in the region of a narrow resonance at 11.70 MeV where the step size was reduced to 25 keV. The

ONR-CIT tandem accelerator was used to provide an α^{++} beam magnetically analyzed to a precision of 0.2%. Targets were made by evaporation of Be^9 onto tungsten backings 0.018 cm thick. Target thickness was determined using a magnetic spectrometer to measure the difference in energies of 1-MeV protons scattered from the tungsten backing with and without penetration through the beryllium layer. See figure 21 for two typical target thickness measurements. The entire yield curve was measured with targets of two different thicknesses: 40 ± 8 $\mu g/cm^2$ and 88 ± 14 $\mu g/cm^2$.

The stilbene crystal used was cylindrical, 3.81 cm in diameter and 3.81 cm long. It was located at 0^o with respect to the beam axis with its front face 5.71 cm from the target. The crystal was mounted on a phototube-preamplifier combination whose output was connected to the internal amplifier of a 400-channel pulse-height analyzer.

3. Analysis of the stilbene spectra

A typical spectrum is shown in figure 1. Neutrons are detected indirectly in stilbene ($C_6 H_5 CH CH C_6 H_5$) through elastic collisions with protons so that each neutron group of discrete energy is represented in the spectrum by a continuous distribution of protons from zero energy to the full neutron energy, all proton energies occurring with approximately equal probability. Thus, one might expect a monoenergetic neutron to produce a rectangular-shaped spectrum in stilbene as recorded in a multichannel analyzer (equal number of counts in all channels up to the channel number corresponding to the incident neutron energy and no counts thereafter). However, the light output of stilbene is a non-linear function of proton energy, low-energy protons being less effective light

producers. Thus, instead of being flat, the spectrum slowly rises as one goes toward lower channels. Swartz and Owen (1960) present tables from which the detection efficiency and spectrum shape for a monoenergetic neutron may be calculated. They also give a detailed description of the use of organic scintillators, in particular stilbene, for the detection of neutrons by their proton recoils.

Gamma rays are also detected in a stilbene crystal, again indirectly, through processes which transfer energy to electrons, primarily Compton scattering in the energy range of interest here. In figure 1, the double-peaked structure near channel 80 was produced by the 4.43-MeV gamma ray of C^{12}. The upper peak is the Compton edge of the gamma ray and the lower peak is due to conversion of the gamma ray into an electron pair which is totally stopped in the crystal, but with loss of both annihilation quanta. The light output of stilbene is a nearly linear function of electron energy and is considerably larger than the light output for a proton of the same energy. For example, pulses from the Compton edge of the 4.43-MeV gamma ray have about the same amplitude as pulses produced by a 9.7-MeV proton.

We have used two methods for obtaining absolute neutron yield from the observed proton pulse-height distributions. The first of these, the integral - sum method, was used to analyze all the n_o data and part of the n_1 data. The second, the initial-step-height method, was used to analyze the n_2 data.

3.1. The integral-sum method

The raw spectra for the entire neutron energy range examined were used to obtain a graph of channel number vs. proton-recoil energy, assuming that the channel number of the half-height point on the shoulder at the end of the proton recoil group (channel 117.8 for n_o in figure 1) corresponds to a proton energy equal to the incident neutron energy. Next, for each spectrum, the sum of all counts above a fixed channel, corresponding to an energy E_c (channel 105 for n_o in figure 1, corresponding to a proton energy of 10.23 MeV), was found. From this, the number of ground-state neutrons per steradian at 0^o could be calculated by multiplying by $E_n/(4\pi(E_n - E_c)\epsilon)$ where E_n is the incident neutron energy and ϵ is the detection efficiency calculated using table I from the article by Swartz and Owen. Figure 2 shows a plot of detection efficiency vs. neutron energy for the particular geometry used in this experiment. A sample calculation of the absolute cross section is given in the caption of figure 1.

When finding the n_1 yield by this method, we had first to allow for the underlying n_o structure. This was done by fitting the theoretical shape of the n_o distribution (which was calculated using table III with kB = 0.0120 from Swartz and Owen's article) to the visible portion of the curve and subtracting n_o from beneath n_1. The n_1 yield was then determined precisely as above. This method of analysis avoids problems due to the front edges of the pulse-height distributions being not well defined and is also amenable to computer programming.

The validity of the integral-sum method of analysis depends upon three assumptions:

i) The n-p scattering cross section is isotropic in the center-of-mass system. This is certainly true for low-energy neutrons but the distribution becomes anisotropic as the neutron energy is increased although at first remaining roughly symmetrical about 90^{o} (CM). For 17-MeV neutrons (the maximum energy of interest here), the anisotropy (ratio of 0^{o} to 90^{o} cross sections in the CM) is about 1.07 according to Gammel (1960), but the effect on the integral sum is always smaller and has been neglected. (It amounts to about 5% for the 17-MeV point.)

ii) All of the recoil protons are stopped in the crystal. Actually, some recoil protons produced near the edges of the crystal will escape, thus moving some counts from high channels to low channels. The effect becomes more serious as the neutron energy is increased. For 17-MeV neutrons and for the E_c chosen, this effect results in the integral sum being about 7% low. It is nearly cancelled by the artificial increase in the number of counts resulting from neglecting the effects of anisotropy.

iii) Neutrons are detected entirely by single-scatter events. Double-scatter events are of two types: a neutron may scatter first from carbon (an event which by itself, produces too small a light pulse for us to have detected) and then from hydrogen; or a neutron may double-scatter from hydrogen. The first type of event may change the detection efficiency but will not seriously affect the spectrum shape; the second moves events from low channels to high channels. For the n_o group of figure 1 and for the cut-off energy chosen, the integral sum contains less than a 5% contribution from carbon-hydrogen scattering and less than a 10% contribution from counts moved into the summed region by hydrogen-hydrogen scattering. Both these effects have been neglected because of the difficulty in computing them exactly.

It has been found empirically (see e. g., Swartz and Owen) that the single-scatter detection efficiency calculated assuming no carbon scattering events is slightly larger and is closer to the true multiple-scatter detection efficiency i. e., this calculation accounts fairly accurately for events in which a neutron is scattered first from carbon and then from hydrogen. The physical meaning of this observation is that the effective path length of the neutron in the crystal is little affected by carbon scattering events. However, this argument is useful only when analysis is based on the full recoil-proton spectrum (which was not possible with our data) because carbon scattering lowers the neutron energy and therefore changes the shape of the spectrum. Figure 2 shows plots of the single-scatter detection efficiency allowing for attenuation of the primary neutron beam by both carbon and hydrogen (the efficiency curve used here), and hydrogen scattering only.

Broek and Anderson (1960) have derived an approximate expression which corrects the initial step height of the proton recoil distribution for both double scattering from hydrogen and edge effects. For our crystal, the correction factors are 1. 07, 1. 03 and 0. 995 respectively for 5-MeV, 10-MeV and 15-MeV incident neutrons, giving us some justification for neglecting wall effects and double scatter from hydrogen. Note that double scatter from carbon and the effects of an anisotropic n-p scattering cross section are not included in their expression.

3. 2. The initial-step-height method

The distortion of the spectrum produced by multiple-scattering events increases as the neutron energy is decreased because the detection efficiency is increasing. Thus the integral-

sum method becomes of dubious validity for "low" energy neutrons to a degree that is determined by the shape and size of stilbene crystal used. For our crystal, we have assumed the integral-sum method to be valid down to a neutron energy of about 10.5 MeV; distortions of the spectrum due to multiple scattering become plainly visible at lower neutron energies.

A possible way to avoid many of the difficulties introduced by multiple scattering is based on the following properties. The non-linear response of stilbene results in a proton of given energy producing a larger pulse than two protons in coincidence with the same total energy. Also, the neutron energy is lowered 15% on the average in a carbon-scattering event, the energy of the recoil carbon atom being mostly lost in a non-luminescent way. Thus the highest-energy portion of the proton-recoil spectrum should be produced predominantly by single-scatter events. The shape of the n_1 peak of figure 1 is suggestive of this interpretation. Below the shoulder, there is a short flat region, then a bump, presumably due to multiple scattering, in which the number of counts increases about 10%.

The n_2 yield was found by using the height of the peak just below the shoulder and calculating the cross section from this assuming the single-scatter efficiencies. To get the total number of counts in the distribution, the step height was multiplied by $E/(4\pi\epsilon\,\Delta E)$, where E is the incident neutron energy, ΔE the energy width of the channel just below the step and ϵ the efficiency. We call this method the initial-step-height method; its validity depends upon the same assumptions as were made for the integral-sum method.

4. Results and discussion

4.1. The n_0 yield curve

The n_0 yield curve was analyzed entirely by the integral-sum method and is displayed in figure 3. The analysis could not be extended below a bombarding energy of 5 MeV because of the increasing degree of overlap of n_0 pulses with $\gamma_{4.43}$ pulses. Errors introduced by this overlap are probably responsible for the large scatter apparent in the lowest few points of the yield curve.

The uncertainty due to neglect of the possible effects of multiple neutron scattering in the stilbene along with uncertainty in the target thickness leads to an estimate of 20% for the standard deviation of the absolute value of the cross section. The statistical error on each point is 2% or less for the points above 5.5 MeV.

4.2. The n_1 yield curve

The n_1 yield curve may either be measured directly or be obtained from the yield of the 4.43-MeV gamma ray since reactions leading to the 4.43-MeV level of C^{12} are the only significant source of this gamma ray. (All higher levels are particle unstable.) We used the gamma ray to obtain most of the yield curve, measuring the height of the Compton shoulder relative to underlying structure. Some spectra taken of the reaction $N^{15}(p, \alpha\gamma_{4.43})C^{12}$ gave very clear $\gamma_{4.43}$ spectra for comparison purposes. The n_1 group itself was analyzed by the integral-sum method for $E_\alpha \geq 11.3$ MeV to find the absolute cross section. The yield curve obtained from $\gamma_{4.43}$ was then scaled to this portion of the curve. Cross sections for several points lower on the yield curves were found directly by the initial-step-height method and agreed with the scaled values to within 30%.

Figure 4 displays the results. The absolute values of the cross sections are assigned standard deviations of 30%; the relative error on each point is 5% or less. The dotted portion of the curve is the region in which the n_1 shoulder is passing through the $\gamma_{4.43}$ shoulder, making accurate separation of the two unfeasible. However, the yield does not deviate more than 20% from the position indicated by the dotted line.

4.3. The n_2 yield curve

The energy of this neutron group is so low over the whole range measured (E_n = 3.25 to 7.00 MeV) that multiple scattering greatly distorts the spectrum. Thus the initial-step-height method of analysis was used throughout. The results are presented in figure 4. The absolute value of the cross section is correct to within 40%. The statistical error on each point is 10% or less. Below E_α = 6.0 MeV, the n_2 group could not be clearly identified; above E_α = 10.0 MeV, the n_2 shoulder is merging with $\gamma_{4.43}$.

4.4. Levels of C^{13}

Assuming the nine peaks in the n_o yield curve correspond to nine resonant levels in the compound nucleus, C^{13}, the parameters listed in table 1 were determined. Many of the resonances are also present in the n_1 and n_2 yield curves. The large rise in the n_1 yield curve between 4.0 and 6.0-MeV bombarding energy appears to be composed of several additional levels, but our data are not sufficiently good to perform an accurate separation.

The results of two previous studies partially covering the same region of C^{13}, both of which utilized the same reaction, are included in the table. Gibbons and Macklin (1959) measured the total

neutron cross section summed over all angles for bombarding energies between 2.58 and 8.2 MeV and identified four levels in the region we have covered. The first three, at E_α = 4.5, 5.0 and 5.75 MeV, can be associated with the pronounced rise we see in the n_1 yield curve in this region as well as with the resonance at E_α = 5.40 MeV in the n_o yield curve. Their fourth level, at E_α = 7.8 MeV, may correspond to the prominent resonance at E_α = 7.95 MeV in our n_o yield curve and to a poorly-resolved structure at about the same energy in the n_1 yield curve. The resonances they see are fairly small ($\lesssim$ 10%) variations in the total mention cross section which rises nearly uniformly from a value of about 400 mb at 4.5 MeV to around 600 mb at 5.5 MeV after which it stays fairly constant.

Seaborn et al. (1963) measured the 0^o and 90^o $\gamma_{4.43}$ yield for $3.4 \leq E_\alpha \leq 10.1$ MeV. Their 0^o $\gamma_{4.43}$ curve closely resembles ours in the region of overlap except that the higher resonances (above E_α = 7.8 MeV) we see are masked in their data by resonances in $C^{12}(\alpha, \alpha'\gamma_{4.43})$. They also measured thirteen angular distributions between 3.3 and 7.6-MeV bombarding energy in an attempt to understand the broad rise in the n_1 yield. All the angular distributions were symmetric about 90^o. After fitting the distributions with Legendre polynomials up to P_4, they concluded that the rise is probably due to several (maybe four) broad overlapping levels, two of which are in agreement with the results of Gibbons and Macklin. Above the broad resonance they identified two more levels: an uncertain one at E_α = 7.1 MeV in agreement with a resonance in our n_o yield curve (and perhaps our n_1 curve as well), and another at E_α = 7.7 MeV which may correspond to our n_o resonance at E_α = 7.95 MeV and to the level seen at E_α = 7.8 MeV by Gibbons and Macklin.

As pointed out by Seaborn et al., the total neutron cross section measured by Gibbons and Macklin can be almost entirely accounted for by n_1 up to about $E_\alpha = 5$ MeV. Beyond this point, a large part of the cross section is probably from low energy neutrons arising from the various possible mechanisms which leave $3\alpha + n$ in the final state. (Our n_2 group is the most energetic neutron group produced in this way.)

In our data, it is rather surprising that the n_o yield curve has so many resonances which show up only weakly or not at all in the n_1 and n_2 yield curves. It is equally surprising that the large rise between $E_\alpha = 4$ and 6 MeV in the n_1 yield should not show up more clearly in the n_o yield. Some of the structure we have attributed to resonating C^{13} levels may in fact be interference effects or fluctuations involving two or more overlapping nuclear levels. Thus, for example, the n_o "resonances" at $E_\alpha = 9.7$ and 10.2 MeV may well be an interference anomaly from a single level. The level at $E_\alpha = 11.70$ MeV is, however, almost certain to be real. It is well defined and appears clearly in both the n_o and n_1 yield curves.

IV. SEMICONDUCTOR DETECTOR AS A FAST NEUTRON SPECTROMETER

1. Introduction

A silicon semiconductor particle detector may be used to obtain precision neutron energy measurements, the neutrons being detected by means of charged-particle-producing nuclear reactions with the silicon of the active volume of the detector. Neutron energy measurements have been made in this way over the range 6 to 17 MeV and higher-energy measurements are possible. The method is primarily useful for measuring the energy of the most energetic neutron produced in a reaction. Usually, lower-energy neutrons can also be measured, but with less precision. Measurements of neutron yield are also possible.

Deuchars and Lawrence (1961) were the first to observe neutron-induced reactions in a silicon semiconductor detector and many other groups have observed them since, several of them recognizing the neutron-detection possibilities. Among the first of these were Birk, Goldring and Hillman (1963) and Mainsbridge, Bonner and Rabson (1963). Mainsbridge et al., and Colli, Iori, Marcazzan and Milazzo (1963) used the technique to measure yield curves for neutron-induced reactions in silicon. Except for these measurements, a semiconductor detector has not previously been used for either neutron energy or neutron yield determinations. This chapter will discuss the problems involved and their solution. The next chapter contains applications of the method.

2. General description of the spectrometer

Figure 5 shows part of the spectrum produced by a 9.83-MeV neutron in a semiconductor detector. The neutron is represented by a whole family of charged particles which are the result of the different isotopes of silicon present, the different reactions possible with each isotope (the most important being (n, α) and (n, p) reactions), and the many states available in each residual nucleus. Note that the energies of the light charged particle and the heavy recoil nucleus produced in the reaction are summed by the detector. Table 2 lists all possible (n, α) and (n, p) reactions. Those marked with an asterisk are the only ones of practical importance in natural silicon.

Among the factors to consider when choosing a semiconductor detector for measuring neutrons of a particular energy are detection efficiency, resolution, and the possible effects of gamma rays. The detection efficiency is determined by the cross sections for the various neutron-absorption processes which can take place. Some of these have been measured and are given in section 4. As an example of their application, about 1 in 1.4×10^4 15-MeV neutrons passing through 1 mm of silicon will react via the $Si^{28}(n, \alpha_o)Mg^{25}$ reaction. Clearly, a detector with large active volume is desirable.

Good resolution is also desirable, but in practice, as active volume increases, resolution decreases. If one is studying neutrons from a reaction induced by an accelerator beam, well defined in both energy and position, there is little point in increasing the volume by increasing the area -- the resolution will soon be limited by the kinematic energy spread of the outgoing neutrons. The detector will have to be moved further away, thus reducing the maximum possible absolute efficiency to that of a smaller detector (with better intrinsic resolution) located closer to the target. It is the depth of the detector which should be as great as possible.

The resolution of a semiconductor detector when used to detect neutrons is always much worse than when used to detect either α particles or protons alone. The best FWHM neutron resolution we have obtained for the $Si^{28}(n, \alpha_o)Mg^{25}$ peak is about 125 keV, even for detectors whose resolution for α particles alone is less than 25 keV. This phenomenon, as well as a difference in amplitude for equal-energy pulses produced by the reactions $Si^{28}(n, \alpha)Mg^{25}$ and $Si^{28}(n, p)Al^{28}$, both appear to be due to effects associated with the heavy recoil ions (Mg^{25} and Al^{28}) and are discussed in detail in section 5.

A semiconductor detector will also detect gamma rays, primarily by Compton scattering. Such gamma rays can come from two sources: gamma rays following the neutron-induced reactions in the detector itself and gamma rays from the nuclear reaction being studied. The first source is of little importance because of its very low intensity (the flux is comparable to the number of neutrons detected per second) and the fact that most of these gamma rays escape without interaction. For example, a 1-MeV gamma ray has a mean attenuation length in silicon of 6.7 cm and typically the detector dimensions are no greater than 1 cm. The only exception is the 31-keV gamma ray from the first excited-to ground state of Al^{28} which has a mean attenuation length of only 0.36 cm. Thus the p_{01} double peak (see figure 5) cannot be resolved, even in principle.

Gamma rays from the reaction being studied may, however, be a serious problem. The ratio of the Compton plus pair cross section to the $Si^{28}(n, \alpha_o)Mg^{25}$ cross section for a gamma ray and neutron each having an energy of 10 MeV is about 10 to 1 and the incident gamma-ray flux often exceeds the neutron flux. Fortunately, the amount of energy which an electron can lose in the detector is limited by the detector

dimensions and is less than 4.5 MeV if the largest dimension is 1 cm (a length sufficient to stop a 45-MeV proton or 200-MeV α particle). Thus, if high-energy gamma rays are present, they set a lower limit on the neutron energy which may be accurately measured. When necessary, this problem may sometimes be avoided by using a detector smaller than would otherwise be desirable.

At this time, the deepest semiconductor detectors are made using the lithium-drift technique of Pell (1960). We have usually used such detectors obtained from Technical Measurement Corp., San Mateo, California. These detectors had cylindrical shape with an active diameter of 1 cm and depth of 5 mm. All the discussion of the remainder of this section is based on Li-drifted detectors with these dimensions.

Resolution is much improved by cooling. For one detector tested, the resolution of the $Si^{28}(n, \alpha_o)Mg^{25}$ peak improved from 190 keV at room temperature to 145 keV when cooled with liquid nitrogen and, for some detectors, neutron resolutions as low as 125 keV, apparently the best obtainable with any silicon semiconductor detector (see section 5), have been obtained after cooling.

We routinely check detectors with an 0.23- mC. calibrated Cs^{137} gamma-ray source. The 0.662-MeV gamma ray is detected primarily by Compton scattering for which the cross section is known. Thus the volume of the detector may be measured directly. At the same time, a very small fraction of the gamma rays is totally absorbed by the detector and produces a peak analogous to the photopeak of a NaI crystal. The resolution of this peak provides a figure-of-merit for the uniformity and quality of the entire active volume of the detector. Figure 6 shows a typical spectrum. A good

detector has, when chilled, a gamma-ray resolution of less than 20 keV. (Our ultimate resolution was limited to about 7 keV by the electronics.) However, a detector which has good resolution for gamma rays may not have good neutron resolution. One detector tested had, when chilled, a gamma-ray resolution of less than 10 keV but a neutron resolution of 230 keV. One possible explanation is that the silicon crystal contains many local inhomogeneities, such as droplets of lithium: fluctuations in the rate of energy loss of an electron due to these inhomogeneities are averaged out over the range of the electron whereas a heavy particle is brought to rest via only one or a few inhomogeneous regions.

Detectors often suffer from a second kind of defect: prominent low-energy tails on all the peaks of the neutron spectrum. These tails tend to wash out peak structure, making it difficult to find excited states in the reaction being studied. It appears that a detector can have fairly good resolution and still show such tails.

A detector is considered suitable as a neutron detector if:

i) The neutron resolution, when chilled, is 150 keV or better.

ii) The ratio of the α_0 peak height to the valley height just above α_1 is 15 to 1 or better. (The best we have observed is 22 to 1.)

3. Neutron energy measurement

Figure 7 shows one of several similar mounting arrangements used for the semiconductor detector. The principal function of the mount is to enable the detector to be chilled in such a way that ice frozen out from the atmosphere does not form on the detector or its external electrical connections. Such ice formation greatly increases the noise output of the detector. It is, of course, not necessary to have the detector mounted inside the target chamber since almost all

the fast neutrons produced pass through the target chamber wall and the front face of the detector mount without interaction. Having the detector outside the target chamber greatly simplifies any moving of the detector which must be performed during the course of an experiment.

All precision neutron-energy measurements have been made with the detector at 0^{o} because kinematic energy spread is a minimum at this angle. The spectrum produced by the neutron being measured was compared with a calibration peak produced by a neutron of known energy as nearly equal to the unknown neutron energy as possible. This minimizes errors due to possible non-linearities of the detector or electronic equipment and makes possible the unfolding of complex spectra by the subtraction of the calibration spectrum from the unknown spectrum. The calibration spectra were obtained using the reaction $Be^{9}(\alpha, n_{o})C^{12}$ which, for this reason, was investigated in some detail (see chapter III). Another good calibration reaction would be $C^{13}(\alpha, n)O^{16}$.

All quantitative calculations have been based on the $Si^{28}(n,\alpha_{o})$ peak. Two methods have been used for finding peak position from the raw data: the centroid method and the intercept method. The first method is intrinsically the more accurate but requires that the target thickness and target-counter geometry be accurately known whereas the second does not.

Before discussing the two methods in detail, let us consider the shape of the $Si^{28}(n, \alpha_{o})$ peak produced by a cylindrical detector which has perfect resolution. Take the detector to be head-on, i. e., the neutrons are incident normal to the circular face. The neutron peak will be broadened by two effects: the spread in beam energy due to finite target thickness, and the kinematic spread in the energy of

the outgoing neutrons due to the finite solid angle subtended by the detector. If the cross section as a function of beam energy is constant, the effect of target thickness alone is to produce a rectangular peak shape.

The effect of kinematic spread is slightly more complicated. If the detector (located at 0^{o}) subtends an angle sufficiently small that $\sin\theta \sim \theta$, the neutron energy as a function of angle, $E_n(\theta)$, is given by

$$E_n(\theta) \cong E_n(0) - K(A, E_{beam})\,\theta^2 \quad . \tag{1}$$

The quantity K increases as A decreases or E_{beam} increases. If the cross section as a function of angle and energy is constant, the probability of a particular count occurring in the cone defined by θ and $\theta + d\theta$ is approximately given by

$$P(\theta)\,d\theta \cong \frac{2\pi h^2\,\theta\,d\theta}{\pi\,\theta_o^{\,2}\,h^2} = \frac{2\theta\,d\theta}{\theta_o^{\,2}} \quad . \tag{2}$$

The quantities h and θ_o are defined in figure 8a. Let $P(\delta)$ be the probability of a deviation δ from $E_n(0)$. From (1), $\delta = K\theta^2$. Therefore, $P(\delta)d\delta = P(\theta)d\theta$ and

$$P(\delta) = P(\theta)\,\frac{d\theta}{d\delta} \cong \frac{1}{\theta_o^{\,2}\,K} \quad . \tag{3}$$

Thus $P(\delta)$ is constant and kinematic energy shifts alone will also produce a square peak.

The two effects taken together, target-thickness shift and kinematic shift, will in general produce a peak shaped like a truncated triangle. Note in particular that the leading edge of this peak should be a straight line whose intercept with the axis gives a measure of the zero-degree neutron energy independent of both target thickness and solid angle. This is the basis of the intercept method.

The effect of imperfect detector resolution is to round out the peak. However, it is found that if only those points between 10% and 90% of maximum peak height are used, a very good fit to a straight line is obtained. The intercept with the axis is found to be the same to within a few keV for neutron peaks of the same energy taken under differing experimental conditions. This method should probably be used whenever the counting statistics are sufficiently good to allow discarding the data provided by the rest of the counts in the peak.

In the centroid method, one simply calculates the centroid of the peak. In a real detector, the low energy side of the peak has a long tail. The method used to treat this tail was to fit a straight line to the back side of the peak above the tail, extend the line to the axis, and artifically lower points in the tail to fit it.

Both the incident beam energy and the outgoing neutron energy require corrections if a Q value is to be calculated. To first order, these corrections can be made in the following way: The effective beam energy is taken to be the incident beam energy lowered by half the target thickness. This corrects for energy loss in the target. The energy of the neutron group detected is taken to be the energy the neutron would have at 0^{o} minus the average kinematic energy spread of the neutron group due to the finite solid

angle subtended by the detector. As a result of equation (3), this last correction is just half the maximum kinematic energy spread of neutrons incident on the detector, i. e., $Kr^2/2h^2 \cong K\theta_o^2/2$.

If the detector being used has a radius greater than or equal to the depth (the usual case), one may get about 40% greater efficiency with the same average kinematic energy spread (i. e., average deviation from the 0^o value of the neutron energy) by using the detector side-on (see figure 8b). In this case, the average kinematic spread is approximately $K/8h^2\ (t^4 + 4r^4)^{1/2}$ which for $r \gtrsim t$, is approximately $Kr^2/4h^2 \cong K\theta_o^2/4$.

The errors assigned to the Q values we measured with the spectrometer have the following sources: uncertainty in the exact value of the incident beam energy, errors in the corrections for energy loss in the target and kinematic energy spread of the outgoing neutrons, and counting statistics. The first source of error was always the largest, ranging from 10 to 20 keV for each independent measurement; it was set by the geometrical precision of the magnetic analysis of the beam energy. See Pearson (1963) for a detailed discussion. In our experience, the beam energy was usually confined to within 1/2 to 2/5 the range calculated from the slit widths at the entrance and exit of the analyzing magnet when the total slit widths were 0. 100" to 0. 150" providing there was steady tandem operation and good beam alignment.

4. Detection efficiency and neutron yield measurement

The charged-particle spectra produced by known numbers of neutrons bombarding a Li-drifted silicon semiconductor detector have been obtained for neutron energies from 7. 3 to 16. 4 MeV in steps of 50 keV or less. The purpose of the measurements was to

obtain cross section curves for the neutron-induced reactions in silicon sufficient to enable the determination of unknown neutron yields. Two nuclear reactions, $D(d, n)He^3$ and $Be^9(\alpha, n)C^{12}$, were used as sources of monoenergetic neutrons, the first providing neutrons from 7.3 to 12.0 MeV, and the second, from 10.6 to 16.5 MeV. The ONR-CIT tandem provided deuterium and α-particle beams magnetically analyzed to a precision of 0.2%. A deuterium gas target was used. The beam came in one end of a tantalum-lined, stainless steel cylinder 3.69 cm long through a nickel foil 5000 A thick and was stopped in tantalum at the other end. At the lowest bombarding energy used, 4.00 MeV, the deuterium beam lost 37 keV in the entrance foil and 5.4 keV in the target chamber gas. The Be^9 target was 72 ± 14 $\mu g/cm^2$ thick. At the lowest α-particle bombarding energy used, 5.1 MeV, the beam lost 51 keV in the target. Figure 11 shows the detection geometry used for both beams.

Once the data were obtained, there was some question as to the best method of analysis. As already stated, the objective was to obtain curves which would be useful for the determination of neutron yield when using a semiconductor detector as a neutron spectrometer. Only peaks from Si^{28} + n reactions are prominent and only these were considered (but see the last paragraph of this section regarding $Si^{29}(n, \alpha)$). Obtaining the maximum amount of information would involve extracting cross sections for each of the separate processes which occur such as the cross section for $Si^{28}(n, \alpha_3)Mg^{25}$. However, several of the peaks are often difficult to separate. Further, the detectors used for these measurements were Li-drift detectors and often the peaks in the spectra obtained with such detectors have prominent low-energy tails as compared with, for example, the results obtained in a surface-barrier detector (see section 2). Thus a peak such as α_3 is not only difficult to separate from p_{01} but has

tails beneath it from all higher peaks (α_o, α_1, α_2, and p_{01}). There is no way of measuring the exact shape of these tails and a small error in estimating their magnitude could lead to a very large error in the deduced cross section.

For these reasons, cross sections were found for all Si^{28} + n reactions above three well-defined valleys in the spectra: the valleys between α_o and α_1, α_2 and p_{01}, and p_{23} and p_4 (or α_5 if visible). These represent the cross sections for α_o (the highest energy Si^{28} peak), $\alpha_o - \alpha_2$ (first three peaks), and $\alpha_o - p_{23}$ (first seven resolved peaks). Figures 9 and 10 show two typical spectra, one from the D(d, n) portion and one from the $Be^9(\alpha, n)$ portion of the yield curve. The numbers given on the detection geometry figure, figure 11, pertain to these two spectra. In appendix 1, a detailed calculation of the $Si^{28}(n, \alpha_o)$ cross section is given for the same two spectra. The entire yield curves are plotted in figures 12 - 15. Possible contributions from tails extending outside the summed region were at least partly taken into account by correcting the sums for particle escape through the edge of the detector (see appendix 1). The error from this source is largest for the $\alpha_o - \alpha_2$ sum but is estimated to be always less than 10% and usually less than 5%. The error on the α_o sum from this source is less than 2%. Peaks from reactions with other isotopes of silicon may be included in the summed regions. Such peaks were not seen and no correction has been made for them. The standard deviation on the absolute cross sections is estimated to be about 10% for neutron energies below 12 MeV but may increase to as much as 20% in the 16-MeV region. Table 3 is a list of the clearly-resolvable resonances in the α_o cross section for neutron energies between 7.2 and 11.2 MeV. These all appear to correspond to levels in Si^{29} but, at slightly higher neutron energies,

curve structure is more likely due to Ericson fluctuations (see Colli et al. (1963)).

The spectra of the $Be^9(\alpha, n)$ portion of the yield curve were also analyzed in terms of the first seven resolved peaks: α_o, α_1, α_2, p_{01}, α_3, α_4 and p_{23}. A computer was used to sum each peak and subtract from beneath it fixed fractions of all higher peaks to allow for the contribution of tails beneath the peak. The fractions used were determined empirically by careful hand analysis of several spectra distributed along the yield curve. The results for all but α_o (already given in figure 13) are shown in figures 16 to 18. The standard deviation is estimated to be less than 30%.

The integral sum cross sections of figures 12 - 15 may be directly used to correct for variations in detection efficiency due to variations in neutron energy. Note that the particular integral sums chosen are not very sensitive to the quality of the detector. As a check on the curves, the cross section at 0^o for $Be^9(\alpha, n)C^{12}$ was measured in a semiconductor detector for bombarding energies between 2 and 6 MeV. The same results are obtained independent of which of the integral cross sections is used. Figure 19 displays the curve obtained from analysis of the α_o peak. The absolute cross section agrees with figure 2 in the region of overlap and with the measurements of Risser et al. (1957). This one curve ties together all the absolute cross section measurements of Chapters III and IV. Its consistency with other curves and with published data is very reassuring.

Two other groups have made extensive cross section measurements for Si^{28} + n reactions in a semiconductor detector. Mainsbridge, Bonner and Rabson (1963) measured separate cross sections for α_o, α_1, α_2, α_3, p_{01}, p_{23}, p_{45} and p_{678} for neutron

energies between 4.6 and 8.5 MeV, and quote an error of 30% on the absolute cross section. Our data overlap the last 1.2 MeV of their curves and agree well in relative shape if correction is made for the fact that the α_o curve of figure 4 of their paper has been accidently transposed upwards in energy about 200 keV (Rabson (1965)). Their absolute cross section normalization is about 1.8 times higher than ours.

Colli et al. (1963), who were investigating Ericson fluctuations, measured separate cross sections for α_o, α_1, α_2, α_3, α_4, and two higher α groups for neutron energies between 12.15 and 18.5 MeV and quote an error of 30% on the result. Comparison of our α_o yield curve with theirs in the region of overlap (12.15 to 16.4 MeV) indicates fair agreement as to relative shape but there are differences in both peak location and peak height. Peaks on their curve occur at neutron energies from 50 to 150 keV higher than peaks on our curve as the neutron energy is increased from 12 to 16 MeV. Our absolute cross sections vary from being 1.4 to 1.8 times higher than theirs over the same range. Part of the yield difference is explainable. They used a small (25 mm area, 0.3 mm deep) semiconductor detector as both target and detector and made no correction for escape through the edges, which they assumed produced at most a 20% error. However, we find that the correction factor varies from 1.25 to 1.44 as the neutron energy is increased from 12 to 16 MeV. (See the formula for f and the discussion following it in appendix 1). Forward or backward peaking in the α-particle angular distribution could easily make this correction much larger. In using their data, care must be taken in deciding which curve belongs with a particular reaction since the curves are unlabelled and the captions are misleading (largely because their curves have been reduced so much in

publication that the different kinds of points they used are indistinguishable).

The α_o peak is usually the most convenient peak to use for determining either neutron energy or neutron yield. At a neutron energy of 6 MeV, the cross section for its formation is less than 10 mb but rises rapidly to as much as 150 mb for neutron energies of 7.5 to 8.0 MeV as the α particles acquire sufficient energy to overcome the Coulomb barrier of the compound nucleus. As the neutron energy is further increased, the cross section slowly falls, sinking to a value of about 10 mb at 16 MeV, the fall being probably due to the increased number of final states available to the compound nucleus. Arbitrarily taking 10 mb as the smallest acceptable cross section, a semiconductor detector made of natural silicon is useful as a neutron spectrometer for neutron energies between 6 and 16 MeV.

As pointed out (and patented) by Birk, Goldring, and Hillman (1963), a semiconductor detector made of Si^{29} would enable useful measurements to be made at lower neutron energies as the Q value of the $Si^{29}(n, \alpha_o)Mg^{26}$ reaction is -36 keV compared with -2655 for $Si^{28}(n, \alpha_o)Mg^{25}$. Mainsbridge et al. find the $Si^{29}(n, \alpha_o)$ cross section to be about 70 mb for a neutron energy of 5.0 MeV. A further advantage in simplifying the spectrum accrues from the greater excitation energy, 1.81 MeV, of the first excited state in Mg^{26} (compared to the value 0.58 MeV in Mg^{25}).

5. Pulse-height and resolution anomalies

Peaks from the reactions $Si^{28}(n, \alpha)Mg^{25}$ and $Si^{28}(n, p)Al^{28}$ show a differential pulse-height defect, i.e., peaks produced in the reaction $Si^{28}(n, p)Al^{28}$ always fall below the amplitude predicted for them by a calibration obtained from the $Si^{28}(n, \alpha)Mg^{25}$ peaks. In

figure 5, the quantity ΔE (equal to 78 ± 10 keV) indicates the differential pulse-height defect measured for this spectrum. The defect is a function of neutron energy and increases with it in an approximately linear fashion over the region measured (see figure 20). A similar defect is not seen on comparing $Si^{28}(n, \alpha)$ and $Si^{29}(n, \alpha)$ peak amplitudes. For example, in figure 5, the α_1' peak is within 6 keV of the position predicted for it by the $Si^{28}(n, \alpha)$ peaks and, for all spectra examined, its position is always consistent with zero differential pulse-height defect independent of neutron energy. Clearly, the defect is associated principally with differences in electron-cloud structure rather than mass alone.

The resolution we observe for peaks such as $Si^{28}(n, \alpha_o)$ is always three or more times worse than one might expect on the basis of α particles alone being stopped. In fact, we have never obtained a "neutron" resolution of less than 125 keV full width at half maximum, even with detectors whose α-particle resolution is 30 keV or less. Neutron resolution appears to get slightly worse as the neutron energy is increased. The resolution of the aluminum and magnesium peaks appears to be about the same but it is hard to make exact comparisons because of the difficulty in subtracting the correct amount of background from beneath the aluminum recoil peaks.

The emphasis of the following discussion is on explaining the differential pulse-height defect. However, the two effects, differential defect and poor resolution, appear to have a common origin and will end up being explained together.

Generally speaking, a pulse-height defect could arise either from reduced charge collection, e. g., recombination losses, or from reduced charge production. For a particular detector, such as the

Li-drift detector used to obtain the spectrum of figure 5, the magnitude of the defect is independent of both bias and temperature. For low biases, the whole spectrum shifts down and the resolution decreases due to poorer charge collection, but the differential defect is unchanged. Reducing the temperature from room temperature to near liquid nitrogen temperature may improve the resolution as much as 50%, but again the differential defect is unchanged.

For neutrons of fixed energy, the defect is the same independent of the detector used. We have checked this with Li-drifted detectors and both high and low resistivity surface-barrier detectors obtained from several different manufacturers. It is hard to believe the defect is the result of recombination losses when it is unaffected by so many factors which should change such losses. Apparently, the defect is the result of reduced charge production and is an intrinsic property of aluminum and magnesium ions being brought to rest in silicon.

To test this directly, we bombarded thin foils of aluminum and magnesium with α particles from the ONR-CIT tandem. The momenta of the recoil ions (energies of 1 to 3 MeV) were measured with a magnetic spectrometer and the pulse heights they produced were measured with a surface-barrier detector at the focal plane of the magnet. Both ions had a pulse-height defect relative to a calibration obtained with scattered α particles, the aluminum ions having the larger defect as expected. However, the dead layer on the front of the detector would produce the same sort of differences and different detectors produced different relative defects. Unfortunately, we were unable to separate an intrinsic defect from the effects of the dead layer.

It has been known for some time that fission-fragment spectra observed in a semiconductor detector show an absolute pulse-height defect variously reported as being from 4 to 20 MeV. The defect is greater for heavier particles but most observers have found it to be independent of the type of semiconductor detector used and of the conditions, such as bias voltage, under which it is used. Two theories have been advanced to explain the defect: It is caused by recombination of electron-hole pairs in the dense plasma produced in the first part of the track (i. e., charge loss), and that it is the result of screened atomic collisions near the end of the track which are relatively inefficient at producing ionization (i. e., decreased charge production). Axtmann and Kedem (1965) have performed an experiment which discriminates between the two theories. They measured the defect for fission fragments whose energies were degraded in air and found it to be approximately constant for both median heavy (defect $\approx$ 13 MeV) and median light (defect $\approx$ 11 MeV) fission fragments over the energy range 25 to 100 MeV. They concluded that the defect arises at the end of the fragment track and is the result of reduced charge production.

Aitken and Dixon (1965) have seen an absolute pulse-height defect in both silicon and germanium semiconductor detectors. They found that the $Si^{28}(n, \alpha)$ and $Ge^{73}(n, \alpha)$ peaks produced by 14. 1-MeV neutrons were shifted 250 keV and 400 keV respectively relative to the calibration obtained using an Am^{241} alpha source and that the defects were independent of detector bias.

Sattler (1965) measured the maximum pulse height of recoil silicon atoms in the reaction Si(n, n) as a function of neutron energy using a silicon semiconductor detector as both target and detector, and using internal-conversion electrons to obtain an energy cali-

bration. He found the maximum pulse height of the recoil silicon atoms to be less than expected on the basis of the electron calibration and obtained a direct measure of the fraction of the silicon recoil energy lost to ionization. His data vary in roughly the same manner as the Al - Mg differential defect plotted in figure 20. Note that in figure 20 ions of different energies are compared, the aluminum recoils always having lower average energies than the magnesium recoils, and both having energies distributed from zero to some maximum value. However, on the basis of the silicon recoil data of Sattler, the absolute defect is expected to increase with energy; the differential defect would be even larger if the two ions had the same energy.

On comparing our data with that of Aitken and Dixon, and Sattler, it is seen that the absolute magnitude of the defect may be inversely correlated with the first ionization potential of the recoil ion; i. e., silicon has the largest ionization potential and the smallest defect. It is also true that for low ion energies ($E \lesssim 3$ MeV) and at fixed velocity, the aluminum ion will always have the highest average charge.

Flicker (1963) was the first person to suggest that atomic collisions might compete significantly with ionization as a mode of energy loss but he performed no quantitative calculations. Haines and Whitehead (1965) have made such calculations and compare their results with observed absolute pulse-height defects, obtaining good agreement with many measurements for both light and heavy ions in both germanium and silicon detectors. Their calculations were performed in the following manner: first, the fraction of the incident ion's energy which is transferred to other ions by atomic collisions was determined. They find that the lower the ion's energy, the

greater the fraction of its energy lost in this way. Most of the recoil ions will have energies much lower than the primary and will lose all or almost all their energy in further atomic collisions. However, the occasional recoil will have sufficient energy to lose a significant fraction by ionization. Thus they extended their calculation to "second order" and found the fractional loss of energy through atomic collisions for the recoils as well (a number equal to one for most recoils). All further energy loss was assumed to take place entirely by atomic collisions. They used differential energy losses and scattering cross sections based on the Thomas-Fermi model of the atom without corrections for atomic shell structure. Thus their theory cannot and does not explain the differential pulse-height defect we see.

Haines and Whitehead also calculated the average dispersion in the energy lost by atomic collision processes. Their results are largely successful in explaining the poor resolution we find for peaks such as $Si^{28}(n, \alpha_o)Mg^{25}$, a resolution which is never better than about 125 keV. After subtracting by quadrature the resolution due to the spread in energy of the recoil Mg^{25} ($\approx$ 35 keV), the spread in the incident neutron energy ($<$ 40 keV) and the electronics resolution ($<$ 15 keV), one is left with an intrinsic resolution of about 110 keV. From figure 2 of their paper, the intrinsic resolution is predicted to be 75 keV in fair agreement with our observations.

6. Comparison with other methods

The ideal neutron detector would have the following properties:

i) High energy resolution preferably with each neutron of different energy being represented by a single peak rather than a continuous pulse-height distribution or a family of peaks.

ii) A detection efficiency which is approximately constant (or at least smoothly varying) over a broad range of neutron energy and is large enough so that the experiment may be performed in a reasonable length of time.

iii) Insensitivity to other radiations, particularly gamma rays, which may also be present.

No detector exists which meets all of the above criteria and the particular detector chosen for a given application will depend upon the yields and energies of the neutrons present, whether a yield or energy measurement is wanted and on the presence or absence of gamma rays. For our measurement of the $Fe^{54}(He^3, n)Ni^{56}$ Q value, we wanted a detector which could measure the energy of a 15-MeV neutron with a precision of at least 25 keV and furthermore, could do this in a reasonable length of time. The 0^o (He^3, n) cross section is about 0.1 mb/sr . To obtain the necessary resolution, target thickness and detector solid angle must be restricted. The target was chosen to be about 25 keV thick for an 11 to 12-MeV He^3 beam and the detector was allowed to subtend no more than 19^o in order that the average kinematic energy spread be less than 25 keV. Thus, with a maximum beam current of 1 μa of He^{3++}, the expected neutron flux through the detector is 140 per second. If the minimum acceptable count rate is taken to be one per minute, the detector must detect at least 1 in 8400 neutrons incident on it. The only technique we could find which could achieve the necessary resolution with the above efficiency was the silicon-semiconductor-detector nuclear-reaction method (hereafter abbreviated as the silicon spectrometer method). A 5 mm deep detector has an efficiency about three times the above minimum for detection in the $Si^{28}(n, \alpha_o)Mg^{25}$ peak and the precision obtainable is limited by uncertainty in the bombarding energy ($\approx$ 10 to 20 keV) rather than the spectrometer itself.

Some of the other techniques which might have been used but were found wanting for one reason or another are proton-recoil counters, time-of-flight, organic scintillators and nuclear emulsions. These and other systems are discussed in detail elsewhere (see e. g., Marion and Fowler (1960)). The proton-recoil counter technique (see e. g., Johnson and Trail (1956)) in which knock-on protons are produced in a polyethylene radiator and detected externally meets all the criteria listed in the first paragraph except that of efficiency which is 10^3 to 10^4 times less than the silicon spectrometer method. Time-of-flight techniques may compete in energy resolution with the silicon spectrometer at the very bottom of the latter's useful energy range, but even here, the precision of typical time-of-flight measurements is usually about five times worse. To maintain resolution at higher neutron energies, the flight path must be increased and the count rate soon becomes too small to make the measurement feasible.

Most of the problems associated with neutron-detection systems arise from the necessity of converting neutrons to charged particles before they are detected. One of the most widely used conversion methods is neutron-proton scattering for which the cross section is both well known and smoothly varying. However, the recoil protons are distributed from zero energy to the full neutron energy. Fortunately, the distribution is approximately uniform, at least for neutron energeis below 20 MeV. Other conversion methods utilize neutron-induced nuclear reactions such as the silicon spectrometer method ($Si^{28}(n, \alpha)Mg^{25}$), the BF_3-filled proportional counter ($B^{10}(n, \alpha)Li^7$) and the He^3-filled proportional counter ($He^3(n, p)T$), although the latter two methods have extremely low efficiency for detecting neutrons in the energy range of interest here.

No matter how the neutrons are converted, the detectors fall into roughly two classes: those for which the conversion takes place within the active volume of the detector and those for which it takes place in an external radiator. Thus, for example, in detectors utilizing n-p scattering, protons are produced throughout the volume of an organic scintillator but in a proton-recoil counter they are produced in an external radiator, e. g., polyethylene, from which they must escape before being detected (in, e. g., a semiconductor detector). In either case, it is the volume of the region in which the protons are produced that determines the detection efficiency. The first type has a large and smoothly-varying efficiency but poor energy resolution and high sensitivity to gamma rays. The second type has low efficiency because of the restricted size of the radiator but may have better energy resolution if only protons scattered in one direction are accepted in which case neutrons of different energies produce discrete peaks. The gamma ray sensitivity is low.

The silicon spectrometer method combines the advantages of both the above types in that neutrons are detected throughout the active volume of the detector and neutrons of a particular energy produce discrete peaks. Gamma rays are seldom a problem. The disadvantages are that the detection efficiency is rapidly varying and a monoenergetic neutron produces more than one peak. The silicon spectrometer method is in some respects similar to the use of a He^3-filled proportional counter.

One widely-used method remains: the use of nuclear emulsions. They contain a great deal of hydrogen (mostly in water) so that neutrons may be detected by internally produced protons as well as by particles from an external radiator. Since the direction of the incident neutrons is usually known, the neutron energy may be

determined from a single track. However, for proton recoils above 5 MeV, range straggle sets a lower limit of about 1% on the accuracy of this kind of measurement. In practice, precision as good as 50 keV is seldom obtained. Neutron yields may be obtained fairly accurately.

In conclusion, the silicon spectrometer method appears to be a valuable addition to the large number of neutron detectors available, making possible neutron energy measurements of low intensity, 6 to 16-MeV neutron groups with a precision not easily obtainable before.

V. THE (He^3, n) MEASUREMENTS

1. Introduction

This chapter might better be titled "Applications of a Semiconductor Detector as a Fast Neutron Spectrometer" as it contains all the results obtained with this technique. However, that would be putting the emphasis on the wrong part of the investigation as the spectrometer was specifically developed to measure the mass of Ni^{56} via the reaction $Fe^{54}(He^3, n)Ni^{56}$. Once the technique was understood, it was a simple matter to perform additional measurements.

All the neutron energy measurements were Q-value determinations of (He^3, n) reactions. This reaction mechanism is a powerful tool for studying proton-rich nuclei as it effectively enables the addition of two protons to the target nucleus, leaving the residual nucleus as far as two positions away from the line of beta stability. The use of a semiconductor detector for measuring the neutron energy allows exploitation of this reaction mechanism, not easily done previously because of the high neutron energies (10 to 17 MeV) typically involved. All of the nuclei described in this section were poorly known. Four of them (Ar^{34}, Cr^{48}, Ni^{56} and Zn^{60}) had previously not even had their ground states located experimentally.

Also included are some neutron yield measurements. Absolute cross sections derived from the (He^3, n) data are given with the Q values in section 3. The angular distributions of neutrons to the ground and first excited states of S^{30} in the reaction $Si^{28}(He^3, n)S^{30}$ were measured and are given in section 5.

2. Procedure

The ONR-CIT tandem accelerator was used to produce a He^{3++} beam up to an energy of 12.1 MeV. The uncertainty in the beam energy was approximately 0.15 to 0.20% depending on the settings of the regulation slits of the analyzing magnet. Neutron energies were measured with a semiconductor detector by the method described in Chapter IV.

All but one of the targets were made by evaporating pure element of the substance to be bombarded onto tungsten backings 0.018 cm thick. The backings were washed in acetone and either heated to white heat in an evacuated tube in an induction furnace or etched in a 3 to 1 mixture of HNO_3 and HF; both processes appeared to be equally effective.

The targets used for studying Cr^{48}, Ni^{56} and Zn^{60} were made from isotopically enriched Ti^{46}(84.5%), Fe^{54}(97%), and Ni^{58}(99%) supplied by Oak Ridge National Laboratory. Natural magnesium (73.3% Mg^{24}), silicon (92.2% Si^{28}), sulfur (95.0% S^{32}) and calcium (96.9% Ca^{40}) were used as targets for the investigation of Si^{26}, S^{30}, Ar^{34} and Ti^{42}.

The sulfur target presented special problems because of the very low melting point of sulfur (113° C). A tungsten target backing was silver-soldered to a block of copper and sulfur was evaporated on half the front face, the other half being left for background runs. The block of copper was screwed to a second block of copper which was water cooled during beam bombardment. Though there was still some sulfur evaporation, it was possible to make a measurement of the $S^{32}(He^3, n)Ar^{34}$ Q value, but the change in thickness made it impossible to locate the excited states reliably. A target of

Sb_2S_3(mp = 550° C) was made by evaporation and showed no deterioration under bombardment when water cooled. This target enabled us to find one excited state in Ar^{34}.

The thickness of each target was measured to within about 20% by comparing the energies of 1-MeV protons scattered from the tungsten on the front and back sides of the target. All targets had a thickness such that, at the He^3 beam energy used, they were about 25 (and always less than 45) keV thick. The beryllium target used for calibration was chosen to give a neutron energy spread due to target thickness about equal to that from the target being studied.

Figure 21 shows the thickness measurements for two targets that were one of three pairs of targets used to measure the $Fe^{54}(He^3, n)Ni^{56}$ Q value. The Fe^{54} bombardment was performed at E_{He^3} = 11.50 MeV with the target at an angle of 45°. Using the data of the graph and the dE/dx curves of Whaling (1958), its thickness was deduced to be 21 ± 4 keV. The $Be^9(\alpha, n)$ calibration was performed at E_α = 10.80 MeV with the beam normally incident; the target thickness was 26 ± 5 keV.

The detector was located outside the vacuum system of the accelerator at an angle of 0° and at a distance such that the average kinematic energy spread of the incident neutrons was about 25 keV over the face of the detector. Its output was connected through a charge-sensitive preamplifier to the internal amplifier of a 400-channel pulse-height analyzer. The gain of the whole system was continuously monitored with a pulser and, in turn, the pulser voltage was periodically checked with a potentiometer. Calibration runs and runs on the unknown were alternated frequently to check gain and target stability and to monitor the build up of contaminants on the target. Additional runs at 30° ensured that the peaks observed moved an amount appropriate to the mass of the system under investigation.

3. Results

All our Q-value analysis has been based on the α_o peak of spectra taken at 0^o, the neutron energy being found by comparing unknown and calibration spectra. Peak position was found by both the centroid and intercept methods (see Chapter IV, section 3). If the two numbers did not agree, the data were rejected. This happened only once, probably because one of the targets was too thick.

In all the reactions studied, reactions other than the one of interest were observed. Except perhaps in the Cr^{48} measurements where other chromium isotopes may have contributed, these were always from contaminants on the target rather than other isotopes of the element being bombarded. This was determined directly by calculating where such isotopes would produce peaks and observing that they were not there. The reactions $C^{12}(He^3, n)O^{14}$ and $O^{16}(He^3, n)Ne^{18}$ were always observed. Some of the carbon was introduced during the manufacture of the target and more was deposited during the bombardment. The presence of oxygen was undoubtedly the result of target oxidation in air since the precautions taken to prevent this were not very stringent. Peaks from the C^{12} and O^{16} reactions were not troublesome since their Q values are more negative than all those measured (except $Ca^{40}(He^3, n)Ti^{42}$, for which these contaminants were used to provide an internal calibration). Peaks from C^{13}, O^{17} and O^{18} would have been more troublesome but were not observed. For example, in one check, the relative number of C^{12} to C^{13} events observed was greater than 200 to 1. In addition to the carbon and oxygen contaminants, peaks due to silicon and magnesium were observed in the Ni^{56} and Zn^{60} data. (This observation was the initial incentive for measuring the

$Mg^{24}(He^3, n)Si^{26}$ and $Si^{28}(He^3, n)S^{30}$ Q values.) These contaminants were observed to build up from an initially unobservable concentration during the course of the bombardment. The silicon is undoubtedly from O-ring grease and the magnesium is probably from the magnesium-containing ($\approx 1\%$) aluminum alloy used for the target holder and the beam pipe.

As a check on the method of analysis, one of the spectra in which carbon was present as a contaminant was analyzed in detail. A Q value of -1152 ± 14 keV was obtained for the reaction $C^{12}(He^3, n)O^{14}$. The weighted mean of all previous measurements is $Q = -1148.1 \pm .4$ keV. All our (He^3, n) Q value and excited state measurements are listed in table 4.

In figure 27 three excited states of Ni^{56} show themselves quite clearly in the raw data but usually excited states are masked by the family of peaks produced by the ground-state neutron and are seen clearly only after subtracting out these peaks. For this purpose, the $Be^9(\alpha, n)$ calibration spectra were used. The spectrum used for subtraction must be very close in energy to that of the ground state neutron because of the very rapid fluctuations in cross section for the neutron absorption events; the difference was usually less than 10 keV.

Rough estimates of the zero-degree cross sections were made for all the (He^3, n) reactions observed. The ground-state neutron cross section was obtained by comparing the yield of the (He^3, n) reaction with the yield from the best $Be^9(\alpha, n)$ calibration spectrum. The cross section may then be found by using the known $Be^9(\alpha, n_o)$ cross section (figure 3), target thicknesses, detection geometries and integrated beam current. Cross sections for excited-state neutrons were found by determining the ratio of their yield in

the $Si^{28}(n, \alpha_0)$ peak to the ground-state yield in the same peak using the known $Si^{28}(n, \alpha_0)$ cross section (see figures 12 and 13). These ratios, along with the ground-state cross sections are presented in table 5.

On the basis of what is known about (He^3, n) stripping theory (see, for example, Henley and Yu (1964)), the angular distribution of the neutrons leading to the ground state of all the nuclei studied here should be strongly forward peaked since both target and residual nuclei have 0^+ ground states. This is certainly true for the only angular distribution we have measured, that of $Si^{28}(He^3, n)S^{30}$ (see page 65 and figure 30). With this in mind, table 5 also includes the half angle, θ_0, subtended by the face of the detector.

The remainder of this section will give the detailed results obtained for each nucleus studied and compare them with previous work.

3.1 The Si^{26} nucleus

Figure 22 shows the spectrum obtained, from which a ground-state Q value of 85 ± 18 keV was calculated. Centroid and intercept methods of analysis gave answers differing by only 2 keV.

The subtraction spectrum shows two excited states of Si^{26}, at 1787 ± 27 keV and 2803 ± 28 keV, as well as peaks due to C^{12} and O^{16}. All peaks assigned to neutron groups leading to Si^{26} had the correct kinematics (checked at 0° and 30°) and could not be produced by any known contaminants. The pronounced dip just below channel 250 (just below the α_4 peak of the ground-state neutron group) illustrates one of the major problems encountered in unfolding the neutron spectra. For the beam energies used, the beryllium target was 13 keV thicker than the magnesium target (which was 32 keV

thick) and in addition, the most energetic neutrons from the beryllium target were 6 keV lower in energy than those from the magnesium target. There is a strong resonance in the α_4 yield just below the $Mg^{24}(He^3, n_o)$ neutron energy, and neutrons from the calibration reaction extended further into it than neutrons from the magnesium reaction.

The nucleus Si^{26} was first reported by Tyren and Tove (1954) although they obtained no direct evidence for its existence. They bombarded Al^{27} with 23-MeV protons and found a 1.7-second activity which they attributed to Si^{26} formed in the reaction $Al^{27}(p, 2n)Si^{26}$. Since then, three other groups have investigated Si^{26}, all of them using the reaction $Mg^{24}(He^3, n)Si^{26}$. The first positive identification was made by Ajzenberg-Selove and Dunning (1960), who detected the outgoing neutrons by means of proton recoils in nuclear emulsions and saw groups corresponding to the ground state, first excited state and second excited state, obtaining $Q = 80 \pm 80$ keV for the ground-state transition. Robinson and Johnson (1960) used an NaI (Tl) crystal to detect the gamma rays produced following the decay of Si^{26} and identified two positron branches leading to the 0.229 MeV and 1.059 MeV levels of Al^{26}. They measured a half life of 2.1 ± 0.3 seconds. Frick et al., (1963), using a magnetic spectrometer to measure the positron spectrum and an NaI (Tl) crystal to detect gamma rays, confirmed the above decay scheme. They determined the relative intensity of the two branches and found an end-point energy of 3.828 ± 0.013 MeV for the branch to the 0.229 MeV level of Al^{26}. They found a half life of 2.1 ± 0.1 seconds. From their numbers, the (He^3, n) Q value is found to be 58 ± 13 keV.

3.2 The S^{30} nucleus

The $Si^{28}(He^3, n)S^{30}$ spectrum is shown in figure 23. From two independent sets of runs, the Q value was determined to be -573 ± 15 keV. One excited state was seen at an energy of 2190 ± 40 keV.

Three groups have previously investigated S^{30}, all of them using the reaction $Si^{28}(He^3, n)S^{30}$. The first measurements were made simultaneously by Johnson et al., (1960) and Robinson et al., (1961), both of whom used scintillation techniques to look for positrons and gamma rays. Johnson et al., found a 1.5 ± 0.1-second-half-life positron activity with an endpoint energy of 4.22 ± 0.15 MeV in coincidence with a 0.676-MeV gamma ray. They attributed this to the decay of S^{30} to the T = 1, 0.684-MeV state of P^{30}. Robinson et al., identified the same branch, measured the β^+ end point to be 4.30 ± 0.15 MeV and the half life to be 1.35 ± 0.1 second. In addition, they detected the direct decay to the ground state, whose end point they measured as 4.98 ± 0.15 MeV. More recently, Frick et al., (1963) have measured the positron spectrum with a magnetic spectrometer, obtaining a half life of 1.4 ± 0.1 seconds and positron end points of 5.085 ± 0.026 and 4.422 ± 0.022 MeV. From the numbers of Frick et al., the (He^3, n) Q value is found to be -540 ± 27 keV.

3.3 The Ar^{34} nucleus

Figure 24 shows the $S^{32}(He^3, n)Ar^{34}$ spectrum obtained with the Sb_2S_3 target. A Q value of -759 ± 15 keV was determined from this spectrum and another series of runs in which a pure sulfur target was used. One excited state was seen, located at an energy of 2058 ± 35 keV.

The data of figure 24 could be used to determine the $S^{32}(He^3, n_o)$ Q value by a third method in addition to the centroid and intercept methods. This was for two reasons: the beryllium and Sb_2S_3 targets were of almost identical thickness (about 21 keV) and, for the particular neutron energy produced here, the cross sections of the silicon reactions which produce peaks α_o to α_2 and p_{01} all varied linearly with neutron energy. With the aid of a series of calibration runs taken with a spacing of 5 keV in neutron energy, the energy of the ground-state neutron of the Ar^{34} spectrum could be found to within 2 keV relative to the calibration neutron energy by comparing the relative yields of α_o to α_2 and p_{01} in the unknown and calibration spectra. Of course the ever-present uncertainties in the He^3 and He^4 beam energies remained. All three methods of analysis gave the same result for the ground-state Q value.

3.4 The Ti^{42} nucleus

Figure 25 shows one of five similar spectra used to obtain the $Ca^{40}(He^3, n)Ti^{42}$ Q value which was determined as -2865 ± 6 keV. Rather than calibrating separately with $Be^9(\alpha, n)$ as was done for all the other Q values measured, we used the carbon and oxygen contaminants on the target, assuming Q values (taken from Mattauch et al., (1965)) of -1148.1 ± 0.4 keV and -3196.0 ± 4.7 keV for $C^{12}(He^3, n_o)O^{14}$ and $O^{16}(He^3, n_o)Ne^{18}$ respectively. This procedure eliminated most of the error due to uncertainty in the beam energy.

On all five spectra, the location of the α_o peaks due to the ground states of O^{14}, Ti^{42} and Ne^{18} were calculated. Structure underlying the α_o peaks of Ti^{42} and Ne^{18} was subtracted out, a computer being used to find the best $Be^9(\alpha, n)$ subtraction spectrum among several taken for O^{14} and Ti^{42} and to calculate peak positions.

The linearity of the 400-channel analyzer was checked separately with a pulser. The O^{14}-Ne^{18} separation was used to find the number of keV per channel and the energy of the neutron to the ground state of Ti^{42} was calculated relative to the O^{14} neutron.

The isotope Ti^{42} has also been observed by Oberholtzer (1962) using the reaction $Ca^{40}(He^3, n)Ti^{42}$. Plastic scintillator was used to detect the positrons. He measured a half life of 0.25 ± 0.04 sec and an end point energy of 6.0 ± 0.6 MeV.

3.5 The Cr^{48} nucleus

Figure 26 shows one of two runs, the other being at a bombarding energy of 10.2 MeV, from which the Q value of $Ti^{46}(He^3, n_o)Cr^{48}$ was determined to be 5550 ± 18 keV. This Q value was the highest and therefore the most difficult to measure. As the beam energy is raised in order to get further over the Coulomb barrier, the neutron cross sections in the silicon fall which suggests the existence of an optimum bombarding energy. Even at this energy, low cross section and detection efficiency plus the thin targets required for energy resolution prevented getting good statistics in a running time of practical duration. In particular, it was impossible to obtain a good kinematics check. With the detector at 30^o, it was possible to verify that the $Si^{28}(n, \alpha_o)$ peak of the neutron to the ground state of Cr^{48} (the n_o-α_o peak) shifted approximately the right amount (and certainly not enough to be a light contaminant) but it was impossible to resolve any of the other groups seen at 0^o. The small peaks above and below the n_o-α_o peak (in channels 387, 375 and 363) shift in a different manner with bombarding energy than the n_o-α_o peak and are probably from a light contaminant which we were not able to identify.

There is a prominent peak in channel 360 which we interpret as being the n-α_o peak of a state in Cr^{48} at 0.72 MeV. Its position also agrees with it being the α_o peak of $N^{15}(He^3, n_o)F^{17}$ but there are several arguments against this identification: This peak and the n_o-α_o peak show up with about the same relative yields in the two runs which were made at different energies with different targets made at different times. If the titanium of the target were totally nitrided, the F^{17} n_o-α_o peak would be about 50% larger than the Cr^{48} n_o-α_o peak. However, the targets used were silver-colored both before and after bombardment instead of the yellow-bronze color of titanium nitride. In the targets used for the $Ti^{46}(He^3, p)V^{48}$ measurements, it was possible to see protons from $N^{14}(He^3, p)O^{16}$; their yield suggested about 2% nitration.

The standard subtraction technique reveals another state at 2.37 MeV and suggests the possible existence of several more at energies of 2.79, 3.11 and 3.51 MeV.

We feel that our identification of the ground state of Cr^{48} is quite certain but the excited states mentioned above are all questionable because of the poor statistics, our inability to obtain a kinematics check, and the presence of an unidentified light contaminant. One other feature adds to the uncertainty: the targets used were only 84.5% Ti^{46}, the remainder being Ti^{47-50}. In particular the targets were 11.1% Ti^{48} which has a (He^3, n_o) Q value of 8.627 MeV so that states in Cr^{50} could well contribute to the spectrum.

The nucleus Cr^{48} was first identified by Rudstam et al., (1952). They bombarded iron targets with 340-MeV protons to study the cross section for the formation of different spallation and fission products. The target was dissolved and chemically separated into the different elements produced. In the chromium fraction, after

subtraction of a 26.5 day Cr^{51} activity, they found a new activity with a half life of 23.5 hours. This was identified as Cr^{48} by the growth and decay of V^{48}. From the relative activities of Cr^{48} and V^{48}, they were able to deduce that Cr^{48} decays mostly, if not entirely, by electron capture. Lieshout et al., (1955) made Cr^{48} by bombarding nickel with 300-MeV protons and chemically separating the chromium produced. They saw no positron decay and estimated it to be less than 2%. Two gamma rays of approximately equal intensity were seen in the decay. Their internal-conversion coefficients were measured to determine their multiplicity. Then, using beta-decay systematics, they estimated the Cr^{48}-V^{48} mass difference to be 1.45 ± 0.2 MeV. Sheline and Wilkinson (1955) chemically separated the chromium produced in the reaction Ti^{46}(50-MeV α, 2n)Cr^{48} and saw the same gamma-ray spectrum as Lieshout et al. Using the internal-conversion data of Lieshout et al., they estimated the mass difference Cr^{48}-V^{48} as 1.724 ± 0.200 MeV. Our measured value for the mass difference is 1.657 ± 0.019 MeV.

3.6 The Ni^{56} nucleus

The Q value for the reaction $Fe^{54}(He^3, n_o)Ni^{56}$ was found to be 4513 ± 14 keV. This result is the average of three independent sets of runs, one of which is shown in figure 27. The error quoted was calculated from estimations of the experimental uncertainties, the largest of which was the exact value of the beam energy; the standard deviation computed from the three independent measurements is also about 14 keV.

Three (and perhaps five) excited states of Ni^{56} are visible in the data of figure 27. In the raw spectrum (top), the first three peaks of the n_1 family i.e., the α_o, α_1 and α_2 peaks of the first excited

state of Ni^{56} (at 2.69 MeV excitation) are clearly visible. The n_1-p_{01} peak looks abnormally high and, as can be seen from the middle spectrum (n_o and n_1 subtracted), coincides with the α_o peak of an excited state at 3.95 MeV.

Two subtractions were performed to obtain the middle spectrum. The n_o family of peaks was subtracted with one of the $Be^9(\alpha, n)$ calibration spectra taken for the Ni^{56} ground state. Unfortunately, the n_1 subtraction could not be performed as easily since none of the n_1 calibration spectra was sufficiently close in neutron energy to provide a good subtraction. However, the data of figures 13 and 16 to 18 could be used to deduce the relative ratios of the peaks produced by a neutron with the same energy as n_1. The individual peaks of the calibration spectrum closest to n_1 were scaled using these ratios and the resultant spectrum shifted in channel number for optimum match and subtracted out.

In the bottom spectrum, peaks due to $Mg^{24}(He^3, n_o)Si^{26}$, $Si^{28}(He^3, n_o)S^{30}$ and $C^{12}(He^3, n_o)O^{14}$ have been subtracted. The magnesium, silicon and carbon were present on the target as contaminants. The subtractions reveal another state in Ni^{56} and the first excited state of Si^{26}.

The O^{14} subtraction spectrum was obtained by bombarding a carbon target but we did not have good calibrations for the Si^{26} and S^{30} peaks. However, we had taken a large number of $Be^9(\alpha,n)C^{12}$ calibration spectra for the ground state of Ni^{56} and, fortuitously, we found that among these spectra there were ones in which the neutron to the first excited state of C^{12} (hereafter called $\bar{n}_1$) had an energy very close to the n_o energies of Si^{26} and S^{30}. The height of the $\bar{n}_1$ peaks is 10-15 times larger than the $\bar{n}_o$ peaks, both because of a larger cross section for the neutron absorption events in silicon and

because the reaction $Be^{9}(\alpha, n)$ populates the first excited state of C^{12} more strongly than the ground state. The Si^{28} + n yield curve spectra of Chapter IV, section 4, were examined to estimate how much $\bar{n}_0$ structure was under the $\bar{n}_1$ spectrum. It was small enough relative to the $\bar{n}_1$ structure to be ignored.

From the data of figure 27, the excitation energy of the first excited state in Si^{26}, whose α_0 peak is revealed clearly only after five subtractions, is found to be 1.78 MeV. This compares with the value 1.787 ± 0.027 found in section 3.1.

As in all cases studied, a long run was made with the detector at 30^{o}. All of the peaks in figure 27 underwent a kinematic shift consistent with the identifications made (except the two peaks labelled Ni^{56} in the top spectrum between channels 200 and 225 which were not seen in the 30^{o} run and are discussed later).

Many groups have investigated the decay of Ni^{56}. They all found a half life of about 6 days. Sheline and Stoughton (1952), and Wells et al., (1963) both put an upper limit of 1% on any positron emission. Thus the decay appears to take place entirely by electron capture. Wells et al., the first group to have constructed a decay scheme, give a summary of work done previous to theirs. It all involved chemical separation of Ni^{56} produced by beam activation of a metal foil, and study of the gamma rays produced in the decay. Wells et al. bombarded natural iron foils with 30-MeV alpha particles. After allowing one to two weeks for the short-lived activities to decay, the Ni^{56} was chemically separated from the target and the gamma-ray spectrum resulting from its decay examined with NaI (Tl) scintillation gamma-ray spectrometers, singly, in coincidence and in delayed coincidence. These measurements, along with angular-correlation measurements, permitted the construction of a decay scheme and

the assignment of spin and parity values to all the states of Co^{56} populated by the decay. More recently, Ohnuma et al., (1965) have performed almost the same experiment and obtained very similar results. They measured internal-conversion electrons and angular-correlation functions for all coincident gamma-ray pairs.

The first determinations of the mass of Ni^{56} were made simultaneously by Hoot, Kondo and Rickey (1963, 1965) and Miller, Kavanagh and Goldring (1963). Our work has been described above. Hoot et al. investigated the reaction $Ni^{58}(p, t)Ni^{56}$ at a proton energy of 28 MeV using a (dE/dx)-E counter telescope. They measured a Q value of -13.987 ± 0.018 MeV and found excited states of Ni^{56} at 2.71, 3.94, 4.97, 5.35, and 6.62 MeV. By measuring the triton angular distribution, they were able to deduce that the ground and first excited states of Ni^{56} probably have spin and parity of 0^+ and 2^+ respectively.

The levels at 2.71, 3.94 and 6.62 MeV seen by Hoot et al. agree well with our work. In addition, we have weak evidence in support of the 4.97 and 5.35 MeV states. Using their numbers, the α_o peaks of these states should lie in channels 224 and 213 in the data of figure 27 and indeed weak peaks are apparent at both these locations. They are, however, washed out in the subtractions. The two other sets of Ni^{56} runs show similar weak peaks in the correct locations. Knowing where to look, we can see that these states might be present but otherwise we would not have attached any significance to the small anomalies observed at these locations.

3.7 The Zn^{60} nucleus

Figures 28 and 29 present one of two sets of independent runs in which the $Ni^{58}(He^3, n)Zn^{60}$ Q value was found to be 818 ± 18 keV. An excited state is seen at an energy of 1019 ± 25 keV. The very strong groups produced by carbon contamination prevented the location of higher excited states.

Lindner and Brinkman (1955) observed Zn^{60} obtained from chemical separation of natural nickel bombarded with 52-MeV alpha particles. Using a liquid scintillator, a new gamma-ray activity with a half life of 2.1 ± 0.1 minutes was found. This they attributed to the decay of Zn^{60} formed by the reaction $Ni^{58}(\alpha, 2n)Zn^{60}$. Gamma-ray activities resulting from the decay of Zn^{61} and Zn^{62} were also observed. Using a scintillation detector, weak gamma rays were observed from 0.5 to 3 MeV. They were unable to decide if these resulted from the decay of Zn^{60} or Zn^{61}.

4. Discussion

This section compares the mass and excitation-energy measurements with theoretical and semi-empirical predictions. The four nuclei Si^{26}, S^{30}, Ar^{34}, and Ti^{42} are the proton-rich members of isotopic-spin triplets the other two members of which are well known. Thus, assuming charge symmetry of nuclear forces, their masses may be estimated by calculating the Coulomb-energy correction. If one assumes that the Coulomb energy is proportional to $Z(Z-1)/R$ and further assumes that R is constant for isobars, one obtains

$$\Delta M = \frac{A}{A-2}\,(\Delta M' + 0.782) - 0.782$$

where ΔM and $\Delta M'$ are respectively the mass differences (in MeV) between the proton-rich and center isobars, and the center and neutron-rich isobars. For the center (Z = N) isobar, one actually uses the mass of the nucleus in its lowest T = 1 state. Our results are compared with this formula in table 6. Included in the table is a comparison of the excited states of the proton-rich and neutron-rich isobars. The measurements agree well with the predictions of charge symmetry, as is usually the case.

The three nuclei Cr^{48}, Ni^{56} and Zn^{60} are even. This makes it very difficult to estimate their mass because the only consistently reliable technique for estimating unknown masses is the use of charge symmetry and that cannot be applied here. (The above three nuclei are charge symmetric with themselves and themselves only.) However, Everling (1963b) was able to obtain mass estimates for Cr^{48} and Ni^{56} by considering the mass trend of all even nuclei in the $f_{7/2}$ shell. He first observed (Everling (1963a)) that a plot of the mass defect (plus a term proportional to A) vs. A for even nuclei in the $d_{5/2}$ shell (Ne^{20}, Mg^{24}, Si^{28}) was nearly a straight line and that an extrapolation of this line towards lower A gave a value for the mass defect of O^{16} (doubly magic, $p_{1/2}$ shell closure) corresponding to the nucleus being in its first-excited state, the 0^+ state at 6.05 MeV. He then made a similar plot for the even nuclei of the $f_{7/2}$ shell (Ti^{44}, Cr^{48}, Fe^{52}, Ni^{56}), the line being drawn from the first-excited, 3.35-MeV, 0^+ state of Ca^{40} (doubly magic, $d_{3/2}$ shell closure) up through Fe^{52}. The nucleus Ti^{44} falls slightly below the line (as did Ne^{20} for the $d_{5/2}$ shell plot) but he expected that Cr^{48} and Ni^{56} should lie on the line (as did Mg^{24} and Si^{28}) and read off values for their mass excesses. His estimates of the energy available for beta decay (the number of interest in the

e-process) are given in table 7 along with values deduced by combining the (He^3, n) Q values of this chapter with the (He^3, p) Q values of the next chapter. Everling's estimates agree very well with the experimental values.

5. The $Si^{28}(He^3, n)S^{30}$ angular distribution

The angular distributions of neutrons to the ground and first excited states of S^{30} were measured at a bombarding energy of 11.6 MeV in steps of 10^o from 0^o to 50^o with a semiconductor detector 1 cm in diameter. At each angle, the detector subtended an angle of 10.0^o. The yield was determined by summing the number of counts in the $Si^{28}(n, \alpha_o)$ peak and correcting the result for variations in the α_o cross section using the data of figures 12 and 13. A series of $Be^9(\alpha, n)$ calibration spectra covering the same neutron-energy range as the S^{30} ground-state neutron was also taken to facilitate subtraction of counts due to the ground-state neutron from beneath the $Si^{28}(n_1, \alpha_o)$ peak of S^{30}.

The angular distributions found for n_o and n_1 resemble typical stripping patterns (see figure 30). With this in mind, the ground-and excited-state distributions were fitted with spherical Bessel functions, the best fits being obtained with $j_o^2(kR)$ and $j_2^2(kR)$ respectively where k is the momentum transfer and R is the interaction radius taken as 5.0 fm to obtain the best fit. A justification for this procedure may be found in the work of Glendenning (1962) who has considered the similar case of (α, d) stripping. These fits, normalized to the experimental points at 0^o, are indicated by the solid lines in the figure. If one assumes a small probability for spin-flip, the two protons captured in the (He^3, n) reaction must be in a singlet state because this is their state in He^3. Since the ground state of Si^{28} is 0^+,

the spins and parities of the levels populated in S^{30} are given directly by the ℓ-value of the angular distribution. Thus the ground and first excited states of S^{30} are 0^+ and 2^+ respectively as is expected on the basis of charge symmetry (see levels of Si^{30} in Endt and Van der Leun (1962)).

VI. THE (He^3, p) MEASUREMENTS

1. Introduction

This chapter describes the results of (He^3, p) Q-value measurements for reactions leaving V^{48}, Co^{56} and Cu^{60} in the final state. Upon combining these with the (He^3, n) Q values obtained in the preceding chapter for Cr^{48}, Ni^{56} and Zn^{60}, one can accurately establish the energy available in, for example, the decay of Ni^{56} to Co^{56}. Thus, the Ni^{56}-Co^{56} mass difference, ΔM, is related to the ground state Q values Q_p and Q_n of $Fe^{54}(He^3, p)Co^{56}$ and $Fe^{54}(He^3, n)Ni^{56}$ by

$$\Delta M = Q_p - Q_n - (M_n - M_H)$$

a result which does not require knowing the masses of anything other than hydrogen and the neutron. Also, the advantage of being able to use the same target material (and even the same target) for both Q-value measurements eliminates many possible sources of systematic error. The mass differences obtained, particularly the Ni^{56}-Co^{56} difference, are important parameters in the e-process (see Chapter II). The emphasis during the (He^3, p) measurements was to obtain accurate ground state Q values but with very little additional effort it was also possible to find many excited states.

2. Procedure

Targets of Ti^{46}, Fe^{54} and Ni^{58} were bombarded with an 11.5 to 12.0-MeV He^{3++} beam from the ONR-CIT tandem accelerator and the protons produced were analyzed with the ONR-CIT 61-cm

magnetic spectrometer. The protons analyzed always had an energy of 12 MeV or more. They were detected in an array of 16 semiconductor detectors located in the focal plane of the magnet. Before being detected, the particles traversed approximately 1/2 mm of aluminum, a thickness sufficient to remove all particles other than protons. In particular, this removed deuterons, an important consideration since the reactions $Fe^{54}(He^3, d)$ and $Ni^{58}(He^3, d)$ were observed to compete strongly with the (He^3, p) reactions being investigated.

The targets consisted of isotopically enriched Ni^{58}(99%), Fe^{54}(97%) and Ti^{46}(84.5%) evaporated respectively to thicknesses of 150, 50 and 20 $\mu g/m/cm^2$ onto gold foils approximately 2000 A thick. The gold foils were prepared by evaporating gold onto glass slides on which barium iodide (which is very water soluble) had been previously evaporated. The foils were then cut up, floated off in distilled water, caught on tantalum frames and glued down with glyptal.

Measurements were made at three angles to facilitate the separation of the proton groups of interest from contaminants. Small angles (15^o - 45^o) were chosen on the assumption that stripping is the dominant reaction mechanism, in which case the yield should be greater in the forward direction. This appeared to be true for the limited number of angles checked. A nuclear magnetic resonance probe was used to measure the magnetic field and the results are presented graphically versus the frequency of this magnetometer. In addition, the ground-state proton groups were calibrated with the reaction $Be^9(He^3, p)B^{11}$ ($Q = 10325.1 \pm 0.7$ keV). The two different evaluations of the ground-state proton energies agreed to within a few keV.

The first measurement of the Co^{56} mass was done in a manner slightly different than described above. The target was one of those previously used to measure the $Fe^{54}(He^3, n)Ni^{56}$ Q value. It was possible to find a single bombarding energy (8.213 MeV) and angle (90^{o}) such that the calibration and unknown proton groups had the same energy. Thus both the Co^{56} measurement and the calibration were made without changes in beam alignment which greatly reduced error. However, at this bombarding energy, the yield was many times lower than at 12 MeV.

The spectrum, which was taken without a foil over the array detectors, showed some poorly-resolved structure between 150 and 450 keV excitation in Co^{56} possibly due in part to three low-lying levels in Co^{56} reported by Nelson et al. (1962) but not seen by other groups. It was decided to repeat the experiment with better resolution. The desired resolution could not be achieved with the 16 counter array and to repeat the experiment with a single detector collimated tightly enough to give this resolution would have taken too much running time. Therefore, it was decided to use nuclear emulsions as the detector in the focal plane of the spectrometer.

Ilford K2 nuclear emulsions 100μ thick on glass plates 1" x 6" were obtained. (These should be ordered "with extra plasticizer". Otherwise the emulsion cracks and peels from its glass backing when put in vacuum - a phenomenon discovered the hard way!) A device was built which holds three plates in the spectrometer chamber and allows them to be rotated into the focal plane one at a time from outside the vacuum system. A sheet of aluminum, 0.08 mm thick, was wrapped around the holder and served as a light shield. This aluminum should not touch the emulsion surface as it produces rapid blackening. Three exposures

were made lengthwise on each plate. The central exposure was $Fe^{54}(He^3, p)Co^{56}$ and the two side exposures were $Be^9(He^3, p)B^{11}$ to be used for calibration.

The emulsions were developed following directions given by Barkas (1963) and scanned using a microscope. Except for better resolution of the previously-resolved peaks, the spectrum was identical to the one obtained with the 16 counter array. In particular, the poorly-resolved structure looked little different than before. Later, it was discovered that this structure is probably due to deuterons as it disappears when a sufficiently thick foil is put in front of the array. The structure is not due to groups from $Fe^{54}(He^3, d)Co^{55}$ although groups from this reaction are visible at lower proton energies. In any case, the low-lying Co^{56} levels reported by Nelson et al. are probably spurious.

3. Results and discussion

Figures 31 and 32 show sample proton spectra obtained in the He^3 bombardment of Fe^{54} and Ni^{58}. Tables 9 and 10 list the energy levels found. The same lettering (i. e., A for the highest energy proton group) is used in both figures and tables. Errors were assigned by comparing the spectra obtained at different angles.

Table 11 lists the ground-state Q values measured. The error is primarily due to uncertainty in the beam energy. Table 7 lists the mass differences which are of interest in the e-process. Figures 33 and 34 summarize the work done on mass numbers 56 and 60.

Our results on V^{48} are very incomplete: the targets were very thin which prevented obtaining a reasonable count rate except at very forward angles and at these angles the ground state of V^{48}

was obscured by peaks from $N^{14}(He^3, p)O^{16}$. The excited states we see (table 8) agree well with other measurements and since the mass excess of V^{48} is known to an accuracy of 3.4 keV, we did not pursue the matter further.

There are variations of nearly two orders of magnitude in the yields of various proton groups in the reaction $Fe^{54}(He^3, p)Co^{56}$ as may be seen in figure 31. (Note in particular the scale change at f = 39.25.) This was true at the three different angles examined (15^o, 30^o, and 90^o). From the work of several authors (see table 9 footnotes), it is probable that levels A, B, D, G, K, and M have spins and parities of 4^+, 3^+, 5^+, 2^+, 1^- (2^-) and 1^+ respectively. By comparing the yield to each state with its spin, it is seen to be generally true that the higher the spin, the lower the yield.

The nucleus Co^{56} is one neutron over and one proton under the double shell closure at Z = N = 28. The expected low-lying shell-model configurations for the odd particle and hole are $(1f_{7/2})^{-1}(2p_{3/2})$ (giving rise to 2^+, 3^+, 4^+, and 5^+ states) and $(1f_{7/2})^{-1}(1f_{5/2})$ (giving rise to 1^+, 2^+, 3^+, 4^+, 5^+ and 6^+ states). Wells (1965) has performed some shell-model calculations which indicate that levels A, B, D and G belong to (and complete) the $(1f_{7/2})^{-1}(2p_{3/2})$ configuration. He also makes a partial assignment of levels to the $(1f_{7/2})^{-1}(1f_{5/2})$ configuration. However, peak K, which Wells assumes to be 2^+ and uses as a parameter in his calculations has been measured to be 1^- (2^-) by Ohnuma and Hashimoto (1965). (Wells et al. (1963) had deduced experimentally that this level was (1^-, $2^\pm$).) On the basis of the yield considerations mentioned above, levels F, I, J and L might be the high-spin members of the configuration.

The ground state of Cu^{60} is $2^{(+)}$ from beta-decay studies. No other information is available as the level structure has not been

previously investigated. The approximate number of low-lying states can be readily explained using the shell model. The Cu^{60} nucleus may be pictured as three neutrons and one proton outside an inert core bounded by the completely filled $f_{7/2}$ shell. Two of these neutrons will be paired with a binding energy of about 1.5 MeV. Thus, on the basis of the Co^{56} structure, the lowest shell-model configuration of Cu^{60} is $(2p_{3/2})^1_n (2p_{3/2})^1_p$ giving rise to four states ($0^+ - 3^+$). Again using the Co^{56} data, about 0.8 MeV is required to move a $2p_{3/2}$ particle to the $1f_{5/2}$ shell. This gives rise to two sets of four states ($1^+ - 4^+$) depending upon whether the odd proton or neutron is excited. The next group of states will start around 1.5 MeV and will arise from breaking the coupled pair of neutrons (many states), exciting the pair to the $1f_{5/2}$ shell (4 states, $0^+ - 3^+$), or excited both uncoupled particles to the $1f_{5/2}$ shell (6 states, $0^+ - 6^+$). One conclusion is that 12 states are expected below 1.5 MeV, in fair agreement with the data. Note in figure 34 the rather well defined group of 10 states (including the ground state) ranging up to 940 keV. Two states could have been easily missed in this interval.

VII. THE GAMMA-RAY MEASUREMENTS

1. Introduction

This chapter reports two measurements of gamma-ray spectra which are only indirectly related to the main theme of the thesis but which produced some interesting results.

Section 2 describes a measurement of the Ar^{34} half life. The ground states of Ar^{34}, Cl^{34}, and S^{34} form a 0^+, T = 1 isotopic-spin triplet. Thus the ground-state beta decays of Ar^{34} and Cl^{34} (both positron emitters) should be superallowed and, according to the CVC theory, have identical log ft values. The mass of Ar^{34} had already been measured (see page 55) and, since this nucleus has never been reported, it was decided to investigate its decay. The Ar^{34} was produced in the reaction $S^{32}(He^3, n)Ar^{34}$. Its decay produces Cl^{34} which is also produced via $S^{32}(He^3, p)Cl^{34}$. One expects the two isotopes to have similar half lives, making them difficult to separate. For the measurement to succeed by the method used, it was essential that Ar^{34} have a detectable decay branch to an excited state of Cl^{34}. The subsequent gamma ray could then be used as a signature for Ar^{34}. Such a gamma ray was found.

Section 3 describes the gamma-ray spectrum obtained from the de-excitation of excited states in Ni^{56} populated by the reaction $Fe^{54}(He^3, n)Ni^{56}$. Section 4 gives a brief discussion of the evidence in favor of collective structure in Ni^{56}, Ca^{40} and O^{16}, all of which are doubly magic.

2. Decay of Ar^{34}

The half life of Ar^{34} (estimated to be about 1 sec) was measured by looking for gamma rays from Cl^{34} following the decay of Ar^{34} produced in the reaction $S^{32}(He^3, n)Ar^{34}$. A 7.6 cm x 7.6 cm NaI (Tl) crystal was located 2 cm from the target at 90^o in the laboratory. The bombarding energy was 10 MeV and the target consisted of Sb_2S_3 pressed into a hole in a beryllium cylinder 2.54 cm in diameter and 2.54 cm long. The experiment was performed in a beryllium environment for two reasons: the low atomic number of beryllium reduces bremsstrahlung produced by β rays and none of the reaction products of He^3 on beryllium produce delayed γ rays.

An electronic sequence timer initiated the following series of operations: the beam was allowed to strike the target for a time τ and was then chopped. After a short delay (150 ms) to ensure that the beam had died away, gamma rays were successively stored in the first and second halves of the memory of a pulse-height analyzer for the same time τ in each half. Then the analyzer was blocked, the beam turned on again and the cycle repeated. The ratio of the numbers of counts, corrected for background, in the two halves of the memory allows one to estimate the half lives of the gamma rays seen. The timing interval was varied from 1 to 5 times the expected Ar^{34} half life.

Figure 35 shows the delayed-gamma-ray spectrum obtained with one-second timing. Most of the large peaks in the top spectrum (total yield of delayed gamma rays in the first two seconds after beam turn-off) are due to gamma rays from S^{34} which follow the beta decay of the isomeric state of Cl^{34} at 0.143 MeV (see Endt and Van der Leun (1962) and figure 36). The $Cl^{34\ m}$ is formed

predominantly by the reaction $S^{32}(He^3, p)Cl^{34}$. Its half life was measured by monitoring the target activity for 45 minutes after the beam was removed and found to be 32 ± 1 min in good agreement with the accepted value of 32.40 ± 0.04 min. The relative yields of the S^{34} gamma rays were measured and are listed in table 12.

Once the S^{34} gamma rays were positively identified both by virtue of their half life and their energy (determined with a calibration using Co^{60} and RdTh sources), they were used as an internal energy calibration. This enabled the energies of the other gamma rays seen to be determined with a precision of 14 keV or better.

The bottom spectrum of figure 35 shows the yield difference between the first and second seconds after beam turn-off. Note that the S^{34} gamma rays have entirely disappeared, illustrating the advantages of this method for finding gamma rays produced in the decay of short-lived radioisotopes. Only three statistically significant peaks remain. They are located at energies (in MeV) of 0.51, 0.67 and 1.02. The 0.51 and 1.02 peaks are due to annihilation quanta, singly and in random coincidence. The remaining peak, at 0.67 MeV, was found to have a half life of 1.2 ± 0.3 s and is most likely due to the beta decay of Ar^{34} to the 0.67-MeV state of Cl^{34}. The large uncertainty in the measured half life was due to difficulty in determining the background beneath the peak.

Note that an 0.51-MeV gamma ray in either true or random coincidence with the backscatter photon of another 0.51-MeV gamma ray would produce a peak at 0.68 MeV very close to the peak seen. This possibility was eliminated by observing that the 0.67-MeV peak had a unique half life, the same for 1, 1.5, 3 and 6 second timing intervals, whereas the 0.51-MeV peak did not. As a further check,

the spectrum produced by a Na^{22} source inserted in the beryllium chamber was examined using detection geometry similar to that of the actual experiment. No backscatter-sum peak was seen; its intensity was at least ten times weaker than the 0.67-MeV peak seen in the experiment.

A lower limit on the intensity of the beta branch to the 0.67-MeV level may be obtained by comparing the yields of the 0.67-MeV and 0.51-MeV gamma rays in the difference spectrum. This is only a lower limit because much of the short-half-life 0.51-MeV radiation comes from other sources such as the beta decay of the ground state of Cl^{34}. The limit obtained is $1.4 \pm 0.2\%$. This has already been corrected for the gamma-ray branching ratio of the 0.67-MeV level which, according to Glaudemans et al. (1964) decays directly to the ground state 80% of the time and cascades through the 0.14-MeV level 20% of the time. In our experiment, the 0.53-MeV gamma ray was swamped by annihilation radiation and the 0.14-MeV gamma ray was below the analyzer cut-off. In any case, the 0.14-MeV gamma ray is useless for measuring the half life of Ar^{34} because the 0.14-MeV state of Cl^{34} is the isomeric state.

Using our values for the Ar^{34} - Cl^{34} mass difference and Ar^{34} half life, we calculate log ft = 3.59 ± 0.11 for the Ar^{34} decay. This value confirms that the decay is superallowed and agrees well with the value of log ft = 3.508 ± 0.010 calculated for the Cl^{34} ground-state decay. Both these values have been calculated using a computer program for f developed by Bahcall (1965). Our Ar^{34} measurements, particularly the half-life measurement, are not sufficiently accurate to really test the CVC theory.

Using the lower limit obtained for the branching ratio of the Ar^{34} decay to the 0.67-MeV state of Cl^{34}, we calculate log ft $\lesssim 5.5$ for this transition. Therefore, the 0.67-MeV level of Cl^{34} is 1^+.

The results on mass 34 are summarized in figure 36.

3. Gamma rays from Ni^{56}

Gamma rays produced in the reaction $Fe^{54}(He^3, n\gamma)Ni^{56}$ at a bombarding energy of 11.6 MeV were studied in a 10.2 cm x 10.2 cm NaI (Tl) crystal. Unfortunately, gamma rays from Co^{56}, produced by $Fe^{54}(He^3, p)$, as well as gamma rays from reactions involving target contaminants swamped the gamma-ray spectrum as seen in a single NaI crystal so that it was necessary to use an n-γ coincidence system. The neutron detector was placed at 0^o where the neutron yield is expected to be largest on the basis of stripping theory, and the gamma-ray detector was located at 90^o. Coincidences between the two detectors were used to gate the gamma-ray event into a 100 channel pulse-height analyzer.

The biggest problem was to obtain a neutron-detection system which did not respond to gamma rays. We first tried to stilbene crystal with pulse shape discrimination but were unable to get satisfactory neutron-gamma-ray separation over the broad range of neutron energies present (up to 16 MeV). Our eventual solution was to "range limit" the gamma rays by using a small cylinder (1.27 cm diameter, 0.63 cm thick) of NE102 plastic scintillator (supplied by Nuclear Enterprises Ltd., Winnipeg, Canada) and make use of the fact that the rate of energy loss for proton recoils is greater than for Compton scattered electrons. Thus, in this piece of scintillator, the maximum pulse height that an electron could produce was less than that of the more energetic proton recoils produced by n_5(6.60-MeV state), which had an energy of 9.4 MeV and was the least energetic neutron of interest. The reaction $Be^9(\alpha, n\gamma_{4.43})$ was used to test the apparatus and to set the integral

bias on the neutron detector. This was chosen as the half-height point in the spectrum of a 9-MeV neutron.

The gamma-ray spectrum obtained with the n-γ coincidence arrangement is shown in figure 37. Despite the poor statistics, due to the extreme inefficiency of the neutron detector, two gamma rays are seen, of energies 1.28 ± 0.06 MeV and 2.66 ± 0.10 MeV. These gamma rays are consistent with a collective interpretation of the levels of Ni^{56} given in the next section.

4. Discussion: Evidence for collective structure in doubly magic nuclei

Recent experimental evidence suggests that the doubly magic nuclei O^{16}, Ca^{40}, and Ni^{56} have pronounced collective properties. The nucleus O^{16} shows several well-developed rotational bands (see, e. g., Borysowicz and Sheline (1964)), the lowest of these being based on the 0^+ first excited state at 6.06 MeV. As outlined below, it is possible to construct a rotational band on the 0^+ first excited state of Ca^{40} at 3.35 MeV and it appears that the levels of Ni^{56} may separate into vibrational bands. Work by Everling (1963a, 1963b) on the mass systematics of the $1d_{5/2}$ and $1f_{7/2}$ shells suggests that the 0^+ first excited states in O^{16} and Ca^{40} represent rearrangements of the nuclear structure necessary for adding more particles outside a doubly-closed shell (see the last paragraph of Chapter IV, section 4 for a discussion of Everling's work). It is then perhaps not too surprising that these states might be highly distorted and show collective properties.

The known states of Ni^{56} appear to separate into two vibrational bands or (less likely from the energy spacing) a vibrational band and a rotational band (see figure 38). Hoot et al. (1965) have

weak evidence in support of the 0^+ and 2^+ assignments for the ground and 2.69-MeV states; the remaining assignments are conjecture. Note that the separation of the two 0^+ states is close to being 1.5 times the intraband spacing (which is about 2.7 MeV for both bands). Our gamma-ray data (see figure 37) are consistent with the vibrational interpretation of figure 38, the 2.66-MeV gamma ray being a superposition of all the intraband transitions and the 1.26-MeV gamma ray being the interband transition between the states at 3.95 MeV and 2.69 MeV.

The nucleus Ca^{40} appears to have a rotational band built on the 0^+ state at 3.343 MeV (see figure 39), the formula

$$E(J) = 0.092\ J(J+1)\ \text{MeV}$$

fitting the levels chosen reasonably well. Recent papers by Springer (1965) and Bauer et al. (1965) provide most of the known spin and parity assignments. Both works were cyclotron studies of the angular distribution of alpha particles inelastically scattered from Ca^{40}.

Let us examine the experimental information on the levels in the postulated rotational band one level at a time. The states at 3.348 MeV and 3.900 MeV are definitely 0^+ and 2^+ respectively. The level required to be 4^+ could be any one of a closely spaced triplet around 5.25 MeV, although the one at 5.202 MeV fits best. This triplet was clearly identified by Braams (1956) who studied $Ca^{40}(p, p')$ with a magnetic spectrometer using a proton beam from an electrostatic generator. This triplet could not be resolved in the cyclotron studies. Bauer et al., with a resolution of 120 keV, saw a single weakly excited level at 5.27 MeV which they assigned as 3^- or 1^-.

Springer observed a single weak group at 5.25 MeV whose angular distribution oscillated only feebly but with a phase corresponding to a negative parity state.

Since, in general, positive parity states were weakly excited in the cyclotron studies; it is possible that a 4^+ state would be masked by a nearby negative parity state. If indeed the 0^+, 3.35 MeV state represents an overall rearrangement of the internal structure as suggested in the first paragraph, members of a rotational band based on this state would be excited only weakly by (α, α') because of the small overlap with the ground state wave function.

The state at 7.12 MeV was seen by both groups, again only weakly excited. Bauer et al. estimate its spin and parity as $\geq 6^+$.

A test of the suggested rotational band would be to see if a member of the triplet at 5.25 MeV were indeed 4^+. Probably the simplest experiment is to measure the $Ca^{40}(\alpha, \alpha')$ angular distribution. One way to achieve the necessary resolution would be to use a tandem accelerator and a magnetic spectrometer.

APPENDIX 1

Sample Calculations of the $Si^{28}(n, \alpha_o)Mg^{25}$ Cross Section

1. Correction factors

This appendix presents two sample calculations of the $Si^{28}(n, \alpha_o)$ cross section: one in which the neutron source was $D(d, n)He^3$; the other, $Be^9(\alpha, n_o)C^{12}$. The complete yield curves for all the Si^{28} + n reactions measured are given in figures 12 to 18.

One of the largest sources of error in the measured cross section is uncertainty in the actual active volume of the semiconductor detector (which served as both target and detector). Different detectors were used for the D(d, n) and $Be^9(\alpha, n_o)$ data; the volume of each was measured periodically using a Cs^{137} gamma-ray source of known strength. One of the spectra, from which the volume of the detector used for the D(d, n) data was deduced, is shown in figure 6.

Another large source of error arises from uncertainty in the neutron-production absolute cross section. Values of the D(d, n) cross section at 0^o were taken from Fowler and Brolley (1956) and have a standard deviation of 7% or less. Values of the $Be^9(\alpha, n_o)$ cross section at 0^o were measured by the methods described in Chapter III. The results, which are plotted in figure 3, have a standard deviation of about 20%.

Figures 9 and 10 show typical spectra from the D(d, n) and $Be^9(\alpha, n)$ data respectively. Figure 11 shows the detection geometries and other details relevant to the analysis of these spectra, an analysis which proceeded in the following way. First the α_o peaks were summed over the regions indicated in the figures and the sum obtained, S, multiplied by a factor f which corrects for α particles which

escape through the edges of the detector and a factor D to correct for the analyzer dead time. One can show that

$$f \cong 1 + (t + r)\, R/(2tr)$$

where t and r are the detector thickness and radius and R is the range of the particle being stopped. This formula assumes both uniform and isotropic particle production throughout the detector volume. For 10-MeV neutrons detected in the α_o peak, $f \cong 1.02$, a correction of little importance. However, f is much more important for the proton groups.

Further evaluation of the absolute cross section will be considered for the two neutron sources separately.

2. Cross section from $D(d, n)He^3$ data

In the following calculation, numbers are taken as needed from figures 9 and 11 where the symbols used are defined unless they have been defined above or are obvious.

$$\sigma(\alpha_o) = SfD/(N_1 N_2 N_3)$$
$$= 92.7 \pm 9.5 \text{ mb}$$

The separate quantities in this expression have the following meanings and values:

$$SfD = (3578 \pm 60) \times 1.013 \times 1.023$$
$$= 3705 \pm 62$$

N_1 = Number of D atoms/mb
$= 2P \times 2a/kT$

$= 6.55 \times 10^{-21} \times (43.2 \pm 0.4 \text{ mm Hg}) \times 3.69 \text{ cm}$

$= 1.043 \pm 0.010 \times 10^{-8}$ atoms/mb

N_2 = Number of Si^{28} atoms in detector

= $N\rho/A$ x abundance (Si^{28}/Si) x volume of detector

= 4.80×10^{22} atoms/cm^3 x (0.275 ± 0.020 cm^3)

= $1.322 \pm 0.096 \times 10^{22}$ atoms

N_3 = Number of neutrons incident on detector per atom of target gas

= $Q/e \times d\sigma/d\Omega[0^o, D(d,n)He^3] \times \pi r^2/(h^2 - a^2)$

= $1.687 \times 10^{14} \times (77.7 \pm 5.4 \times 10^{-27}) \times 2.21 \times 10^{-2}$

= $2.90 \pm 0.20 \times 10^{-13}$ neutrons/atom

The expression $\pi r^2/(h^2 - a^2)$ in N_3 is the effective solid angle subtended by the detector. This formula, which is proved by Evans (1955), assumes that the neutron source has no radial extension, an assumption which introduces an error of less than 0.5%.

3. Cross section from $Be^9(\alpha, n_o)C^{12}$ data

In the following calculation, numbers are again taken as needed from figures 10 and 11. The form of the calculation is the same as in the preceding section.

$\sigma(\alpha_o) = SfD/(N_1N_2N_3)$

$= 25.6 \pm 7.2$ mb

SfD = $(1103 \pm 35) \times 1.019 \times 1.082$

$= 1217 \pm 39$

N_1 = Number of Be atoms/mb

= $5.90 \pm 0.94 \times 10^{-9}$ atoms/mb

N_2 = Number of Si^{28} atoms in detector

= 4.80×10^{22} atoms/cm^3 x (0.40 ± 0.06 cm^3)

$= 1.92 \pm 0.29 \times 10^{22}$ atoms

N_3 = Number of neutrons incident on detector per atom of Be.

$= Q/2e \times d\sigma/d\Omega[0^{o},\ Be^{9}(\alpha, n_{o})C^{12}] \times \pi r^{2}/h^{2}$

$= 4.68 \times 10^{14} \times (4.47 \pm 0.90 \times 10^{-27}) \times (0.20 \pm 0.02)$

$= 4.19 \pm 0.94 \times 10^{-13}$ neutrons/atom

Overlapping $Be^{9}(\alpha, n)$ and $D(d, n)$ data were taken for E_n ranging from 11 to 12 MeV. The $Be^{9}(\alpha, n)$ data were about 9% higher throughout this range. Therefore, the entire $Be^{9}(\alpha, n)$ curve has been normalized to the $D(d, n)$ curve by multiplication by 0.918.

APPENDIX 2

Some Observation Concerning Negative Ion Beams

The production of negative ion beams is an essential part of the operation of a tandem accelerator. Negative beams of hydrogen and deuterium are routinely produced, an oxygen beam is fairly simple to obtain, and helium, carbon and sulfur beams are possible. This appendix will describe some investigations performed helping J. DeBoer develop techniques for obtaining a high energy oxygen beam (which was used for Coulomb excitation studies), and some attempts to produce negative neon and sulfur beams (which were to be used for the production of Ni^{56} via the reactions $Ca^{40}(Ne^{20}, \alpha)Ni^{56}$ and $Si^{28}(S^{32}, \alpha)Ni^{56}$).

The negative ion source of the ONR-CIT tandem consists of two units: a positive ion source; and a system consisting of an extraction electrode, focus electrode (Einzel lens), and charge exchange canal. To produce a negative hydrogen beam, hydrogen gas is bled into the positive ion source. Electrons emitted by a tungsten filament ionize the gas and magnetic fields promote the formation of a plasma consisting of ions such as H^+, H_2^+, H_3^+, and electrons. Some of this plasma is extracted from a small hole in the source and is accelerated through 40 keV by the extraction electrode and focussed with the Einzel lens. Next the beam passes through a narrow canal, the exchange canal, which has hydrogen gas continually leaked into it. A small fraction of the beam becomes negatively ionized upon collision with this gas and is again accelerated through 40 keV upon leaving the exchange canal. A magnet (the 20^o magnet) is used to select the particular negative beam desired and the beam is

accelerated to the tandem terminal. Inside the terminal, it goes through another narrow, gas-filled canal (the stripper canal) where a large fraction of the beam is stripped to a positive charge state and re-accelerated upon leaving the terminal. The beam then passes through a 90^{o} analyzing magnet, a set of energy regulation slits, and on into the target room.

In our first attempts to make a negative oxygen beam, we put a mixture of 7% O_2 and 93% H_2 in the source. We were able to obtain up to 1/4 μa of O^{6+} beam on target at an accelerating voltage of 6 MeV. The purpose of the hydrogen was to reduce wear on the tungsten filament in the ion source. Even so, the filament usually lasted only about one day. In an attempt to determine which was the best of the many different negative oxygen beams coming from the source, we measured 20^{o} magnet current vs beam intensity at the Faraday cup near the low energy end of the tandem (i. e., at the low energy tee or LET). One of the curves obtained is shown in figure 40.

All of the peaks below a magnet current of 100 ma are due to hydrogen beams since the same curve is obtained with only hydrogen in the source. The relative magnitude of the different peaks depends upon the lens settings, in particular the setting of the Einzel lens mentioned above. The largest hydrogen beam was always found to be that corresponding to H_3^+ coming out of the source and H^- coming around the 20^{o} magnet (the H_3^+/H^- beam), in agreement with a note in the HVEC instruction manual. The identification of the other peaks is given in the figure. These identifications were made using the fact that the 20^{o} magnet current should be proportional to the square root of the ion energy times ion mass ($I \approx \sqrt{EA}$) if one assumes that all the beam which goes through the 20^{o} magnet has only one negative

charge. With deuterium in the source, the whole spectrum shifts up $\sqrt{2}$ in magnet current as expected. Later, the energy of the different hydrogen peaks was measured with an electrostatic analyzer located at the exit of the 20^{o} magnet. Energies of 80 keV, 60 keV, 53.3 keV and 40 keV were found respectively for the H^{+}/H^{-}, H_2^{+}/H^{-}, H_3^{+}/H^{-} and H^{o}/H^{-} beams as expected.

The peaks above a magnet current of 200 ma in figure 40 are at least partly due to oxygen or oxygen-hydrogen combinations; some of them are explicitly identified in the figure. However, many of these peaks persist with no oxygen in the source and have never been identified. They may be due to various combinations of carbon, nitrogen and hydrogen. We usually used the peak at about 370 ma for an oxygen beam. It is most likely O_3^{++}/O^{-}. Measurements with the electrostatic analyzer established that the peaks at 300 ma and 410 ma predominately have energies of 40 keV and 80 keV and are therefore O^{o}/O^{-} and O^{+}/O^{-} respectively although either member of each pair may have one or more hydrogen atoms attached which may explain the large peak widths.

The next significant advance was made by H. Winkler who noticed that the H^{o}/H^{-} peak has maximum intensity at much higher settings of the exchange gas and Einzel lens than the other hydrogen beams. He concluded that the H^{o}/H^{-} beam was produced in the exchange canal by bombardment of the exchange gas. Thus, an obvious thing to try was to put other gases in the exchange canal. We first tried O_2 in the exchange canal and H_2 in the source. The predominant beam produced was O_2^{o}/O_2^{-} (≈ 10 μa at the LET). This was not very satisfactory because the O_2^{-} ion will not strip to high charge states such as O^{6+} even assuming that the molecule is broken apart by the first collision in the stripper canal and that the

terminal voltage is 6 MeV. The reason is that the individual atoms in the molecule each have only 3 MeV energy on the average and it is the atomic velocity which determines the degree of stripping.

We next tried H_2O in the exchange canal and H_2 in the source and found three peaks at the LET corresponding to H_2O^0/H_2O^- (5 - 10 μa), H_2O^0/OH^- (5 - 10 μa) and H_2O^0/O^- (much weaker). With 6 MeV on the terminal, it was possible to get 1/2 μa of O^{6+} on target - a significant improvement from the old method, not only because the beam was larger but because the ion-source filament now lasted much longer.

Next, attempts were made to produce a negative neon beam. Neither neon in the exchange canal and hydrogen in the source nor vice versa produced a measureable neon beam. With helium in the source and hydrogen in the exchange canal, peaks due to He^+/He^- and He^0/He^- were observed, but with very low intensity (less than 0.1 μa at the LET for He^+/He^-, the stronger of the two).

Attempts to make a negative sulfur beam were more successful. With H_2S in the exchange canal and H_2 in the source, a current of 7 μa was obtained at the LET. The beam consisted of $H_2S^0/(H_2S^- + HS^- + S^-)$, the different negative ions being too similar in rigidity to separate with the 20^0 magnet. Satisfactory regulation of the tandem was obtained on beams up to S^{10+}. For this last beam, an image current of 5 na was obtained at a terminal voltage of 6 MeV. The beam energy was 66 MeV, the highest ever obtained with the ONR-CIT tandem. Positive beam identification was made by observing the beam scattered from a gold foil with a semiconductor detector located at 30^0 with respect to the beam axis. Figure 41 shows the spectrum obtained with the tandem regulating on a 42.4-MeV S^{7+} beam. At this time, argon was being used as the exchange gas. Also, the pumping on the high energy portion of the vacuum

system was not very satisfactory. These two facts explain the very large number of subsiduary peaks seen in figure 41. Due to the poor vacuum, large numbers of charge-exchange collisions could take place between the sulfur beam and argon gas the whole length of the high energy acceleration column. Thus, a small fraction of the sulfur and argon produced with charge states lower than that of the sulfur beam being regulated on will have the correct energy to get around the magnet. Under similar running conditions, an oxygen beam does not have the same large number of satellite beams although such beams were observed when oxygen was used as the stripper gas. Perhaps the sulfur satellite beams are enhanced because the similar masses of sulfur and argon maximize the momentum transfer per collision.

Unfortunately, the above method for producing a sulfur beam has a serious drawback. The H_2S or something derived from it forms a deposit on the ceramic balls which provide insulation for the parts of the ion source at 40 keV. After less than a day of running, arcing in the source is so bad that further operation is impossible and the insulating balls must either be cleaned or replaced. With H_2S in the source and H_2 in the exchange canal, breakdown occurs even faster. Clearly, another source of sulfur would be desirable but a suitable one does not seem to exist. A gas such as SO_2, if used in the exchange canal, would probably form beams such as SO_2^- and SO^-. Molecules such as these would not have enough velocity to be stripped to high charge states i. e., they would behave like the O_2^- ions discussed previously.

One further difficulty remains. It was discovered that the interval diameter of the exchange canal had been reduced twofold by the formation of a metallic deposit. After this had been reamed out,

it was no longer possible to produce large beams from the gas in the exchange canal, probably because much higher exchange gas pressures are required for this method to work effectively (this was confirmed directly for the H^{o}/H^{-} beam -- see above). A twofold increase in the exchange canal diameter increases the conductance between 8 and 32 times, depending on the pressure. After the exchange canal has been cleaned out, there was some evidence that the ion source produced a larger hydrogen beam. Therefore, the idea of reducing the exchange canal diameter was not very popular.

At this point, Dr. Kavanagh suggested that the reaction $Fe^{54}(He^{3}, n)Ni^{56}$ would be superior to heavy ion beam reactions for the study of Ni^{56}. It was, and further work on heavy ion beams was discontinued.

REFERENCES

J. H. Aitken and W. R. Dixon, 1965, Nuclear Physics 67, 395.

F. Ajzenberg-Selove and K. L. Dunning, 1960, Phys. Rev. 119, 1681.

F. Ajzenberg-Selove and T. Lauritsen, 1959, Nuclear Physics 11, 1.

J. D. Anderson, C. Wong and J. McClure, 1962, Nuclear Physics 36, 161.

R. C. Axtmann and D. Kedem, 1965, Nucl. Instr. and Meth. 32, 70.

J. N. Bahcall, 1965, to be published in Nuclear Physics.

W. H. Barkas, 1963, "Nuclear Research Emulsions", Vol. 1, Academic Press, New York.

R. W. Bauer, A. M. Bernstein, C. Heymann, E. P. Lippincott and N. S. Wall, 1965, Physics Letters 14, 129.

M. Birk, G. Goldring and P. Hillman, 1963, Nucl. Instr. and Meth. 21, 197.

J. H. Bjerregaard, P. F. Dahl, O. Hansen and G. Sidenius, 1964, Nuclear Physics 51, 641.

J. Borysowicz and R. K. Sheline, 1964, Physics Letters 12, 219.

C. M. Braams, 1956, Phys. Rev. 101, 1764.

H. W. Broek and C. E. Anderson, 1960, Rev. Sci. Instr. 31, 1063.

F. E. Clifford and R. Tayler, 1965, Memoirs R. A. S. 69, 21.

L. Colli, I. Iori, M. G. Marcazzan and M. Milazzo, Nuclear Physics 43, 529.

W. M. Deuchars and G. P. Lawrence, 1961, Nature 191, 995.

P. M. Endt and C. Van der Leun, 1962, Nuclear Physics 34, 1.

R. D. Evans, 1955, "The Atomic Nucleus", McGraw-Hill, New York, p. 737.

F. Everling, 1963a, Nuclear Physics 40, 670.

F. Everling, 1963b, Nuclear Physics 47, 561.

H. Flicker, 1963, Rev. Sci. Instr. 34, 822.

J. L. Fowler and J. E. Brolley Jr., 1956, Rev. Mod. Phys. 28, 103.

W. A. Fowler and F. Hoyle, 1964, Ap. J. (Suppl.) 9, 201.

G. Frick, A. Gallmann, D. E. Alburger, D. H. Wilkinson and J. P. Coffin, 1963, Phys. Rev. 132, 2169.

J. L. Gammel, 1960, "Fast Neutron Physics", Vol. 2 ed. by J. B. Marion and J. L. Fowler, Interscience, New York, p. 2185.

J. H. Gibbons and R. L. Macklin, 1959, Phys. Rev. 114, 571.

P. W. M. Glaudemans, L. Eriksson and J. A. R. Werkhoven, 1964, Nuclear Physics 55, 559.

N. K. Glendenning, 1962, Nuclear Physics 29, 109.

E. L. Haines and A. B. Whitehead, 1965, to be published in Rev. Sci. Instr.

E. M. Henley and D. U. L. Yu, 1964, Phys. Rev. 135, B1152.

R. Hofstadter, 1956, Rev. Mod. Phys. 28, 214.

C. G. Hoot, M. Kondo and M. E. Rickey, 1963, Bull. Amer. Phys. Soc. 8, 598.

C. G. Hoot, M. Kondo and M. E. Rickey, 1965, Nuclear Physics 71, 449.

C. H. Johnson and C. C. Trail, 1956, Rev. Sci. Instr. 27, 468.

R. G. Johnson, L. F. Chase and W. L. Imhof, 1960, Bull. Amer. Phys. Soc. 5, 406.

R. van Lieshout, D. H. Greenberg, L. A. C. Koerts and C. S. Wu, 1955, Phys. Rev. 100, 223.

L. Lindner and G. A. Brinkman, 1955, Physica 21, 747.

B. Mainsbridge, T. W. Bonner and T. A. Rabson, 1963, Nuclear Physics, 48, 83.

J. B. Marion and J. L. Fowler, 1960 eds. "Fast Neutron Physics" Vol. 1, Interscience, New York.

J. H. E. Mattauch, W. Thiele and A. H. Wapstra, 1965, Nuclear Physics 67, 1.

R. G. Miller, R. W. Kavanagh and G. Goldring, 1963, Bull. Amer. Phys. Soc. 8, 599.

J. W. Nelson, H. S. Adams, R. H. Davis, J. D. Fox, N. P. Heydenburg, H. S. Plendl, R. K. Sheline and G. M. Temmer, 1960, Bull. Amer. Phys. Soc. 5, 424.

J. W. Nelson, H. S. Plendl and R. H. Davis, 1962, Phys. Rev. 125, 2005.

J. D. Oberholtzer, 1962, PhD Thesis, Florida State University (unpublished).

H. Ohnuma and Y. Hashimoto, 1965, Nuclear Physics 66, 337.

J. D. Pearson, 1963, PhD Thesis, California Institute of Technology, p. 19.

E. M. Pell, 1960, J. Appl. Phys. 31, 291.

T. A. Rabson, 1965, private communication.

J. R. Risser, J. E. Price and C. M. Class, 1957, Phys. Rev. 105, 1288.

E. L. Robinson and O. E. Johnson, 1960, Phys. Rev. 120, 1321.

E. L. Robinson, J. I. Rhode and O. E. Johnson, 1961, Phys. Rev. 122, 879.

G. Rudstam, P. C. Stevenson and R. L. Folger, 1952, Phys. Rev. 87, 358.

A. R. Sattler, 1965, Phys. Rev. 138, A1815.

J. B. Seaborn, G. E. Mitchell, N. R. Fletcher and R. H. Davis, 1963, Phys. Rev. 129, 2217.

R. K. Sheline and R. W. Stoughton, 1952, Phys. Rev. 87, 1.

R. K. Sheline and J. R. Wilkinson, 1955, Phys. Rev. 99, 165.

A. Springer, 1965, PhD Thesis, Berkeley (unpublished).

C. D. Swartz and G. E. Owen, 1960, "Fast Neutron Physics", Vol. 1, ed. by J. B. Marion and J. L. Fowler, Interscience, New York, p. 211.

T. Tohei, 1960, J. Phys. Soc. Japan 15, 372.

H. Tyren and P. A. Tove, 1954, Phys. Rev. 96, 773.

A. H. Wapstra, 1965, private communication.

D. O. Wells, S. L. Blatt and W. E. Meyerhof , 1963, Phys. Rev. 130, 1961.

D. O. Wells, 1965, Nuclear Physics 66, 562.

W. Whaling, 1958, Handbuch der Physik 34, 193; and also D. Demirlioglu and W. Whaling, private communication.

Table 1

Resonances in $Be^{9}(\alpha, n)C^{12}$ for E_α above 4.0 MeV

E_α at resonance (MeV)			Excitation energy in C^{13} (MeV)	Approximate level width (keV) present work
Gibbons and Macklin[a]	Seaborn et al.[b]	Present work[c]		
4.50	4.45		13.8	
5.00	5.00		14.1	
	5.3		14.3	
		5.40 ± 0.10	14.39	240
5.75	5.7		14.64	
		6.20 ± 0.05	14.95	400
	(7.1)	7.10 ± 0.05	15.57	210
7.8	7.7		16.1	
		7.95 ± 0.05	16.16	240
		9.10 ± 0.05	16.96	380
		9.7 ± 0.10	17.37	140
		10.2 ± 0.05	17.72	280
		11.1 ± 0.05	18.34	400
		11.70 ± 0.03	18.76	80

a) Resonances in the total neutron cross section summed over all angles, measured up to E_α = 8.2 MeV. See Gibbons and Macklin (1959).

b) Resonances in the $\gamma_{4.43}$ yield at 0° measured up to E_α = 10.0 MeV. See Seaborn et al. (1963).

c) Resonances in the n_o yield at 0°. See page 22.

Table 2

Important Neutron-Induced Reactions in Silicon*

Isotope	Natural Abundance (%)	Reaction	Q value (keV)[a]
Si^{28}	92.21	*$Si^{28}(n, \alpha)Mg^{25}$	-2652.6 ± 3.2
		*$Si^{28}(n, p)Al^{28}$	-3852.1 ± 4.2
Si^{29}	4.70	*$Si^{29}(n, \alpha)Mg^{26}$	-32.7 ± 3.9
		$Si^{29}(n, p)Al^{29}$	-2893 ± 7
Si^{30}	3.09	$Si^{30}(n, \alpha)Mg^{27}$	-4201 ± 5
		$Si^{30}(n, p)Al^{30}$	-6510 ± 250

* See page 26.

a) Q values taken from Mattauch et al. (1965).

Table 3

Resonances in $Si^{28}(n, \alpha_o)Mg^{25}$ below 11.3 MeV

All table entries are in MeV and have a standard deviation of 13 keV. Mainsbridge et al. (1963) investigated this same reaction for neutron energies up to 8.5 MeV (see page 36) but with poorer energy resolution. They identified resonances at 7.300 ± 0.025 MeV, 7.66 ± 0.02 MeV and 7.94 ± 0.02 MeV.

7.285	8.380	9.840
7.430	8.510	10.000
7.510	8.670	10.150
7.635	8.800	10.460
7.780	8.930	10.650
7.890	9.050	10.780
8.000	9.290	10.990
8.120	9.410	11.230
8.240	9.550	

Table 4

Results of (He^3, n) Measurements [†]

Final Nucleus	Our (He^3, n) Q value (keV)	Mass Excess (keV)[a] This Experiment	Other Work	Best Value	Excited States (keV) This Experiment	Other Work
Si^{26}	85 ± 18	- 7158 ± 18	- 7153 ± 80[b] - 7131 ± 13[c]	- 7141 ± 11	1787 ± 27 2803 ± 28	1780 ± 60[b] 2790 ± 80[b]
S^{30}	- 573 ± 15	-14057 ± 15	-14270 ± 150[d] -14190 ± 150[e] -14090 ± 27[c]	-14065 ± 13	2190 ± 40	-
Ar^{34}	- 759 ± 15	-18394 ± 15	-	-18394 ± 15	2058 ± 35	-
Ti^{42}	-2865 ± 6	-25123 ± 7	-25090 ± 600[f, g]	-25123 ± 7	-	-
Cr^{48}	5550 ± 18	-42813 ± 19	-43023 ± 200[h, j] -42743 ± 200[i, j]	-42813 ± 19	(720 ± 30)* (2370 ± 50)*	-
Ni^{56}	4513 ± 14	-53899 ± 15	-53902 ± 18[k]	-53900 ± 12	2686 ± 24 3950 ± 25 (4980 ± 50)*	2710 ± 50[k] 3940 ± 50[k] 4970 ± 50[k]

Table 4 Cont'd.

					(5350 ± 50)*	5350 ± 50[k]
					6600 ± 30	6620 ± 50[k]
Zn^{60}	818 ± 18	-54186 ± 19	-	-54186 ± 19	1019 ± 25	-

* Assignment uncertain

a) $C^{12} = 0$. All numbers calculated from the experimentally measured quantities using the mass table of Mattauch, Thiele and Wapstra (1965).

b) Ajzenberg-Selove and Dunning (1960).

c) Frick et al. (1963).

d) Johnson, Chase and Imhof (1960).

e) Robinson, Rhode and Johnson (1961).

f) Oberholtzer (1962).

g) The mass excess quoted for Ti^{42} in Mattauch et al. is of unknown origin and probably erroneous according to Wapstra (1965).

h) Lieshout et al. (1955).

i) Sheline and Wilkinson (1955).

j) Mass estimate based on beta decay systematics.

k) Hoot, Kondo and Rickey (1965).

† See Chapter V.

Table 5

The 0^{o} (He^{3}, n) Cross Section Measurements

The quantities E_b, θ and ϵ are, respectively, the bombarding energy (in MeV), the half angle subtended by the detector and the ratio of the bombarding energy in the center-of-mass system to the Coulomb barrier, estimated using $V_c = (Z_x Z_{He^3} e^2)/(R_x + R_{He^3})$. Values of R_x were taken from Hofstadter (1956); R_{He^3} was taken as 2.0×10^{-13} cm. The data used for determining these cross sections are displayed in figures 22 to 29. See page 52 for further discussion.

Final Nucleus	E_b	θ	ϵ	Ground-state cross section (mb/sr)	Excited state (MeV) [probable J^{π}]	Ratio of excited- to ground-state cross section
Si^{26}	11.60	15	1.75	4.3 ± 1.7	1.79 $[2^+]$ a)	0.22 ± 0.07
					2.80 $[2^+]$ a)	0.29 ± 0.12
S^{30}	11.60	14	1.60	3.7 ± 1.1	2.19 $[2^+]$ a)	0.19 ± 0.05
Ar^{34}	10.81	16	1.32	1.4 ± 0.5	2.06 $[2^+]$ a)	0.10 ± 0.03
Ti^{42}	11.60	14	1.23	0.23 ± 0.09	-	-
Cr^{48}	11.00	17	1.09	0.15 ± 0.09	0.72	0.42 ± 0.23
					2.37	0.34 ± 0.15
Ni^{56}	11.51	18	0.99	0.12 ± 0.06	2.69 $[2^+]$ b)	1.32 ± 0.35
					3.95 $[0^+]$	1.02 ± 0.26
					5.35 $[0^+,2^+,4^+]$	0.36 ± 0.24
					6.60 $[2^+]$	2.50 ± 1.00
Zn^{60}	11.60	19	0.94	0.12 ± 0.04	1.02	1.45 ± 0.36

a) Spin and parity are those of the corresponding level in the charge-conjugated nucleus.

b) See discussion of Chapter VII, section 4 (page 78).

Table 6

Charge-Symmetry Predictions

Comparison of the measurements on Si^{26}, S^{30}, Ar^{34} and Ti^{42} with the predictions of charge symmetry. All numbers are in MeV.

Isobaric triplet	M(Z = A/2+1)-M(Z = A/2) Calculated[a]	Measured[b]	Excited states Z = A/2-1[c]	Z = A/2+1
Mg^{26} Al^{26} Si^{26}	4.88	5.051 ± 0.019	1.81, 2.94	1.79, 2.80
Si^{30} P^{30} S^{30}	6.02	6.140 ± 0.017	2.23, 3.51	2.19
S^{34} Cl^{34} Ar^{34}	5.88	6.057 ± 0.015	2.13, 3.30	2.06
Ca^{42} Sc^{42} Ti^{42}	6.76	7.018 ± 0.014	1.52, 1.84	-

a) Calculated using the mass table of Mattauch et al. (1965) and the formula on page 63. The locations of the first $\overline{T} = 1$ states in Al^{26}, P^{30} and Cl^{34} were obtained from Endt and Van der Leun (1962) and that of Sc^{42} from Oberholtzer (1962).

b) Calculated from our (He^3, n) Q value using the mass table of Mattauch et al.

c) Taken from Endt and Van der Leun.

Table 7

Beta-Decay Energy of Alpha Nuclei†

Nuclear pair	Mass difference (MeV)* Estimated[a)]	Measured
Zn^{60} - Cu^{60}	-	4.170 ± 0.022
Ni^{56} - Co^{56}	2.19 ± 0.05	2.115 ± 0.017
Cr^{48} - V^{48}[b)]	1.70 ± 0.10	1.657 ± 0.019

* These mass differences, particularly Ni^{56} - Co^{56}, are of interest in the e-process. See Chapter II.

a) Taken from Everling (1963b).

b) V^{48} mass taken from Mattauch et al. (1965).

† Based on the measurements of Chapters V and VI.

Table 8

Levels of V^{48} †
(energies in keV)

Nelson et al. [a]	Bjerregaard et al. [b]	Present work [c]
306 ± 14	310 ± 12	316 ± 15
416 ± 14	420 ± 12	408 ± 10
514 ± 14	523 ± 12	
	616 ± 12	615 ± 20
752 ± 14	751 ± 12	
	771 ± 12	
	1049 ± 12	

a) Nelson et al. (1960).

b) Bjerregaard, Dahl, Hansen and Sidenius (1964).

c) Computed using V^{48} mass from Mattauch et al. (1965).

† See page 70.

Table 9

Levels of Co^{56}
(energies in keV)

Ident.	Nelson et al. [a]	Anderson et al. [b]	Wells et al. [c]	Bjerregaard et al. [d]	Present work
B	159 ± 4	165 ± 15	164 ± 3	158 ± 12	166 ± 9
	186 ± 6				
	225 ± 6				
	280 ± 6				
D		560 ± 15		578 ± 12	576 ± 9
F		825 ± 15		829 ± 12	832 ± 9
G		980 ± 15	984 ± 4	965 ± 12	978 ± 9
				1008 ± 12	
H		1105 ± 15		1111 ± 12	1111 ± 9
I					1246 ± 13
J					1335(?) ± 13
K			1470 ± 6	1445 ± 12	1445 ± 13
L					1592 ± 18
M			1740 ± 5	1714 ± 12	1723 ± 13
N				1925 ± 12	1934 ± 13
O				2056 ± 12	2087 ± 13
P				2222 ± 12	2225 ± 18
Q				2291 ± 12	2312 ± 18
R				2358 ± 12	2381 ± 18

a) Nelson, Plendl and Davis (1962).

b) Anderson, Wong and McClure (1962).

c) Wells, Blatt and Meyerhof (1963). The similar experiment of Ohnuma and Hashimoto (1965) gives results in agreement with these.

d) Bjerregaard, Dahl, Hansen and Sidenius (1964).

Table 10

Levels of Cu^{60} *
(energies in keV)

B	72 ± 7	I	940 ± 9	S	2762 ± 13
C	298 ± 7	K	1428 ± 9	T	3000 ± 9
D	375 ± 7	L	1673 ± 9	U	3078 ± 13
E	465 ± 7	M	1783 ± 9	V	3157 ± 9
F	568 ± 9	N	1917 ± 25	W	3361 ± 25
F'	606 ± 9	O	2007 ± 9	X	3477 ± 9
G	681 ± 7	P	2196 ± 9	Y	3602 ± 9
H	796 ± 7	R	2547 ± 9		

* See page 70 and figure 32.

Table 11

The (He^3, p) Q Values*
(energies in keV)

Reaction	Previous Measurements[a)]	This work
$Fe^{54}(He^3, p)Co^{56}$	7427.8 ± 8.5	7410 ± 10
$Ni^{58}(He^3, p)Cu^{60}$	5760.3 ± 9.5	5770 ± 12

a) Calculated from mass table of Mattauch et al. (1965).

* See Chapter VI.

Table 12

Decay of Cl^{34m}

The relative intensities of S^{34} γ rays in the β^+ decay of Cl^{34m} are listed. The 2.13-MeV transition was arbitrarily assigned an intensity of 100. See page 75.

Transition in S^{34} (energies in MeV)	Relative intensity	
	Tohei[a]	Present work
3.92 → 3.30	weak	< 0.5[b]
4.07 → 3.30	weak	< 0.5[b]
3.30 → 2.13	32	47 ± 8
2.13 → 0	100	100 ± 5
3.30 → 0	32	34 ± 5
4.11 → 0	1	1.2 ± 0.5

a) Tohei (1960).

b) Not seen.

Figure 1

Neutron and gamma-ray spectrum from the reaction $Be^{9}(\alpha, n)C^{12}$ at a bombarding energy of 6.00 MeV as seen in a stilbene crystal located at 0^{o}. Neutron groups leading to the first three states of C^{12} and the 4.43-MeV gamma ray of C^{12} are visible. The neutron energies are 11.52, 6.84 and 3.25 MeV. See pages 15-16.

The absolute cross section for the n_o group was found from this spectrum in the following way. The sum, N_1, (equal to 3430 ± 150) of all counts above channel 105, which corresponds to a proton energy, E_c, of 10.23 ± 0.03 MeV, was obtained. The total number of n_o neutrons detected in the crystal is then

$$N_2 = N_1 E_n/(E_n - E_c) = (3.07 \pm 0.15) \times 10^4 .$$

The target was measured to have $(5.90 \pm 0.94) \times 10^{18}$ beryllium atoms/cm^2 (see text, page 50). Therefore the number of neutrons detected per incident α particle per target atom is

$$N_3 = N_2/(Q/2e \times 5.90 \times 10^{18}) = 1.11 \pm 0.19 \times 10^{18}\ cm^{+2}$$

From the graph of figure 2, $4\pi\epsilon = 0.0256 \pm 0.0015$. Therefore the differential cross section is

$$d\sigma/d\Omega(0^{o}) = N_3/4\pi\epsilon = 4.36 \pm 0.74 \text{ mb/sr} .$$

The final value for the cross section at this point was obtained by averaging the value from this spectrum and another spectrum obtained with a thinner target ($2.68 \pm 0.54 \times 10^{18}$ atom/cm^2). It is 4.88 ± 0.98 mb/sr (see figure 3) and includes 15% error to allow for the effects of multiple scatter and edge losses.

Figure 1

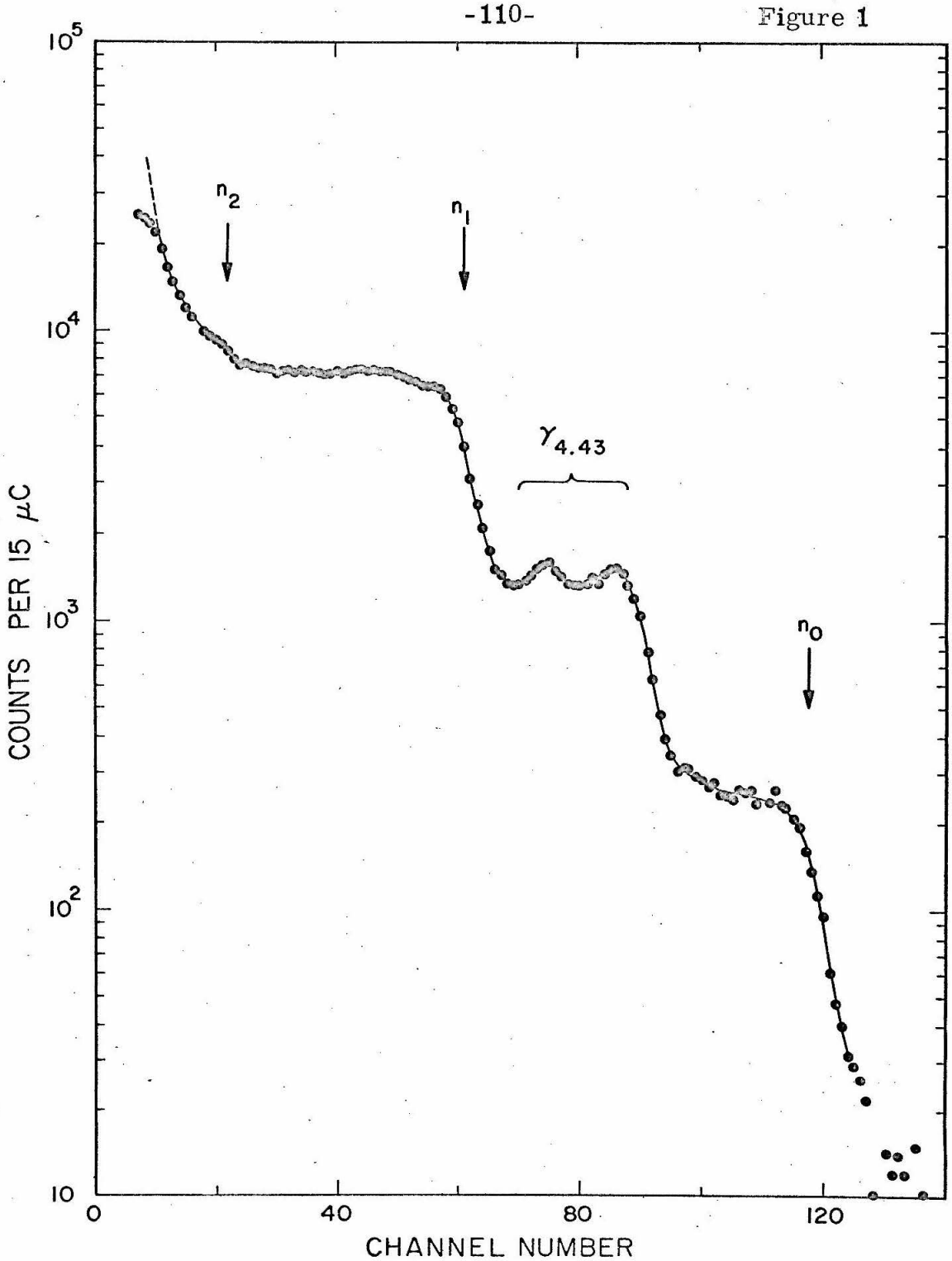
10^5
10^4
10^3
10^2
10
COUNTS PER 15 μC
n_2
n_1
$\gamma_{4.43}$
n_0
0
40
80
120
CHANNEL NUMBER

Figure 2

Single-scatter detection efficiency vs neutron energy for the stilbene crystal used for the $Be^{9}(\alpha, n)C^{12}$ neutron yield measurements of Chapter III. The dimensions of the crystal and the geometry used are given in the figure. The quantity ϵ is that fraction of the total number of neutrons emitted by an isotropic neutron source that is removed from the primary beam by scattering from hydrogen. The solid curve, which was used in our analysis, allows for attenuation of the primary beam by scattering from carbon (which does not produce an observable pulse) as well as from hydrogen; the dashed curve was calculated assuming hydrogen scatter only and is about 10% higher. See text (page 19) for a discussion of the possible usefulness of this curve. The form of the efficiency integrals for the two curves is given on the figure; $n_H\sigma_H$ and $n_C\sigma_C$ are the linear attenuation coefficients for scattering from hydrogen and carbon respectively, and x is the path length of the neutron beam in the crystal. Values of $n_H\sigma_H$ and $n_C\sigma_C$ were taken from table I of Swartz and Owen (1960). The figure displays $4\pi\epsilon$ for convenience in finding differential cross sections in cm^2-steradians^{-1}.

Figure 2

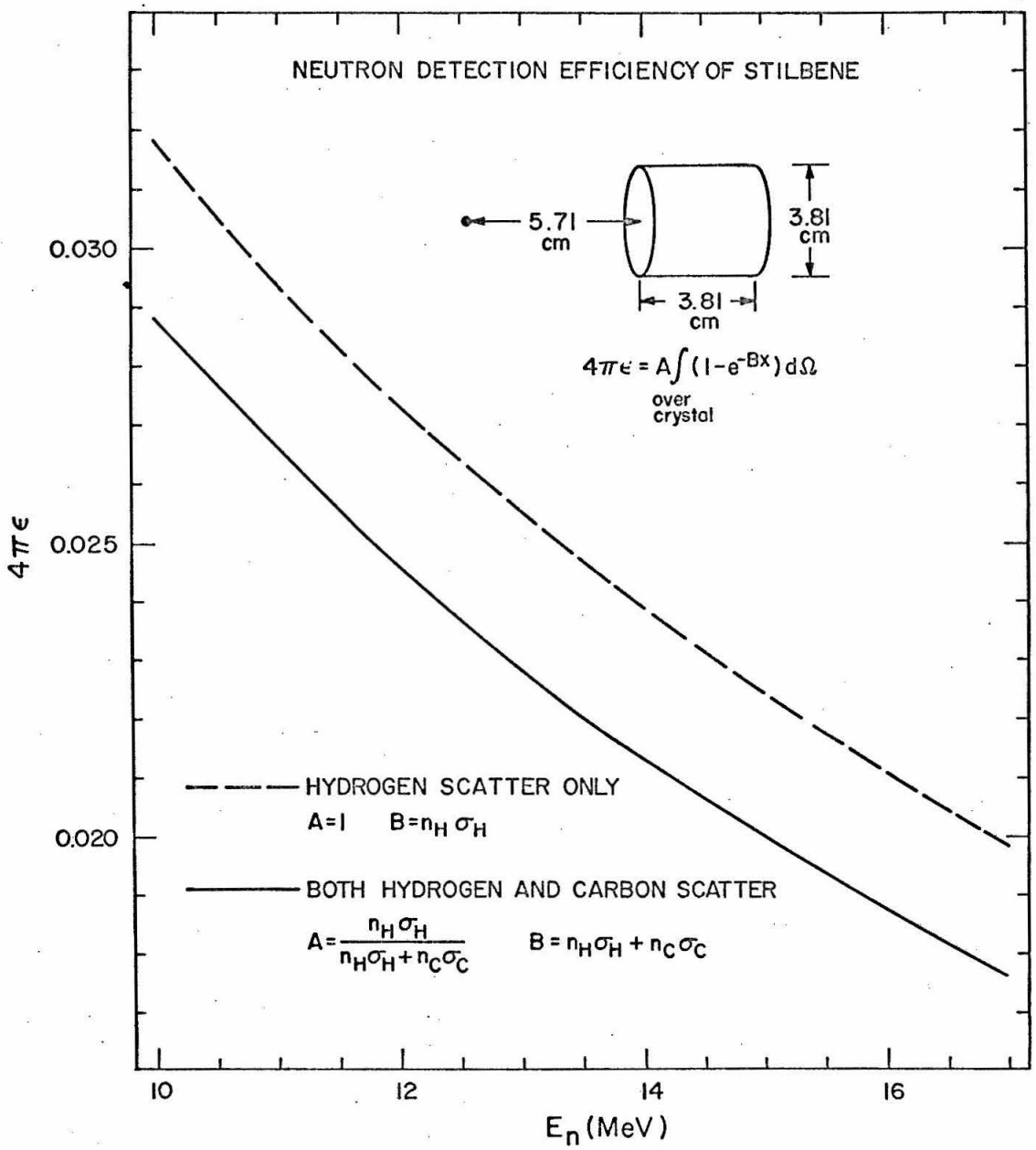
NEUTRON DETECTION EFFICIENCY OF STILBENE
5.71 cm
3.81 cm
3.81 cm
$4\pi\epsilon = A\int_{\text{over crystal}}(1-e^{-Bx})\,d\Omega$
0.030
0.025
0.020
$4\pi\epsilon$
HYDROGEN SCATTER ONLY
A=1 $B=n_H\sigma_H$
BOTH HYDROGEN AND CARBON SCATTER
$A=\frac{n_H\sigma_H}{n_H\sigma_H+n_C\sigma_C}$ $B=n_H\sigma_H+n_C\sigma_C$
10
12
14
16
E_n (MeV)

Figure 3

Cross section at 0^{o} for the reaction $Be^{9}(\alpha, n_{o})C^{12}$ as a function of bombarding energy. The resonances, indicated by arrows, may correspond to levels in the compound nucleus C^{13}. See page 21 and table 1. The standard deviation on the absolute value of the cross section is 20%; the statistical error on each point is 2% or less for the points above 5.5 MeV.

Figure 3

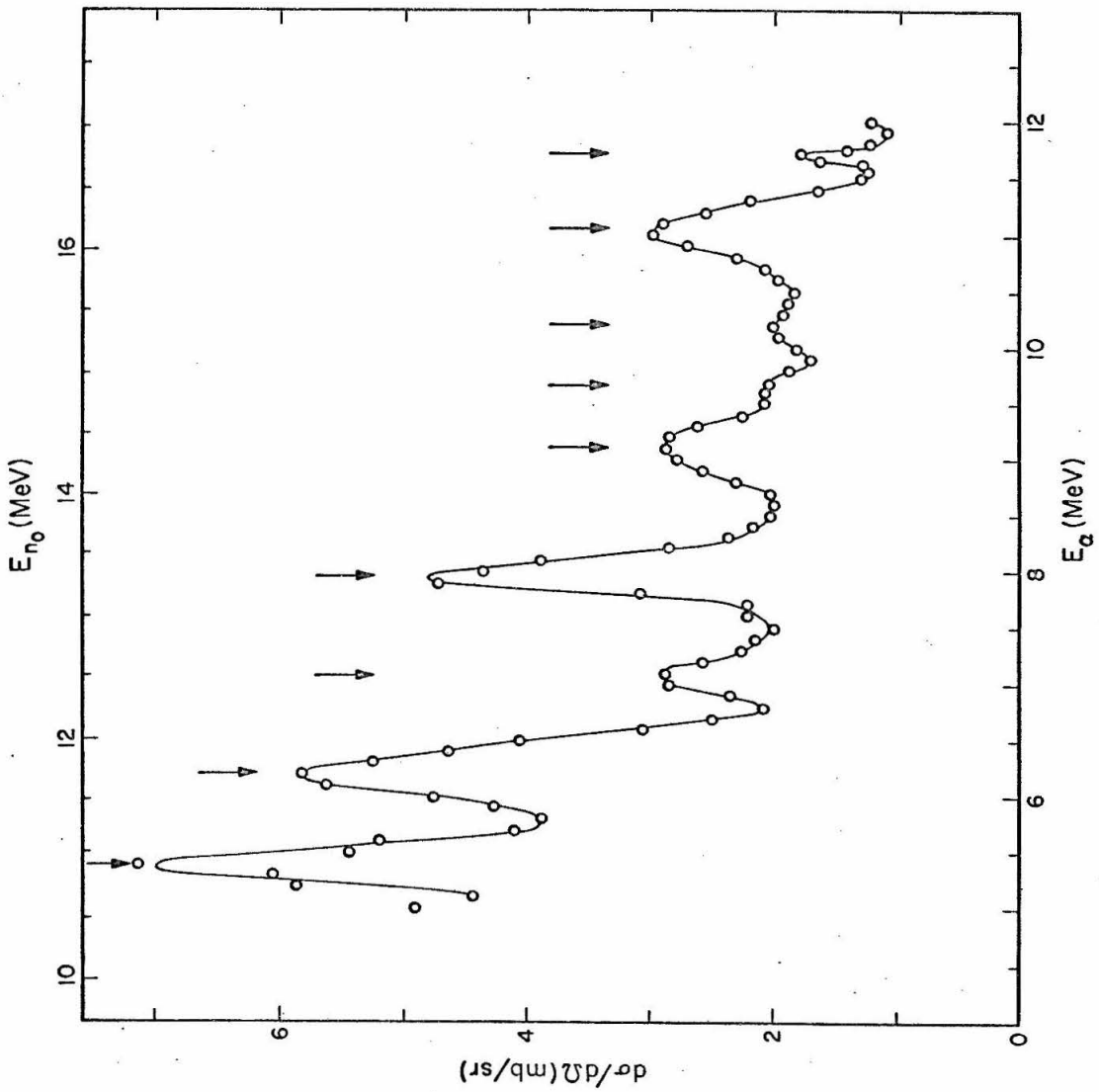

Figure 4

Cross sections at 0^{o} for the reactions $Be^{9}(\alpha, n_1)C^{12}$ and $Be^{9}(\alpha, n_2)C^{12}$ as a function of bombarding energy. The arrows indicate the position of resonances seen in the ground-state neutron yield (see figure 3). See pages 21 and 22.

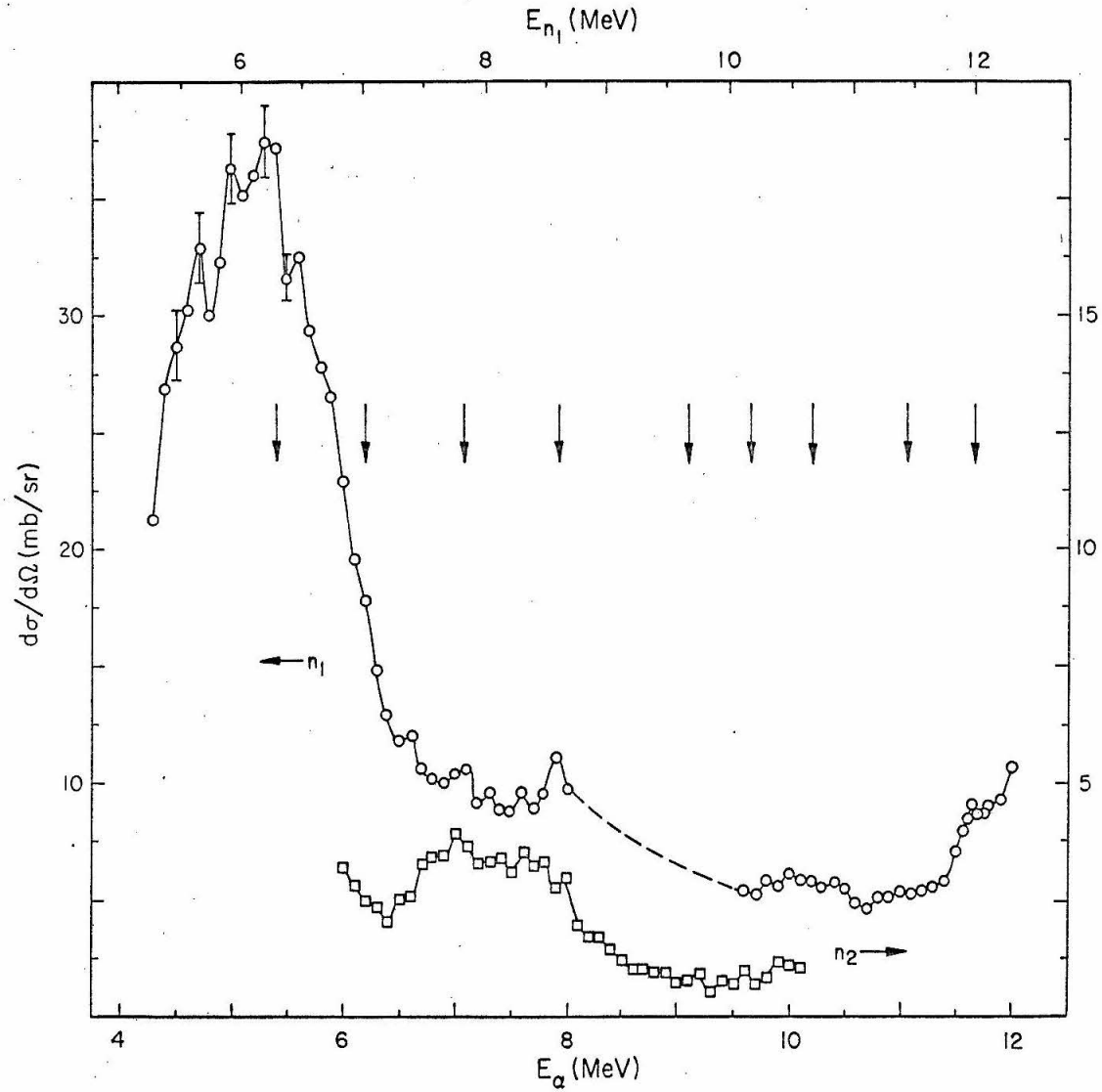
E_{n_1} (MeV)
6
8
10
12
30
20
10
15
10
5
$d\sigma/d\Omega$ (mb/sr)
n_1
n_2
4
6
8
10
12
E_α (MeV)

Figure 4

Figure 5

Upper portion of the pulse-height spectrum resulting from neutron-induced reactions in a silicon semiconductor detector. The peaks observed are identified with the different states of the final nuclei produced. See pages 38-39 for the meaning of ΔE. The incident neutrons, produced in the reaction $Be^{9}(\alpha, n)C^{12}$, had an energy of 9.83 MeV.

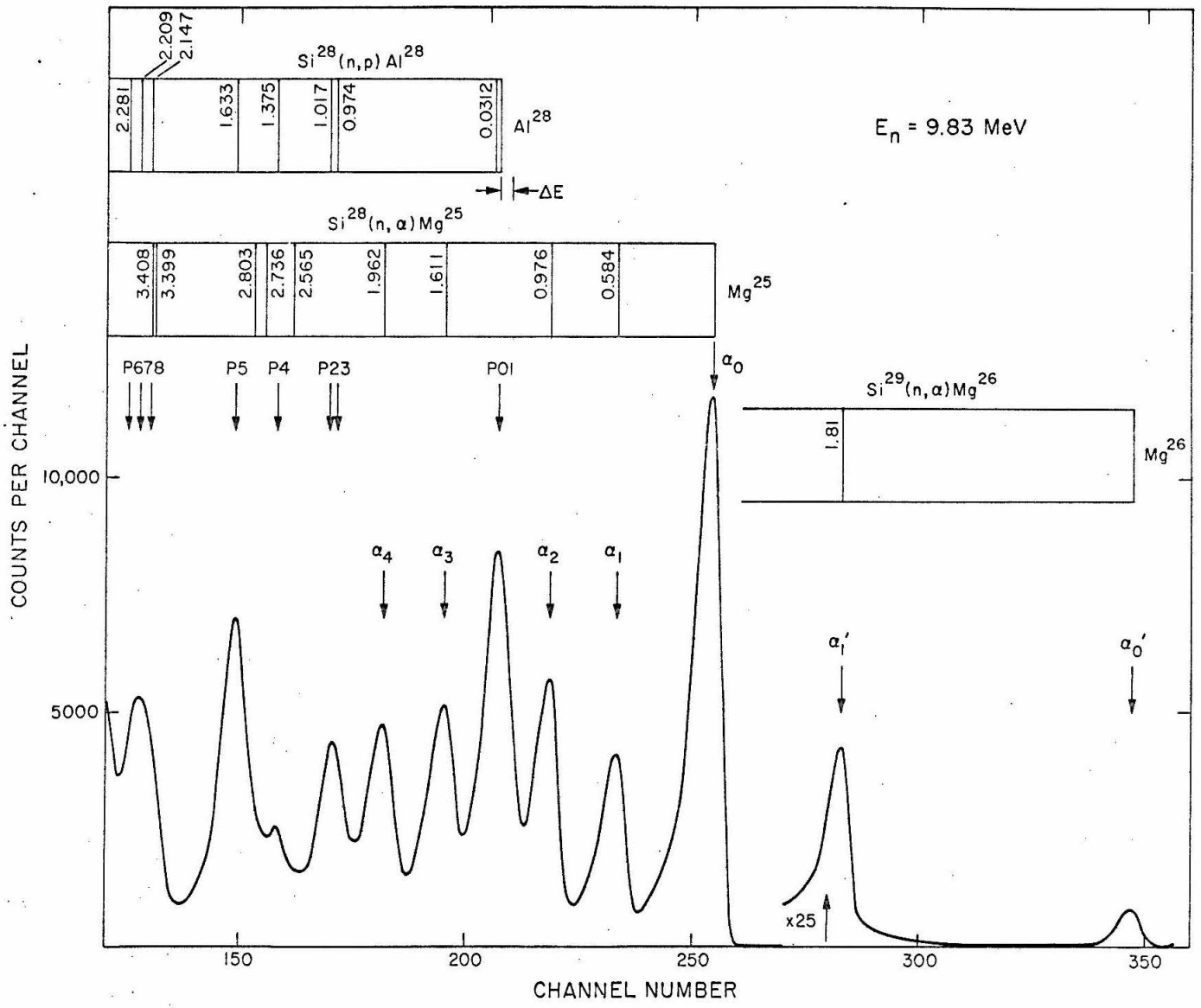
2.209
2.147
Si28(n,p) Al28
2.281
1.633
1.375
1.017
0.974
0.0312
Al28
ΔE
Si28(n,α) Mg25
3.408
3.399
2.803
2.736
2.565
1.962
1.611
0.976
0.584
Mg25
En = 9.83 MeV
P678
P5
P4
P23
P01
α0
Si29(n,α) Mg26
1.81
Mg26
α4
α3
α2
α1
α1'
α0'
x25
COUNTS PER CHANNEL
10,000
5000
150
200
250
300
350
CHANNEL NUMBER

Figure 5

Figure 6

Spectrum produced by a Cs^{137} gamma-ray source (E_γ = 0.662 MeV) in a chilled lithium-drifted semiconductor detector. The most prominent feature is the Compton shoulder whose edge appears at E_e = 0.468 MeV. Also visible are a small full-energy peak (Γ = 20 keV) and a secondary Compton edge at E_e = 0.468 + 0.074 = 0.542 MeV. Using the known Compton scattering cross section, and the theoretical shape of the Compton profile (dashed curve), the active volume of the detector was deduced to be 0.271 $\pm$ 0.035 cm^3. The detector area was 80 mm^2; therefore the depth was 3.39 $\pm$ 0.44 mm. This detector was the one used for the $D(d,n)He^3$ measurements of the Si^{28} + n yield curve. See pages 28 and 81.

Figure 6

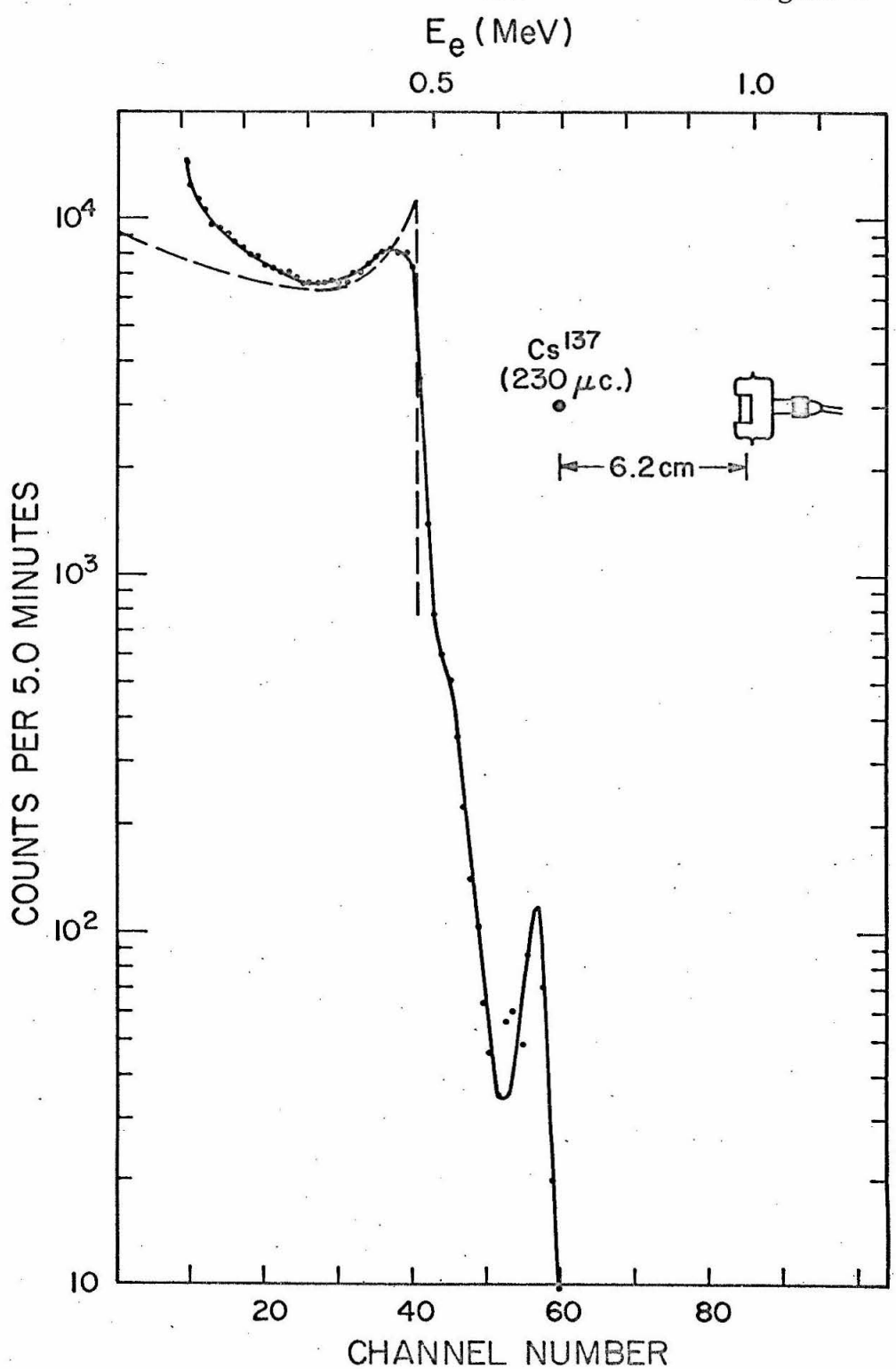
E_e (MeV)
0.5
1.0
10^4
10^3
10^2
10
COUNTS PER 5.0 MINUTES
Cs^{137}
(230 μc.)
6.2cm
20
40
60
80
CHANNEL NUMBER

Figure 7

Mounting arrangement used for the Li-drifted semiconductor detector. A-detector; B-stainless steel front (0.015" thick); C-stainless steel tubing (0.010" wall thickness); D-copper bar; E-clamping bar; F-vacuum electrical feed-through. Cross hatched material is brass. See page 29.

Figure 7

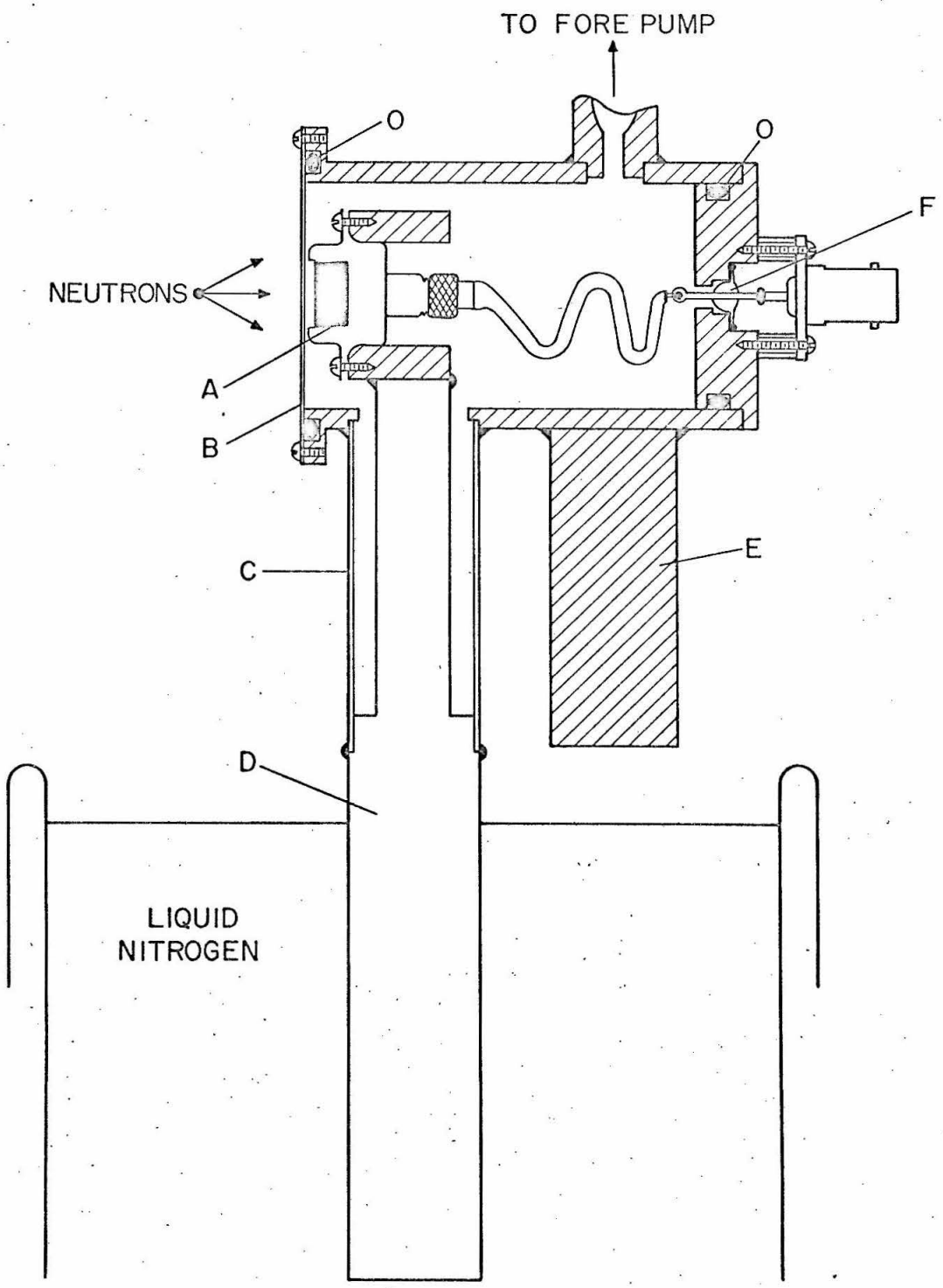

Figure 8

Two useful geometries for using a semiconductor detector as a neutron spectrometer:

a) Head-on (see page 31),

b) Side-on (see page 33).

The cylinder represents the active volume of the detector.

Figure 8

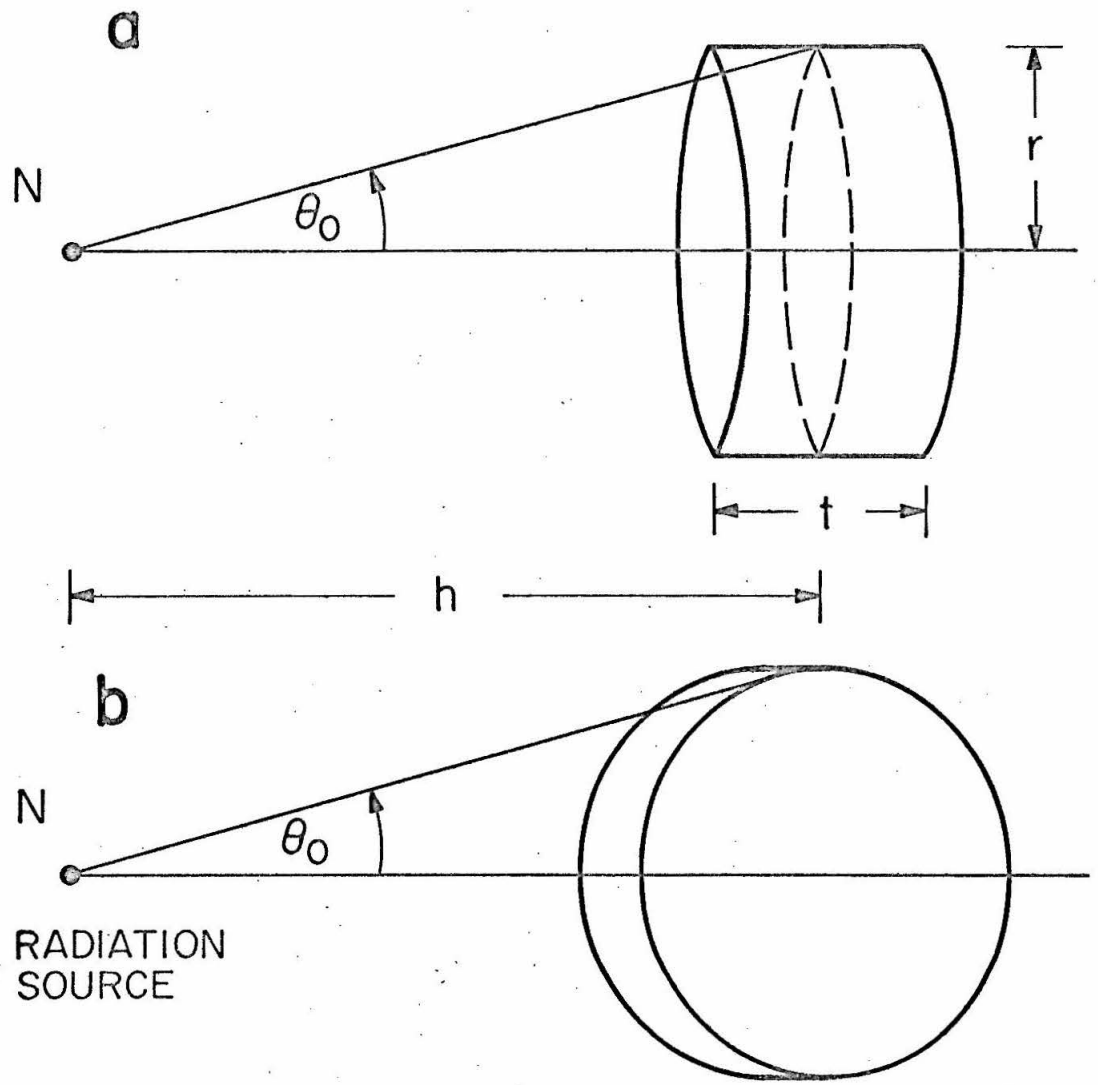

Figure 9

Spectrum produced in a silicon detector by neutrons from the reaction $D(d, n)He^3$ at a bombarding energy of 5.15 MeV. After correction for the gas cell entrance foil, deuterium gas target thickness and kinematic energy spread of the outgoing neutrons, the average neutron energy at the detector was 8.33 MeV. This is a typical spectrum from the data used to obtain the Si^{28} + n yield curves of figures 12 and 14. The regions summed for the different integral cross sections are indicated. A calculation of the α_o cross section obtained from this spectrum is given on page 82.

Low energy peaks due to $Si^{28}(n, n)Si^{28}$ and $Si^{28}(n, n')Si^{28*}$ (1.77) are identified. The arrows indicate the expected positions of the maximum energy Si^{28} recoil calculated from the position of the $Si^{28}(n, \alpha_o)$ peak. A correction of 17%, taken from the data of Sattler (1965), has been applied to allow for the pulse-height defect of the recoil silicon atoms. See page 41.

Figure 9

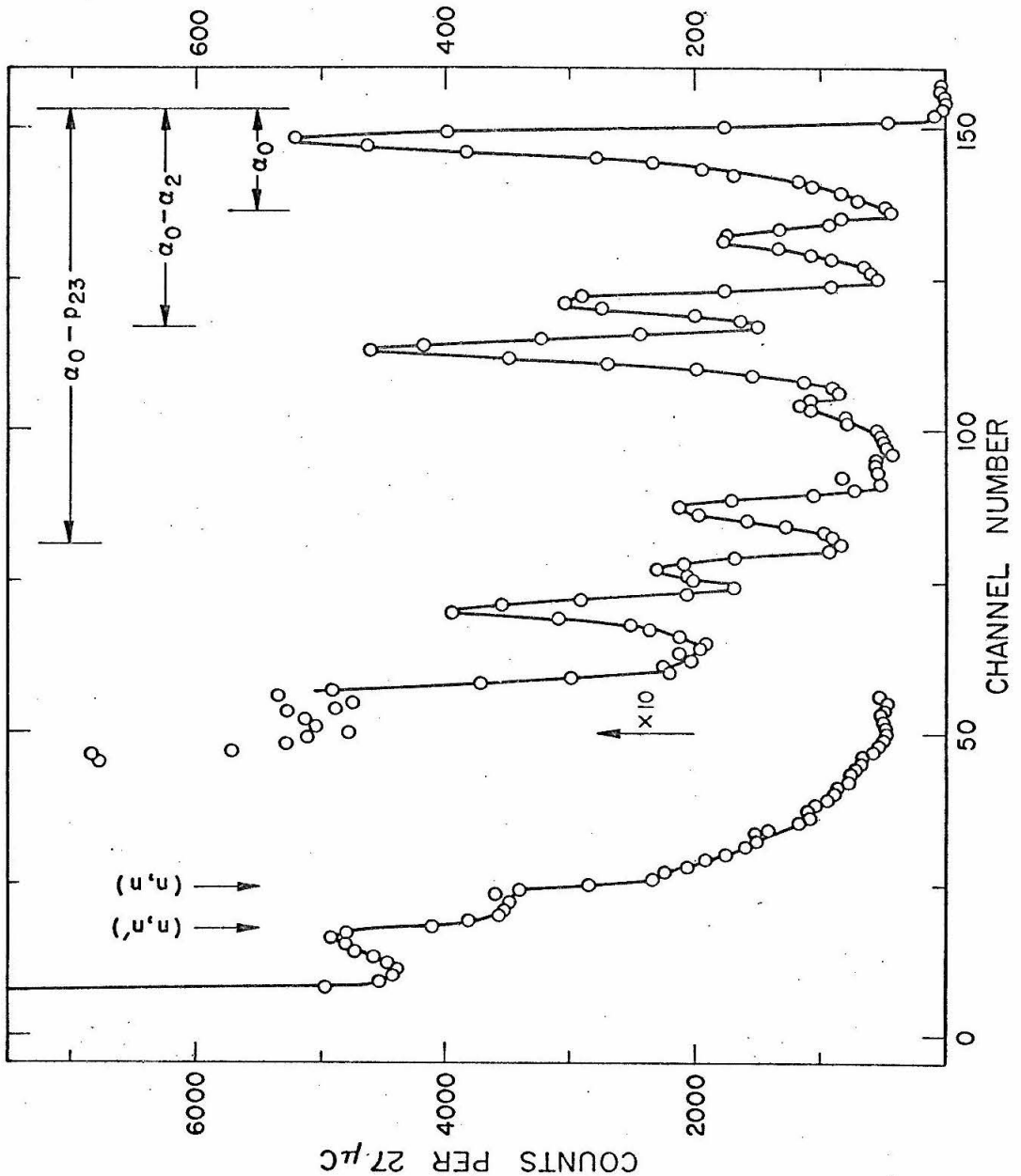
COUNTS PER 27 μC
6000
4000
2000
600
400
200
CHANNEL NUMBER
0
50
100
150
$a_0 - p_{23}$
$a_0 - a_2$
a_0
(n,n)
(n,n')
x10

Figure 10

Spectrum produced in a silicon detector by neutrons from the reaction $Be^{9}(\alpha, n)C^{12}$ at a bombarding energy of 8.00 MeV. After correction for the Be^{9} target thickness (5.90×10^{18} atoms/cm^2, equivalent to 49 keV) and kinematic energy spread of the outgoing neutrons, the average neutron energy at the detector was 13.29 MeV. This is a typical spectrum from the data used to obtain the Si^{28} + n yield curves of figures 13 and 15 to 18. The regions summed for the different integral cross sections are indicated. A calculation of the α_0 cross section obtained from this figure is given on page 83.

Figure 10

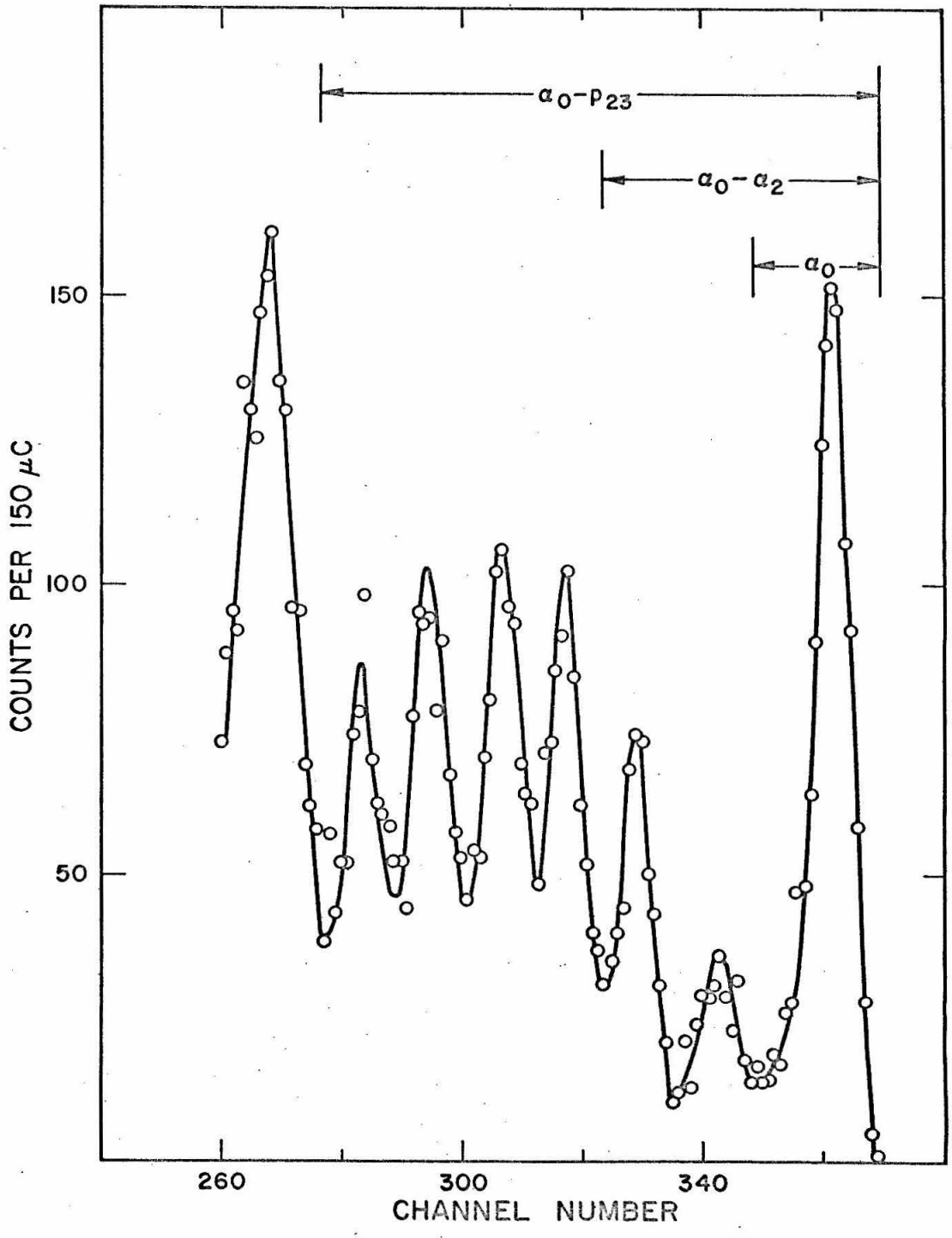
a_0-p_{23}
a_0-a_2
a_0
150
100
50
COUNTS PER 150 μC
260
300
340
CHANNEL NUMBER

Figure 11

Experimental set-ups used for the measurement of the Si^{28} + n yield curves (see figures 12-18).

Top: $D(d, n)He^{3}$ as neutron source.

Bottom: $Be^{9}(\alpha, n)$ as neutron source.

The data given on this figure, in conjunction with the spectra of figures 9 and 10 are used to calculate the absolute cross section for $Si^{28}(n, \alpha_{o})Mg^{25}$ in appendix 1 (page 81).

Figure 11

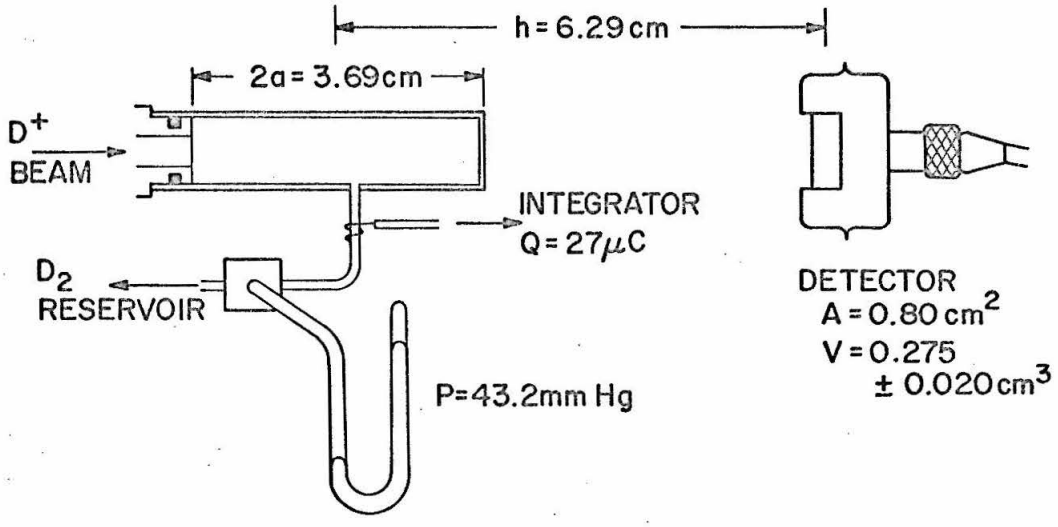
h = 6.29 cm
2a = 3.69 cm
D+
BEAM
INTEGRATOR
Q = 27μC
D2
RESERVOIR
P = 43.2 mm Hg
DETECTOR
A = 0.80 cm2
V = 0.275
± 0.020 cm3

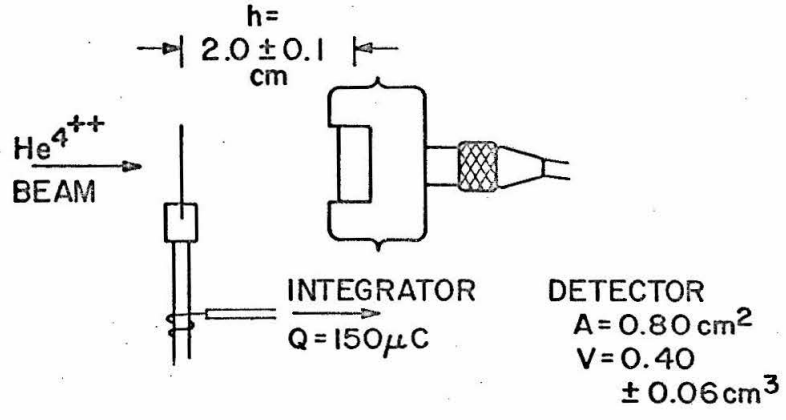
h =
2.0 ± 0.1
cm
He4++
BEAM
INTEGRATOR
Q = 150μC
DETECTOR
A = 0.80 cm2
V = 0.40
± 0.06 cm3

Figure 12

Total cross section for the reaction $Si^{28}(n, \alpha_o)Mg^{25}$ for $7.2 \leq E_n \leq 12.0$ MeV. Table 3 is a listing of the clearly-resolvable resonances on this curve. The reaction $D(d, n)He^3$ was used to provide neutrons and a Li-drifted silicon detector served as both target and detector. For details on how this curve was obtained and why it is useful, see Chapter IV, section 4 (starting on page 33).

Figure 12

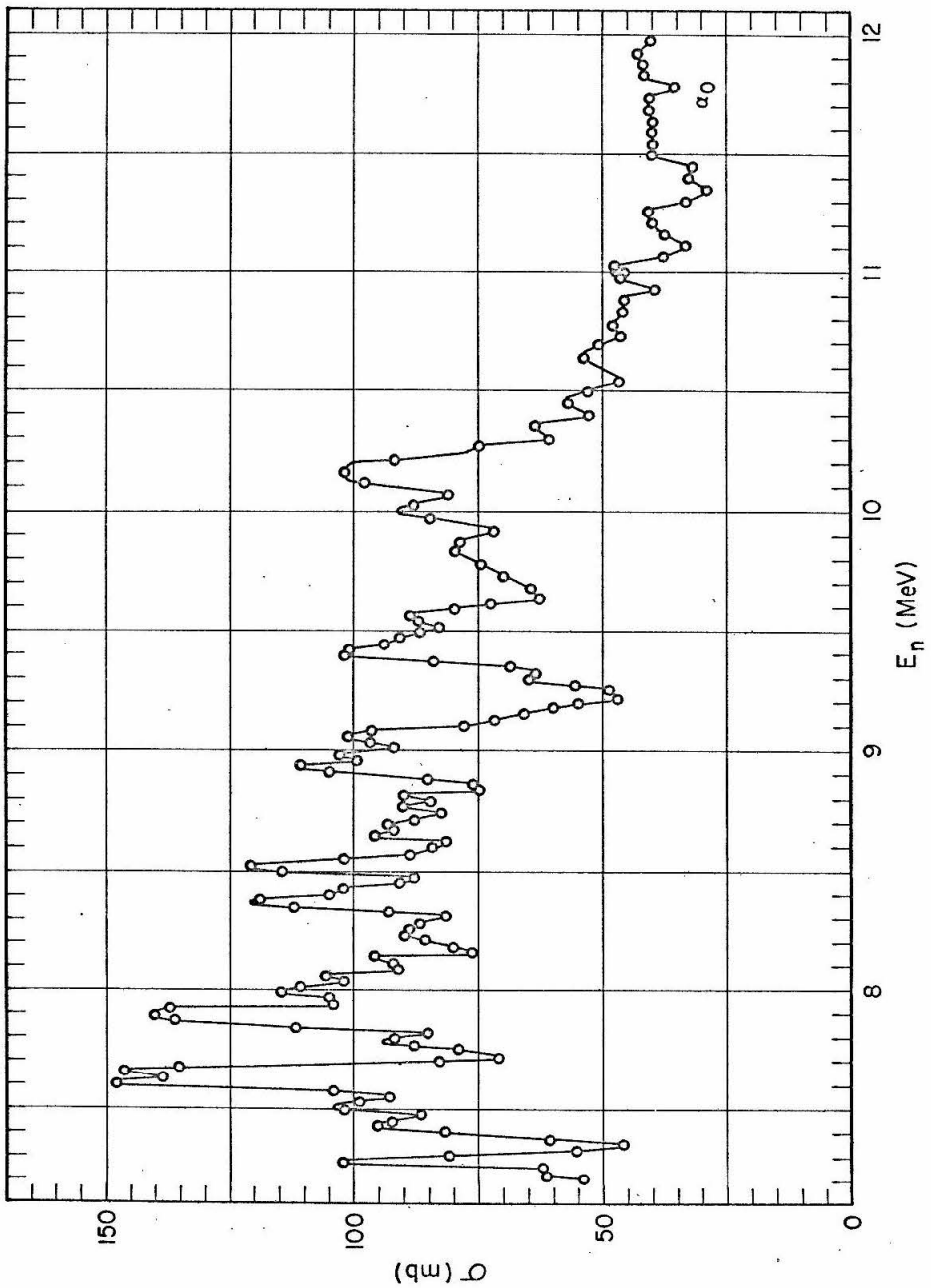

Figure 13

Total cross section for the reaction $Si^{28}(n, \alpha_o)Mg^{25}$ for $11.44 \leq E_n \leq 16.40$ MeV. The reaction $Be^{9}(\alpha, n_o)C^{12}$ was used to provide neutrons and a Li-drifted silicon detector served as both target and detector. For details on how this curve was obtained and why it is useful, see Chapter IV, section 4 (starting on page 33).

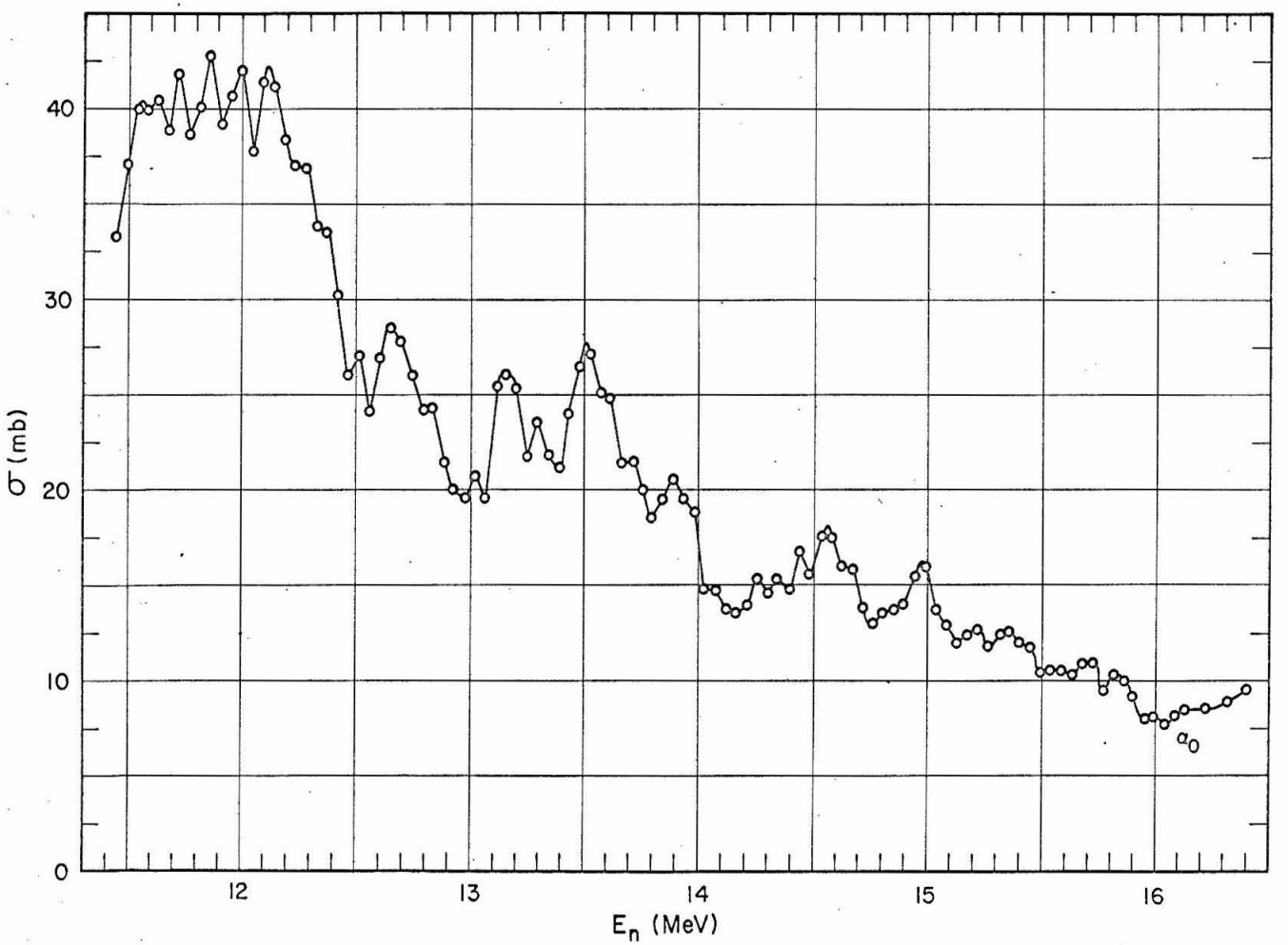

Figure 13

Figure 14

Total cross sections for peaks α_o-α_2 (lower curve) and α_o-p_{23} (upper curve) for the reactions $Si^{28}(n, \alpha) Mg^{25}$ and $Si^{28}(n, p)Al^{28}$ for neutron energies of 7.2 to 12.0 MeV. The reaction $D(d, n)He^3$ was used to provide neutrons and a Li-drifted silicon detector served as both target and detector. Figure 9 shows a typical spectrum from the data used to obtain these curves and indicates the regions summed for the different integral cross sections. The analysis, experimental techniques and possible applications of these curves are discussed in Chapter IV, section 4 (starting on page 33).

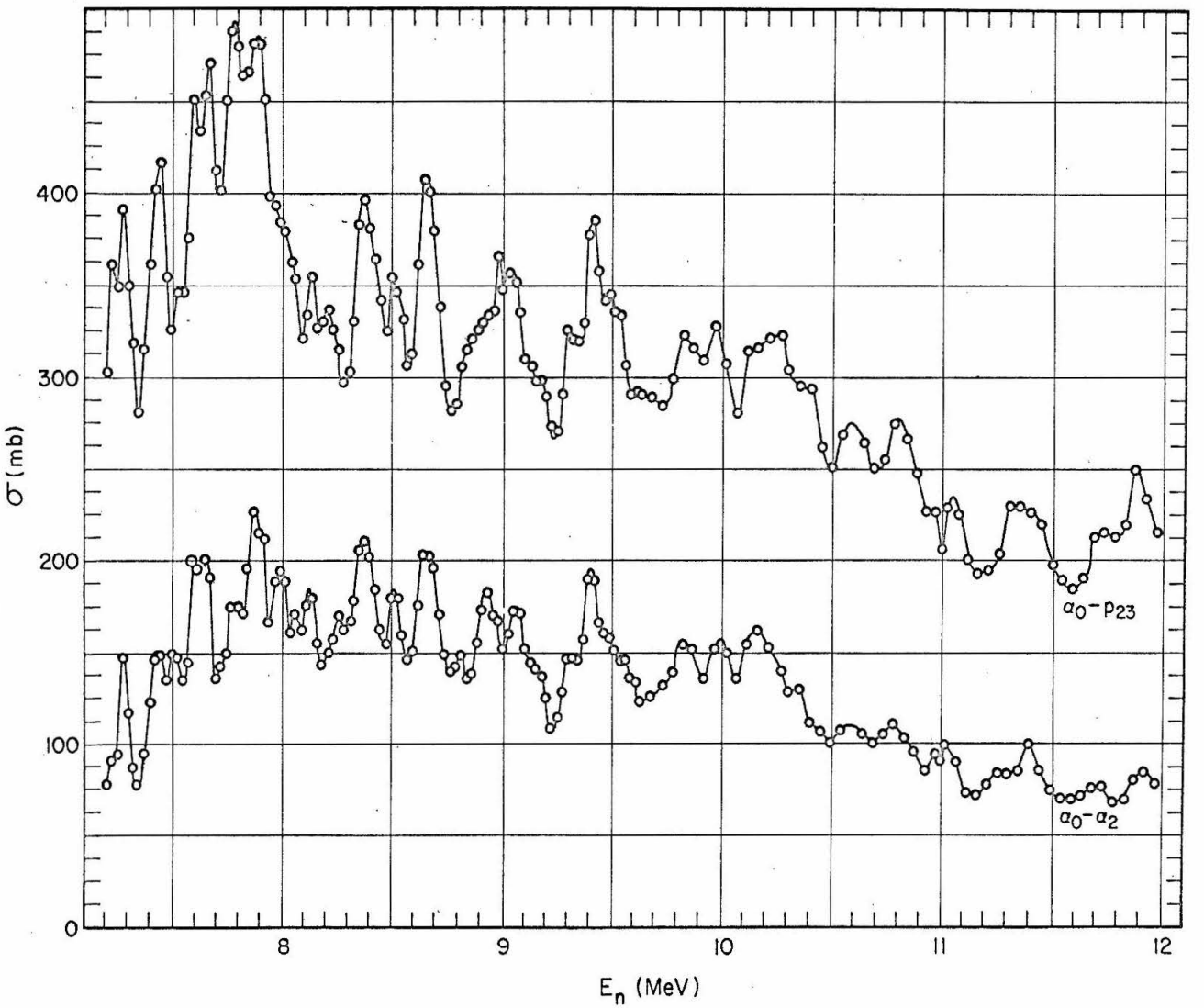

Figure 14

Figure 15

Total cross sections for peaks α_o-α_2 (lower curve) and α_o-p_{23} (upper curve) for the reactions $Si^{28}(n, \alpha)Mg^{25}$ and $Si^{28}(n, p)Al^{28}$ for neutron energies of 11.44 to 16.40 MeV. The reaction $Be^{9}(\alpha, n_o)C^{12}$ was used to provide neutrons and a Li-drift silicon detector served as both target and detector. Figure 10 shows a typical spectrum from the data used to obtain these curves and indicates the regions summed for the different integral cross sections. The analysis, experimental techniques and possible applications of these curves are discussed in Chapter IV, section 4 (starting on page 33).

Figure 15

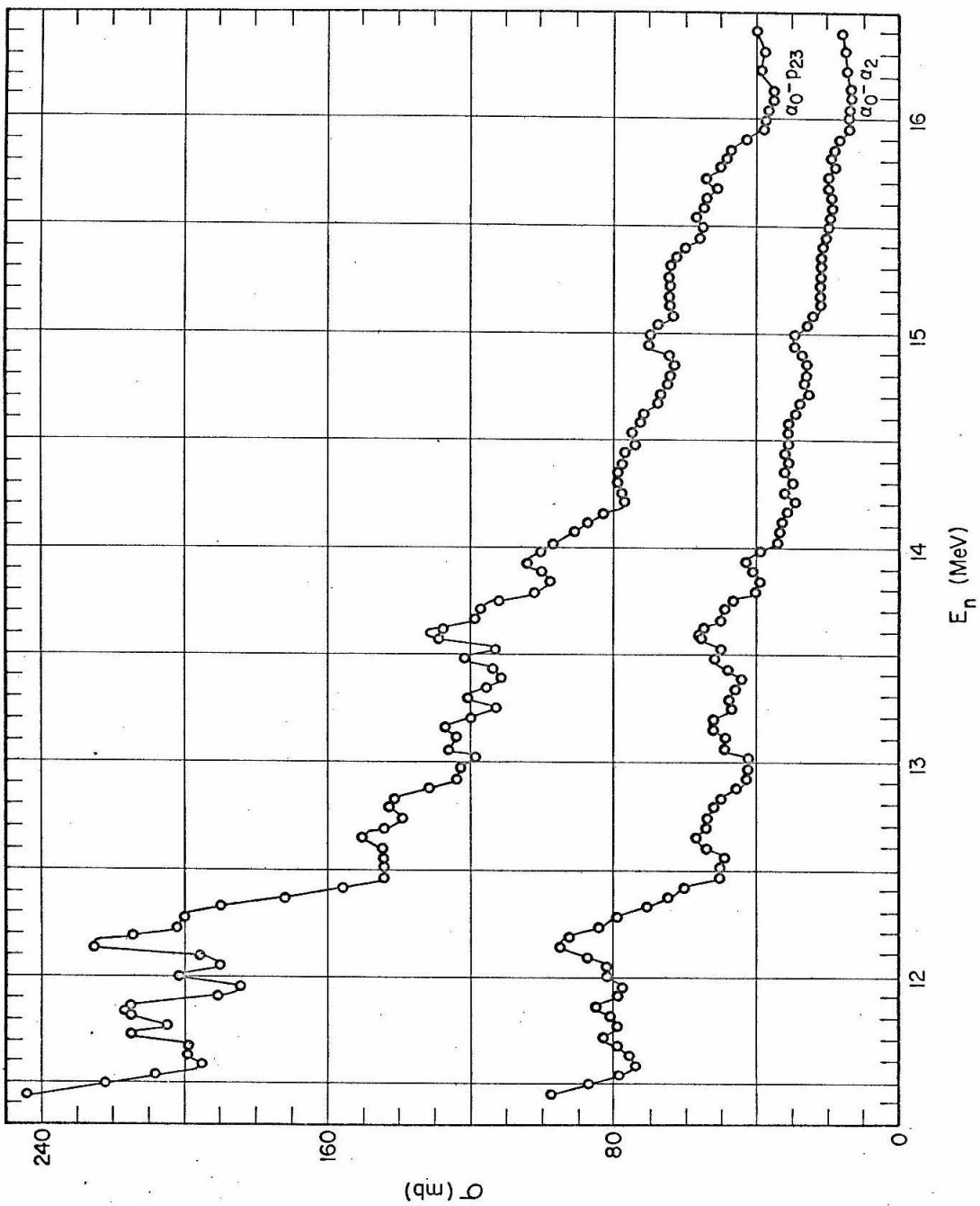

Figure 16

Total cross sections for peaks α_1 (lower curve) and α_3 (upper curve) for the reaction $Si^{28}(n, \alpha)Mg^{25}$ for neutron energies of 11.44 to 16.22 MeV. These curves were evaluated from the same data as the curves of figures 13 and 15. The reaction $Be^{9}(\alpha, n_o)C^{12}$ was used to provide neutrons and a Li-drifted silicon detector served as both target and detector. The analysis, experimental techniques and possible applications of these curves are discussed in Chapter IV, section 4 (starting on page 33).

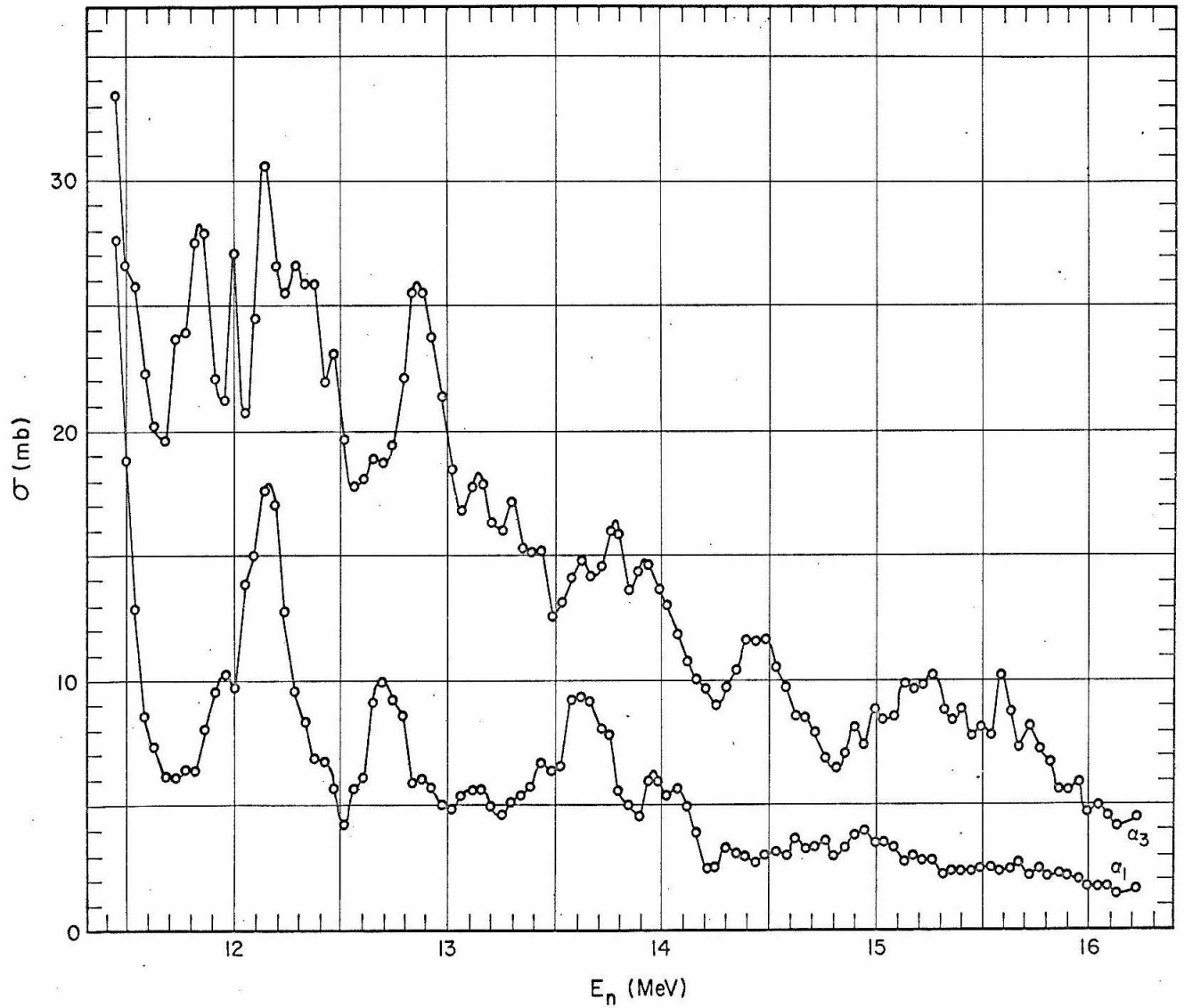

Figure 16

Figure 17

Total cross sections for peaks α_2 (lower curve) and α_4 (upper curve) for the reaction $Si^{28}(n, \alpha)Mg^{25}$ for neutron energies of 11.44 to 16.22 MeV. For details, see the caption of figure 16.

Figure 17

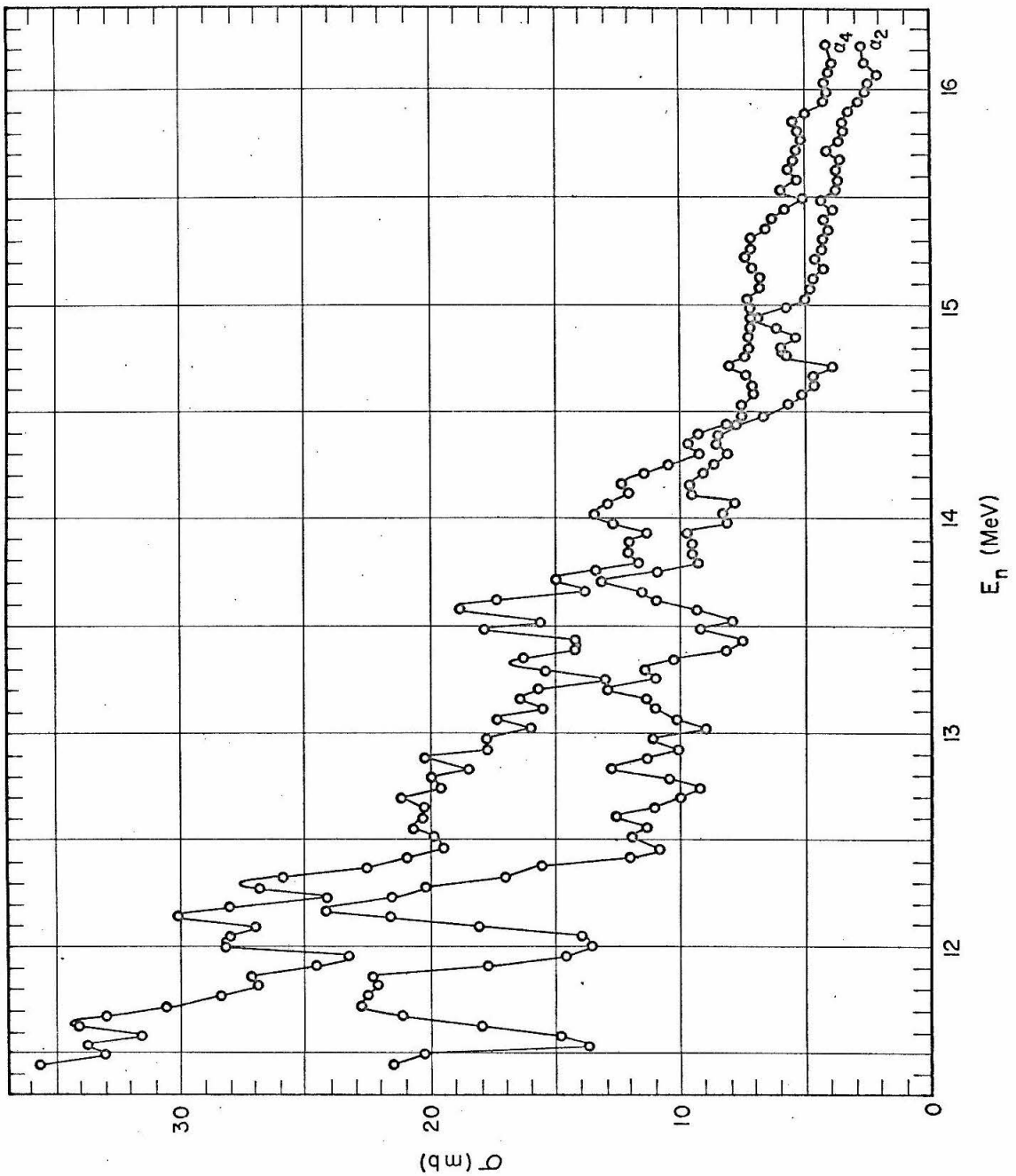

Figure 18

Total cross sections for peaks p_{01} (upper curve) and p_{23} (lower curve) for the reaction $Si^{28}(n, p)Al^{28}$ for neutron energies of 11.44 to 16.22 MeV. For details, see the caption of figure 16.

Figure 18

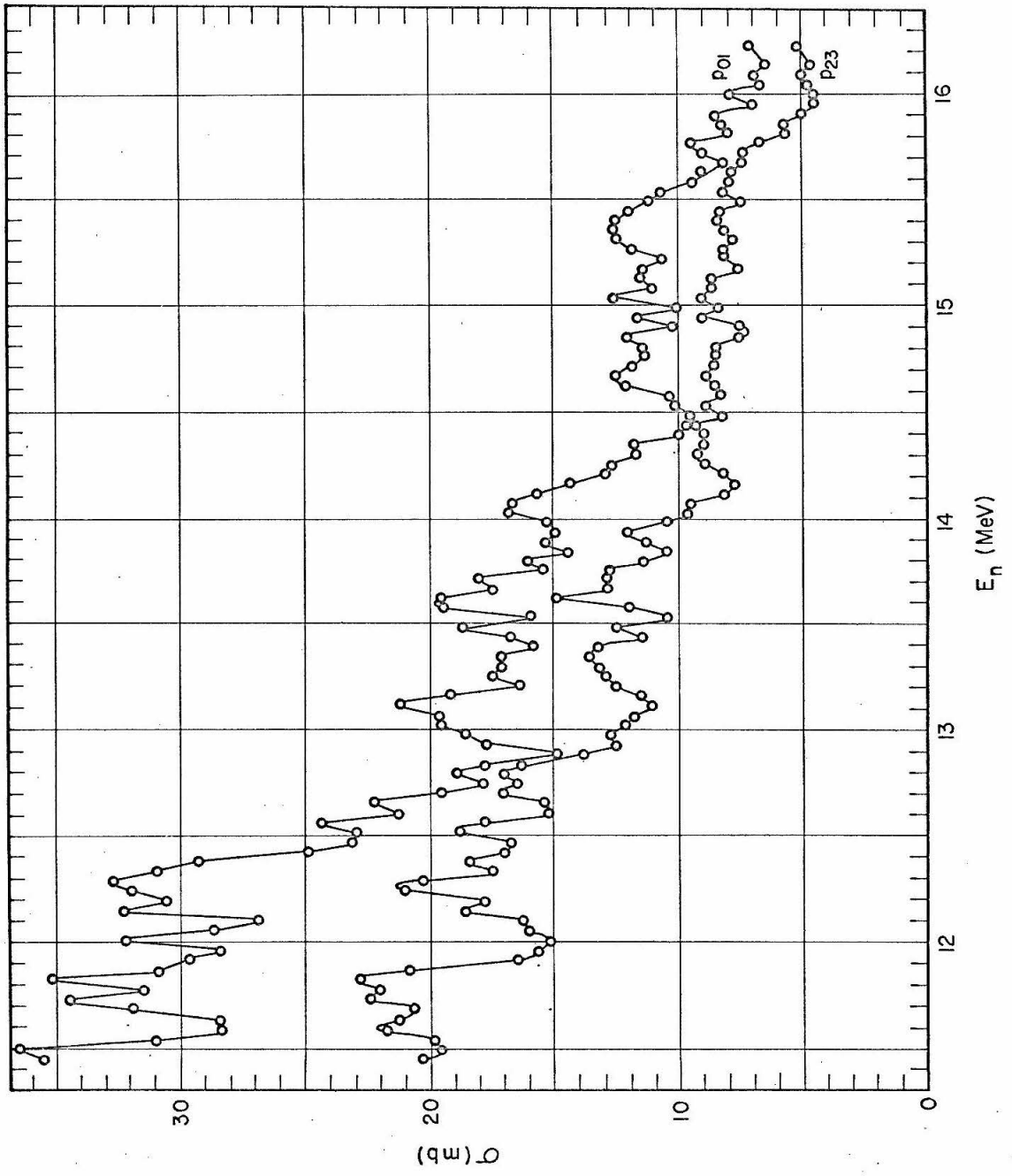

Figure 19

Cross section at 0^{o} for the reaction $Be^{9}(\alpha, n_{o})C^{12}$ as a function of bombarding energy. This curve was measured with a silicon semiconductor detector (see page 36). It agrees well, both in absolute cross section and shape, with the curve of figure 2 in the region of overlap (E_{α} = 5-6 MeV) and with the data of Risser, Price and Class (1957) who measured this cross section for $1.7 \leq E_{\alpha} \leq 4.8$ MeV.

Figure 19

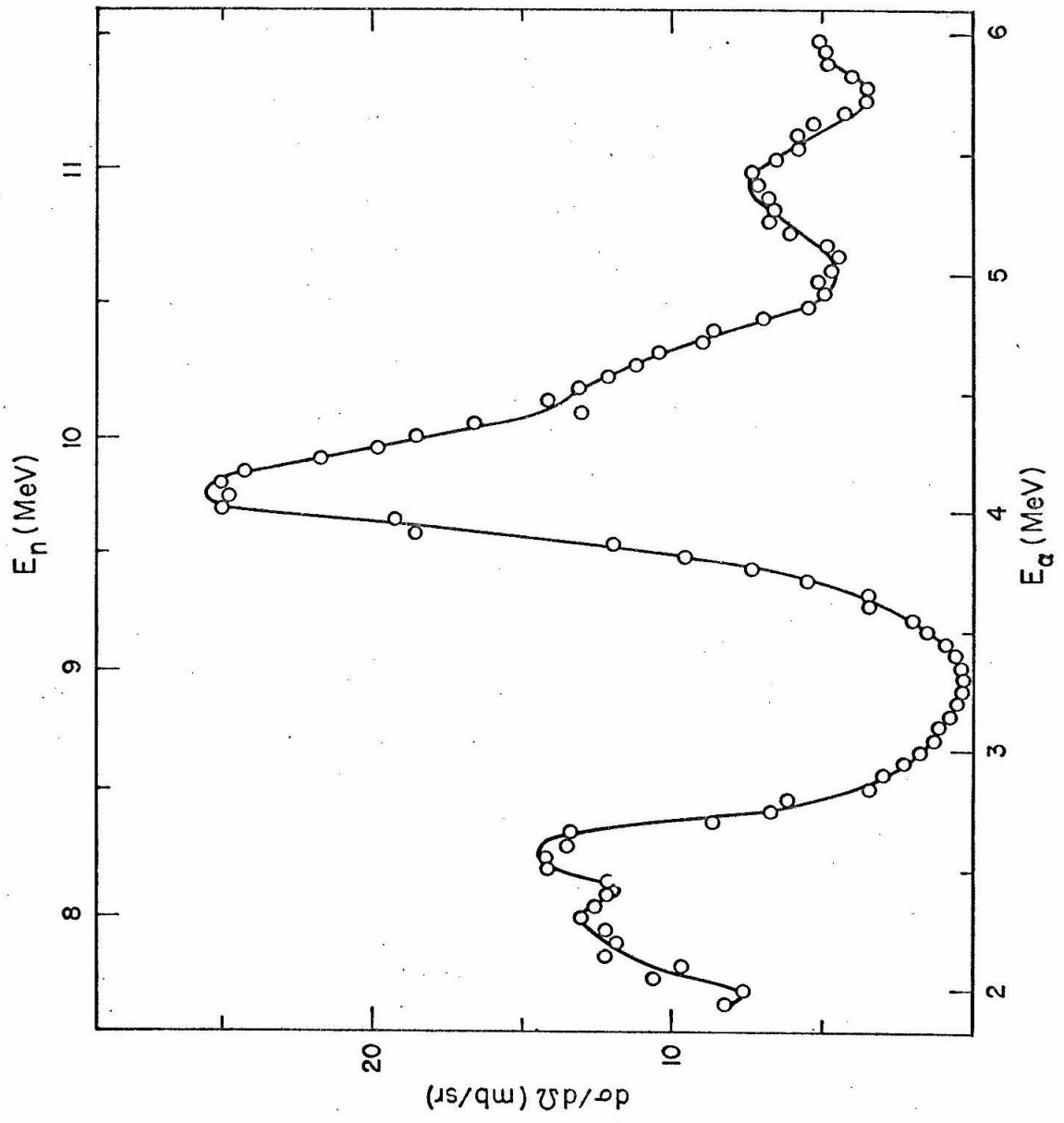

Figure 20

Pulse-height defect of the $Si^{28}(n, p_{01})$ peak as determined from a calibration based on $Si^{28}(n, \alpha)$ peaks. See page 39.

Figure 20

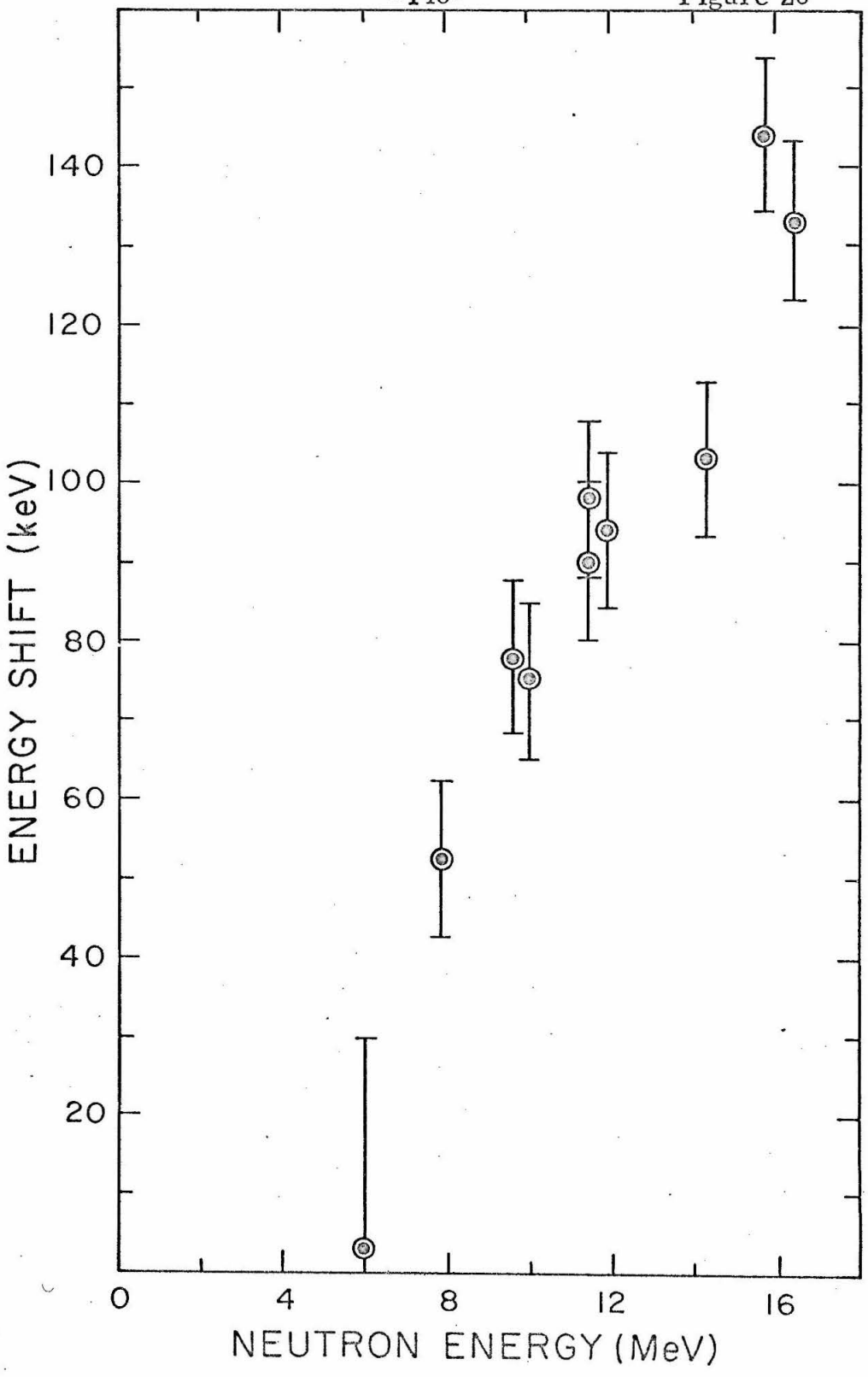
ENERGY SHIFT (keV)
140
120
100
80
60
40
20
0
4
8
12
16
NEUTRON ENERGY (MeV)

Figure 21

Thickness measurements of a Be^{9} target (top) and Fe^{54} target (bottom) performed by scattering 1-MeV protons from the tungsten backing with and without penetration through the target material evaporated on one side. The two graphs show the number of scattered protons per unit incident charge vs energy of the scattered proton, the latter being given by

$$E_p(\text{MeV}) = 0.3841(1 - E_p/(2m_pc^2))/F^2$$

where F is the magnet fluxmeter reading. The square points delineate the profile of the back side i. e., protons scattered without penetration through the evaporated material. The scattering geometry for both measurements is indicated. Note that two measurements of the Fe^{54} thickness are obtained: the shift of the W profile and the width of the peak due to protons scattered by Fe^{54} itself. These measurements were performed on the 26. 7-cm-magnetic-spectrometer station of the #1 ESG. See page 50 for further discussion of this figure.

Figure 21

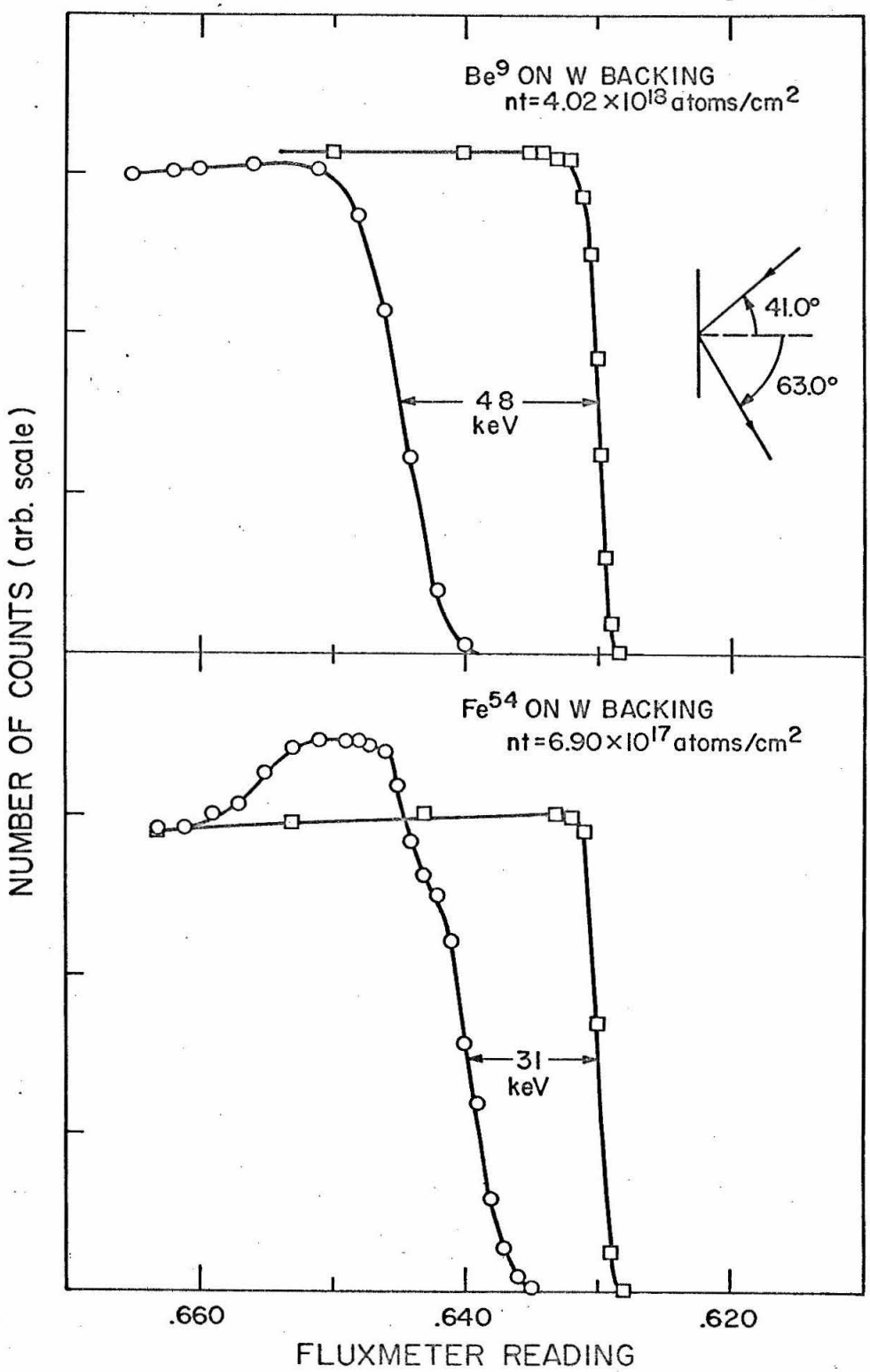
Be9 ON W BACKING
nt=4.02×10^18 atoms/cm^2
41.0°
63.0°
48
keV
Fe54 ON W BACKING
nt=6.90×10^17 atoms/cm^2
31
keV
NUMBER OF COUNTS (arb. scale)
.660
.640
.620
FLUXMETER READING

Figure 22

The reaction $Mg^{24}(He^{3}, n)Si^{26}$ at a bombarding energy of 11.60 MeV as seen in a silicon semiconductor detector at 0^{o} with respect to the beam axis. The top spectrum is the sum of several runs directly as recorded in a 400-channel analyzer. Reactions induced in the detector by the ground-state neutron are indicated by arrows. See figure 5 for the spectrum of a single monoenergetic neutron in which the peaks are correlated more clearly with the corresponding nuclear reactions in the silicon which produce them. The bottom spectrum shows the top spectrum with the best calibration obtained for the ground-state neutron normalized to it and subtracted out. Families of peaks associated with contaminants and excited states are explicitly identified. The ordinates are true numbers of counts before and after subtraction. See page 53 for a discussion of the results obtained.

Figure 22

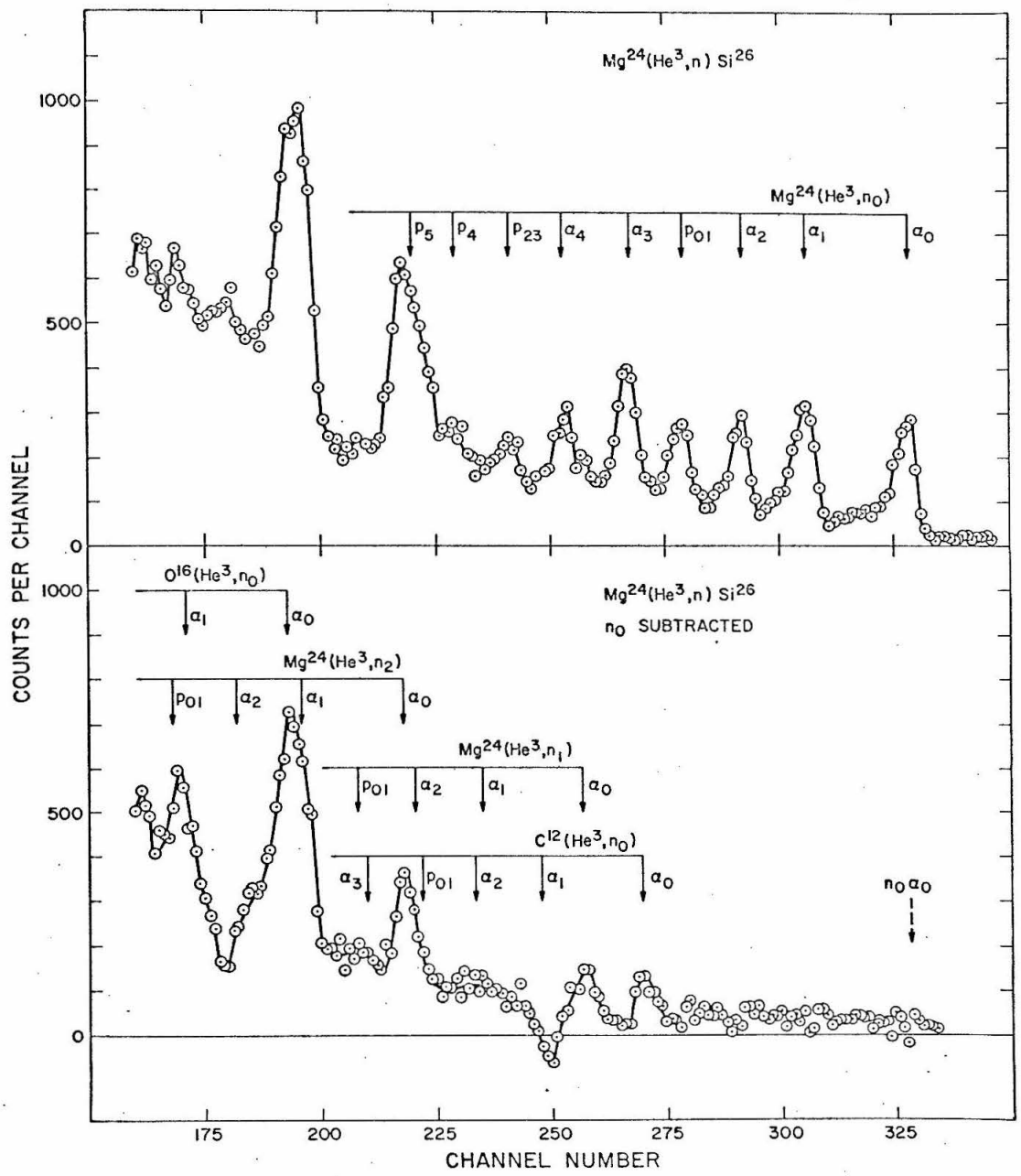
Mg24(He3,n) Si26
Mg24(He3,n0)
p5
p4
p23
α4
α3
p01
α2
α1
α0
O16(He3,n0)
Mg24(He3,n) Si26
n0 SUBTRACTED
Mg24(He3,n2)
Mg24(He3,n1)
C12(He3,n0)
n0 α0
COUNTS PER CHANNEL
CHANNEL NUMBER
1000
500
0
175
200
225
250
275
300
325

Figure 23

The reaction $Si^{28}(He^3, n)S^{30}$ as seen in a silicon detector at 0^o at a bombarding energy of 11.60 MeV. In the subtraction spectrum, the large dip just in front of the n_1-α_o peak arises in the same way as the dip in the Si^{26} spectrum (see figure 22 and the discussion of artificial dips on page 53). This spectrum, which was taken at 0^o, does not show n_1 very clearly, particularly when artifically-produced dips and rises of comparable magnitude are present. However, in spectra taken at other angles, n_1 shows up clearly even before subtraction. In fact, at 30^o, the n_1 cross section is about three times that of n_o. (See the n_o and n_1 angular distributions of figure 30.) For notation see figure 22 and for a discussion of the results see page 55.

Figure 23

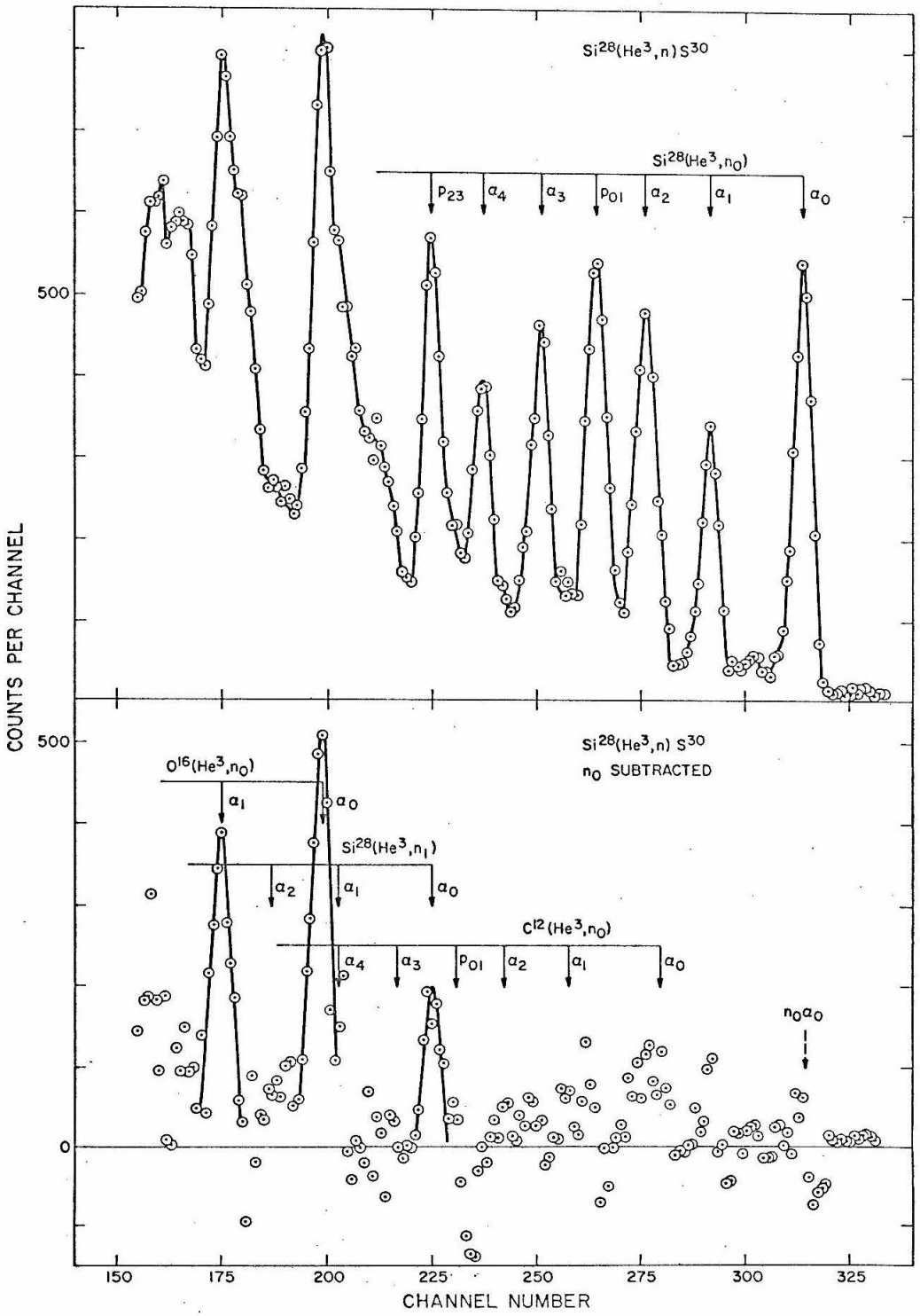
Si28(He3,n)S30
Si28(He3,n0)
p23
α4
α3
p01
α2
α1
α0
500
COUNTS PER CHANNEL
Si28(He3,n) S30
n0 SUBTRACTED
O16(He3,n0)
α1
α0
Si28(He3,n1)
α2
α1
α0
C12(He3,n0)
α4
α3
p01
α2
α1
α0
n0α0
0
150
175
200
225
250
275
300
325
CHANNEL NUMBER

Figure 24

The reaction $S^{32}(He^3, n)Ar^{34}$ as seen in a silicon detector at 0^o at a bombarding energy of 10.81 MeV. For notation, see figure 22 and, for a discussion of the results, see page 55.

Figure 24

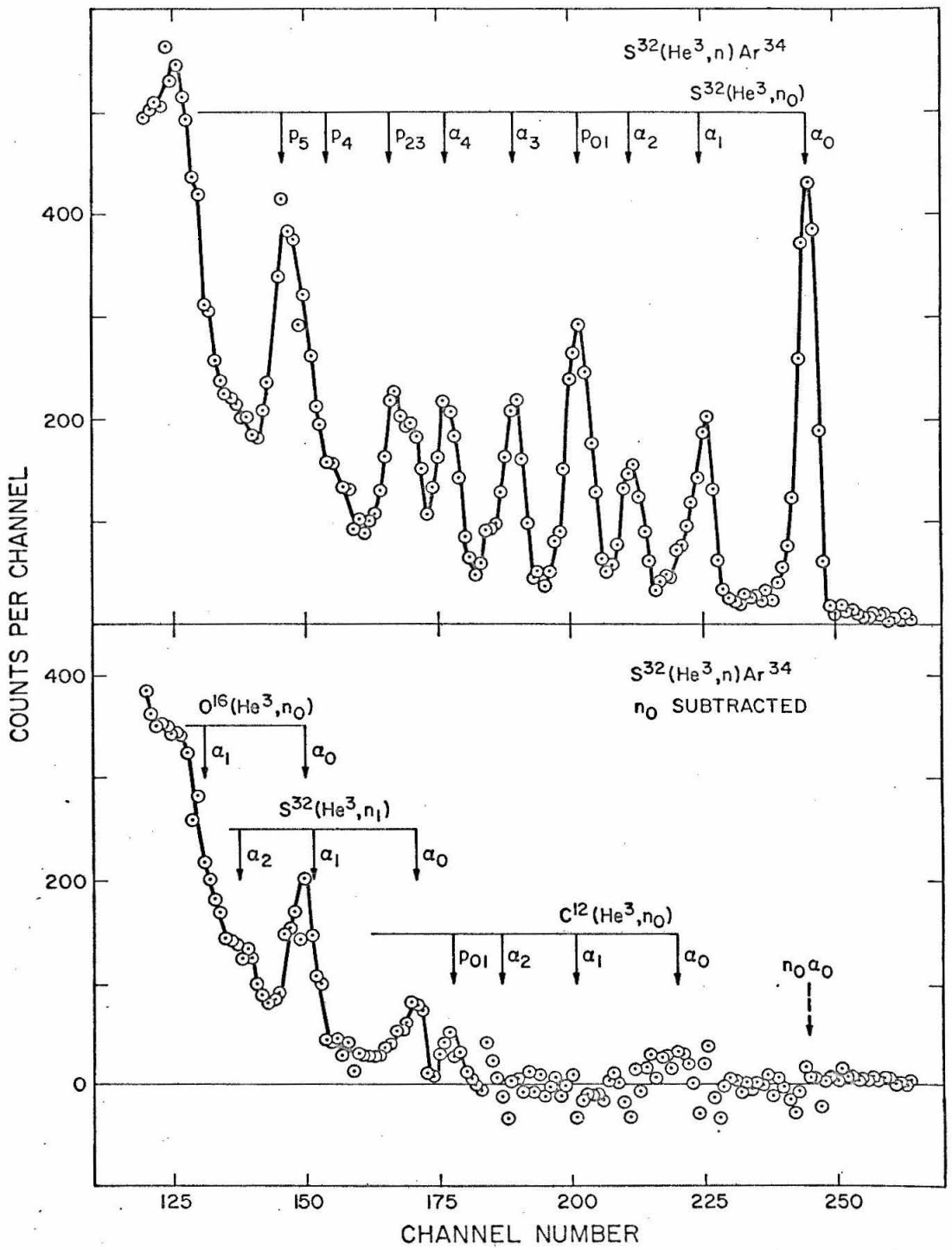
$S^{32}(He^3,n)Ar^{34}$
$S^{32}(He^3,n_0)$
p_5 p_4 p_{23} α_4 α_3 p_{01} α_2 α_1 α_0
400
200
COUNTS PER CHANNEL
$S^{32}(He^3,n)Ar^{34}$
n_0 SUBTRACTED
$O^{16}(He^3,n_0)$
α_1 α_0
$S^{32}(He^3,n_1)$
α_2 α_1 α_0
$C^{12}(He^3,n_0)$
p_{01} α_2 α_1 α_0
$n_0\alpha_0$
400
200
0
125
150
175
200
225
250
CHANNEL NUMBER

Figure 25

The reaction $Ca^{40}(He^3, n)Ti^{42}$ at a bombarding energy of 11.60 MeV as seen in a silicon detector. The upper spectrum shows the peaks produced by neutrons leading to the ground states of O^{14}, Ti^{42} and Ne^{18} with the detector at 0^o. The lower spectrum shows the same peaks with the center of the detector at 45^o, its face subtending an angle of 10^o. The kinematic shift of the $Si^{28}(n, \alpha_o)$ peaks is indicated by ΔE_k. There was about four times more carbon on the target when the lower spectrum was taken. See page 56 for a discussion of the results obtained and figure 22 for notation.

Figure 25

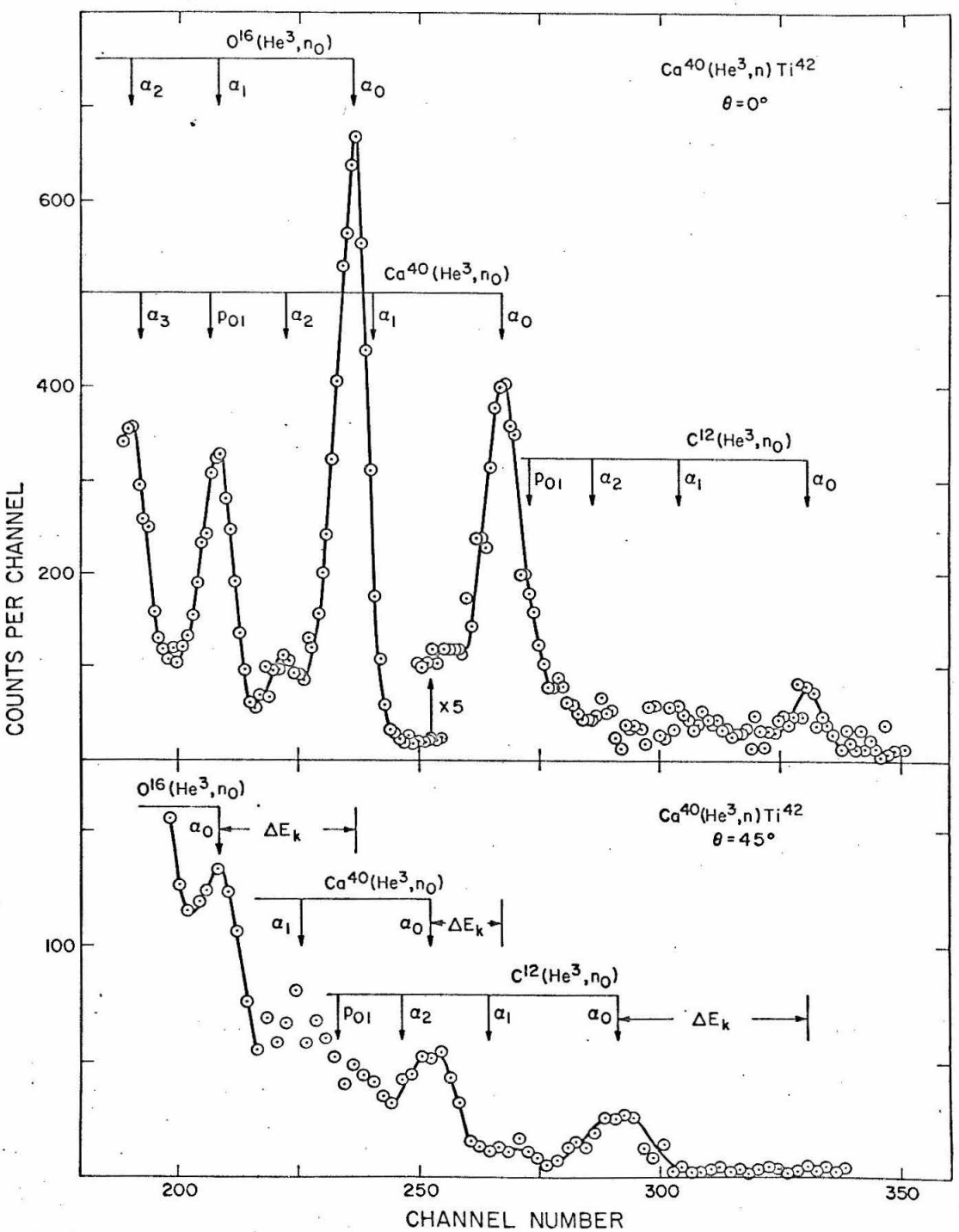
$O^{16}(He^3,n_0)$
α_2
α_1
α_0
$Ca^{40}(He^3,n)Ti^{42}$
$\theta = 0°$
600
$Ca^{40}(He^3,n_0)$
α_3
p_{01}
α_2
α_1
α_0
400
$C^{12}(He^3,n_0)$
p_{01}
α_2
α_1
α_0
200
x5
COUNTS PER CHANNEL
$O^{16}(He^3,n_0)$
α_0
ΔE_k
$Ca^{40}(He^3,n)Ti^{42}$
$\theta = 45°$
$Ca^{40}(He^3,n_0)$
α_1
α_0
ΔE_k
100
$C^{12}(He^3,n_0)$
p_{01}
α_2
α_1
α_0
ΔE_k
200
250
300
350
CHANNEL NUMBER

Figure 26

The reaction $Ti^{46}(He^3, n)Cr^{48}$ at a bombarding energy of 11.00 MeV. Note that the ground-state neutron subtraction cannot be extended below channel 255 because of the presence of groups from $Be^9(\alpha, n_1)$ in the calibration reaction. For notation see figure 22 and for a discussion of the results see page 57.

Figure 26

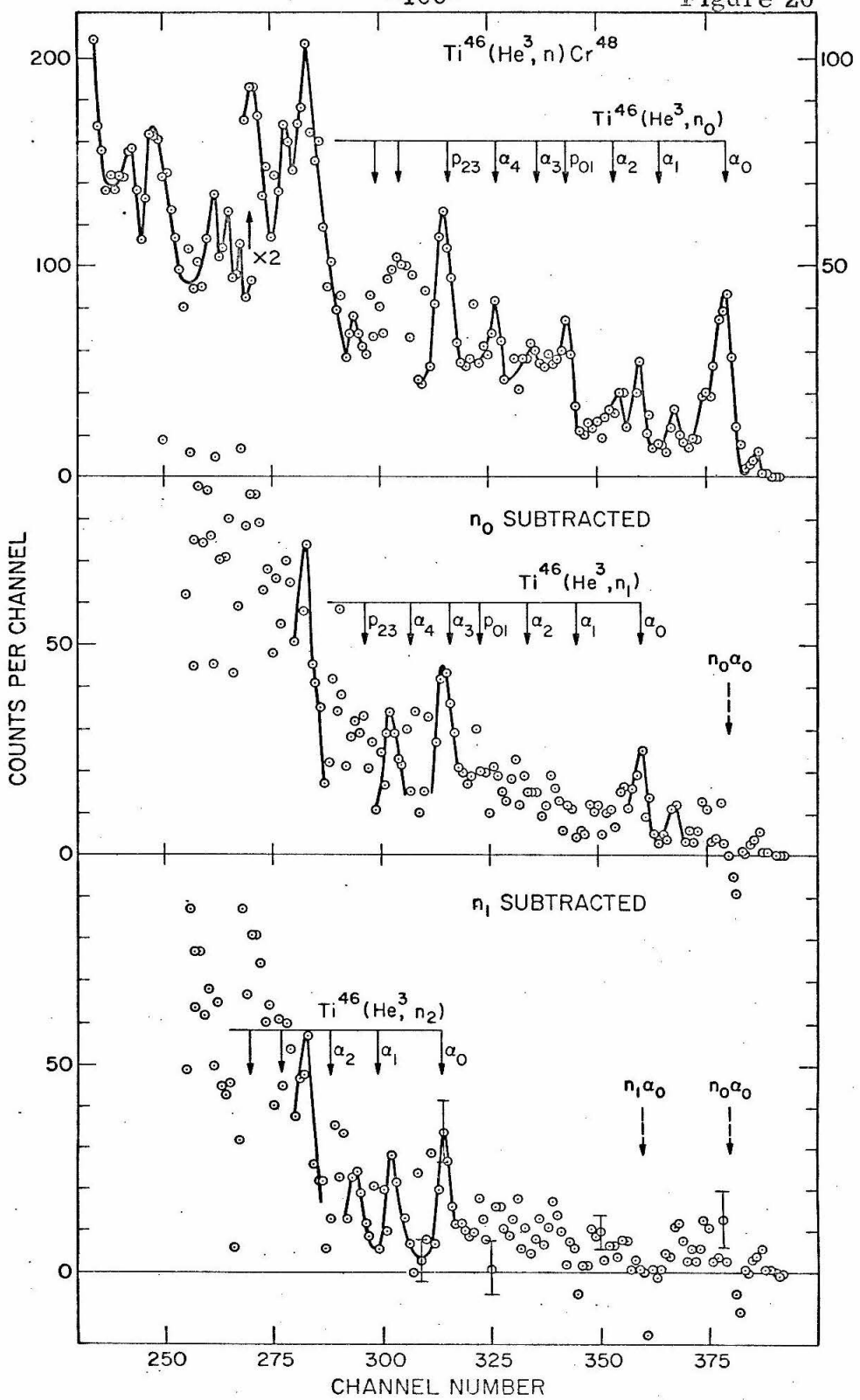
Ti46(He3, n)Cr48
Ti46(He3, n0)
p23 α4 α3 p01 α2 α1 α0
×2
n0 SUBTRACTED
Ti46(He3, n1)
n0α0
n1 SUBTRACTED
Ti46(He3 n2)
n1α0
COUNTS PER CHANNEL
CHANNEL NUMBER
200
100
0
50
250
275
300
325
350
375

Figure 27

The reaction $Fe^{54}(He^{3}, n)Ni^{56}$ at a bombarding energy of 11.51 MeV. The middle spectrum was obtained after two subtractions and the bottom after three more. Three excited states of Ni^{56} are definitely seen and there is weak evidence for two more. The α_o peaks of these latter two are indicated in the top spectrum between channels 200 and 225. The subtractions and the results obtained are discussed starting on page 59. For notation, see figure 22.

Figure 27

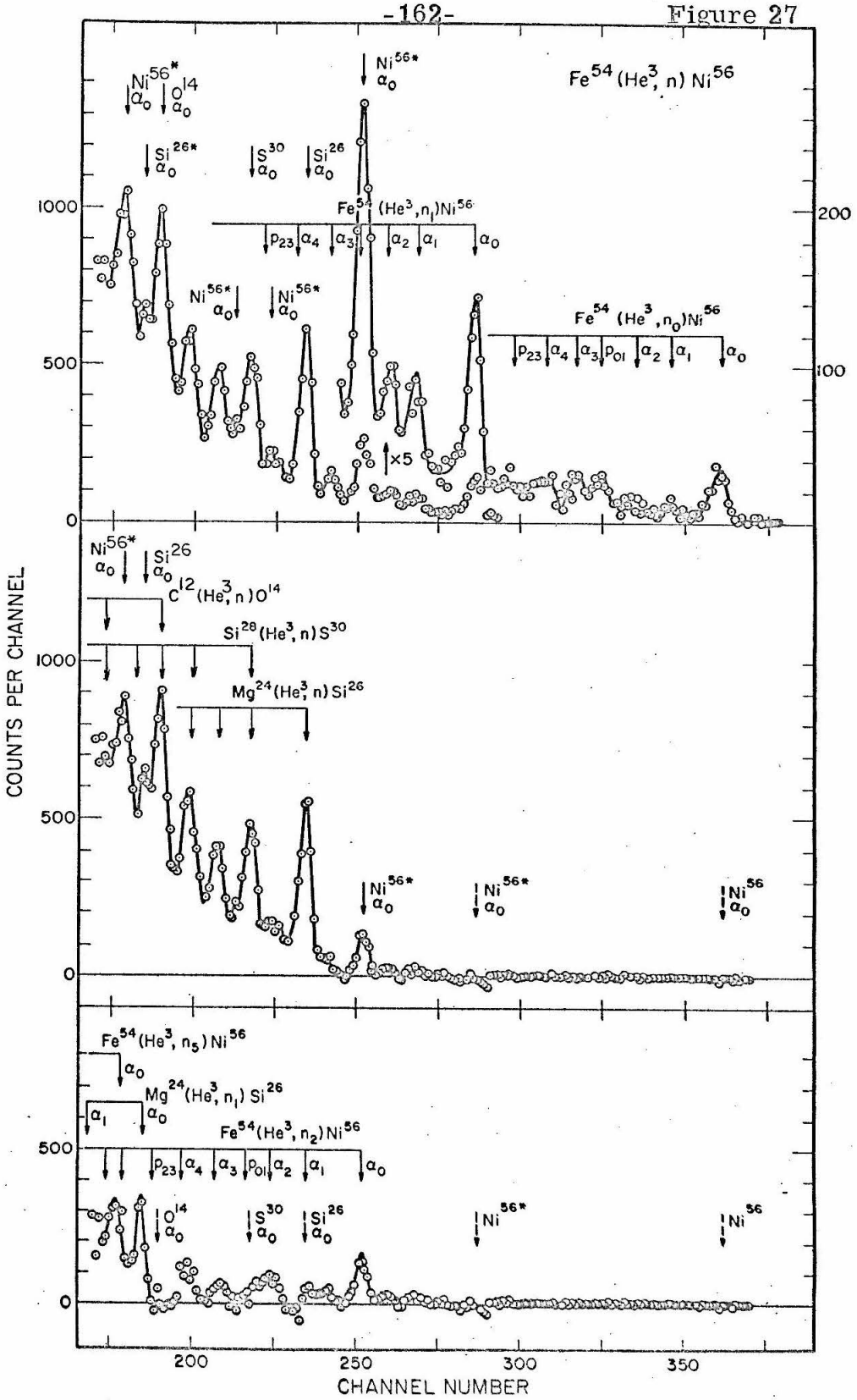
Fe54 (He3, n) Ni56
Ni56* α0
O14 α0
Si26* α0
S30 α0
Si26 α0
Fe54 (He3, n1) Ni56
p23 α4 α3 α2 α1 α0
Ni56* α0
Ni56* α0
Fe54 (He3, n0) Ni56
p23 α4 α3 p01 α2 α1 α0
×5
Ni56* α0
Si26 α0
C12 (He3, n) O14
Si28 (He3, n) S30
Mg24 (He3, n) Si26
Ni56* α0
Ni56* α0
Ni56 α0
Fe54 (He3, n5) Ni56
α0
Mg24 (He3, n1) Si26
α1
α0
Fe54 (He3, n2) Ni56
p23 α4 α3 p01 α2 α1 α0
O14 α0
S30 α0
Si26 α0
Ni56* α0
Ni56 α0
COUNTS PER CHANNEL
CHANNEL NUMBER
0
500
1000
100
200
200
250
300
350

Figure 28

All the data used for one determination of the $Ni^{58}(He^3, n)Zn^{60}$ Q value. See the next figure for the subtraction spectra. Left: The reaction $Ni^{58}(He^3, n)Zn^{60}$ at a bombarding energy of 11.60 MeV. Top right: Spectrum obtained by bombarding the target backing. The $Si^{28}(n, \alpha_0)$ peaks of (He^3, n) reactions on Mg^{24}, Si^{28} and C^{12} are identified both here and on the Zn^{60} spectrum. The magnesium and silicon accumulated on the target during the run. Bottom right: One of the $Be^9(\alpha, n_0)$ spectra used to calibrate the neutron group leading to the ground state of Zn^{60}.
See page 63 for a discussion of the results obtained.

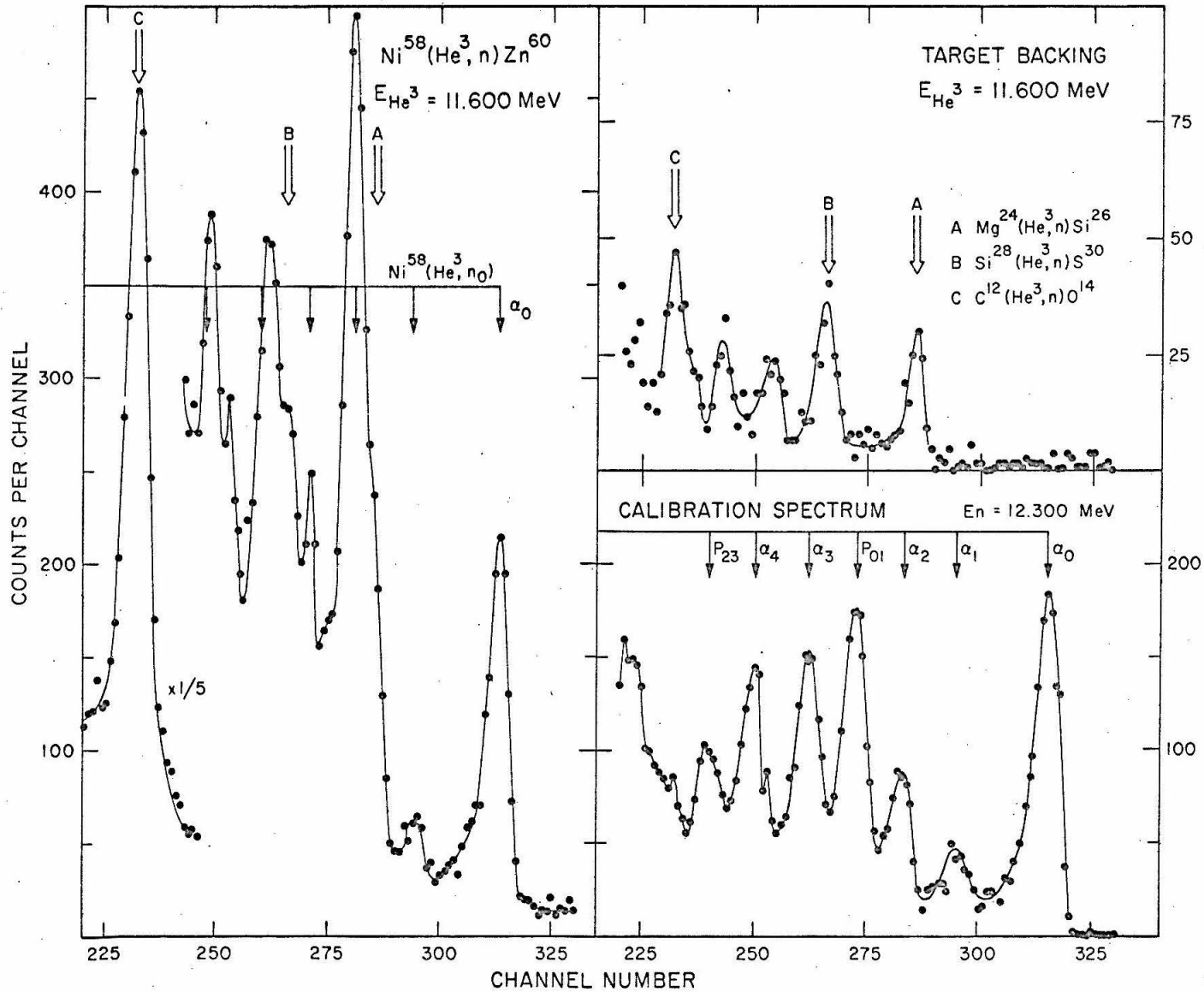
Ni58(He3, n)Zn60
EHe3 = 11.600 MeV
C
B
A
Ni58(He3, n0)
α0
x1/5
TARGET BACKING
EHe3 = 11.600 MeV
A Mg24(He3,n)Si26
B Si28(He3,n)S30
C C12(He3,n)O14
CALIBRATION SPECTRUM
En = 12.300 MeV
P23
α4
α3
P01
α2
α1
α0
COUNTS PER CHANNEL
CHANNEL NUMBER
100
200
300
400
25
50
75
225
250
275
300
325

Figure 28

Figure 29

The first excited state of Zn^{60}. See the preceding figure for the raw data. Left: Peaks remaining after subtracting the ground-state calibration spectrum. Right: Peaks remaining after subtracting the target-backing spectrum attributed to Mg and Si contaminants. The first three peaks of the $Si^{28}(n, \alpha)$ spectrum produced by the neutron group to the first excited state of Zn^{60} are clearly revealed. See page 63 for a discussion of the results obtained.

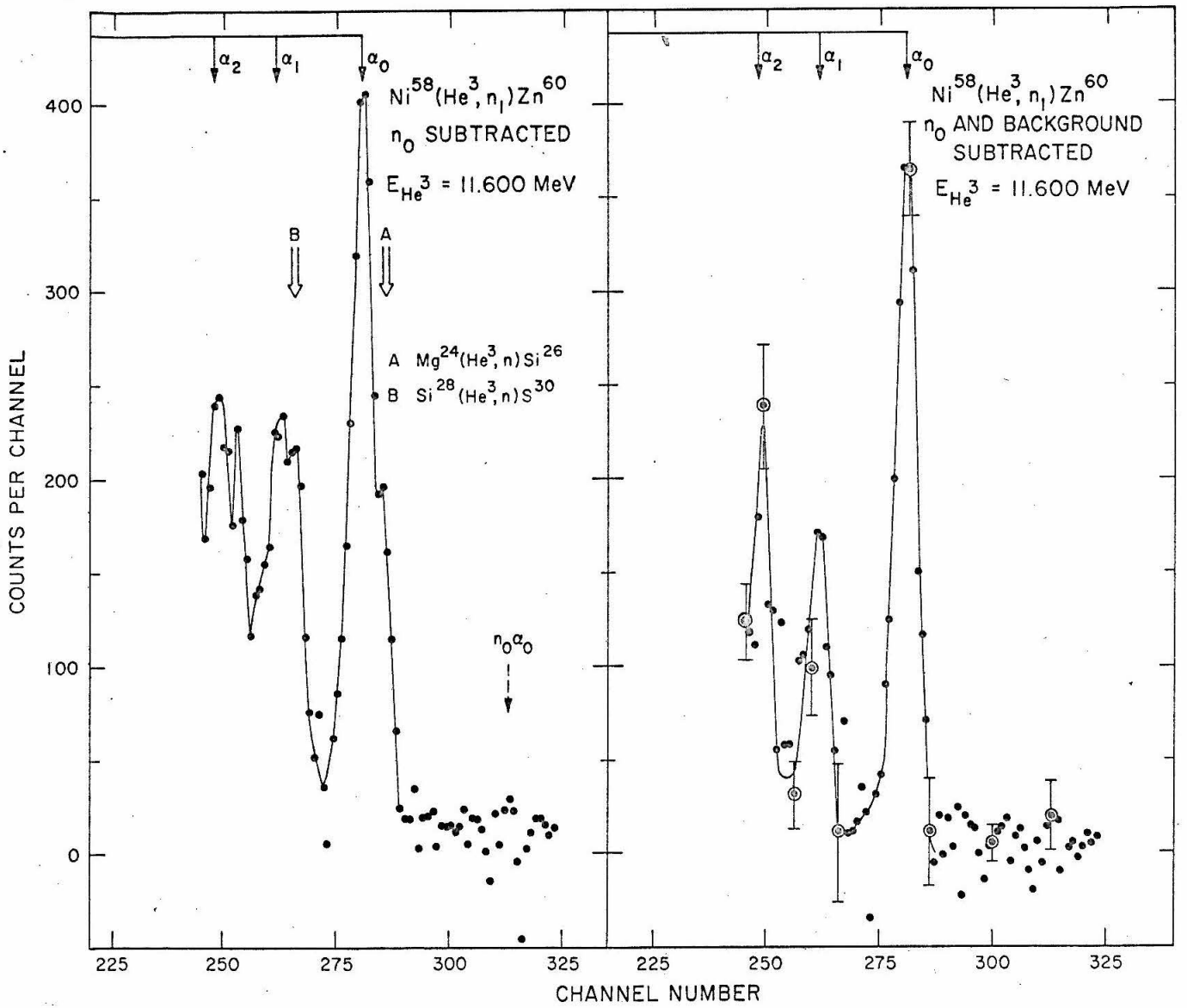
α_2
α_1
α_0
$Ni^{58}(He^3, n_1)Zn^{60}$
n_0 SUBTRACTED
E_{He^3} = 11.600 MeV
B
A
A $Mg^{24}(He^3, n)Si^{26}$
B $Si^{28}(He^3, n)S^{30}$
$n_0\alpha_0$
n_0 AND BACKGROUND SUBTRACTED
COUNTS PER CHANNEL
CHANNEL NUMBER
0
100
200
300
400
225
250
275
300
325

Figure 29

Figure 30

Angular distribution of neutrons from $Si^{28}(He^3, n)S^{30}$ to the ground and first-excited states of S^{30} measured in a semiconductor detector at a bombarding energy of 11.60 MeV. The vertical error bars are largely from uncertainty in the relative variation of the $Si^{28}(n, \alpha_0)$ cross section but also include statistical uncertainty. The horizontal lines on each point indicate the total angle subtended by the detector face. The error on the absolute cross section is 30% and the error on the relative magnitude of the ground and first-excited-state neutron yields is 20%. The solid lines are theoretical fits which assume a stripping process and use the plane-wave Born approximation with R = 5.0 fermis. See page 65.

Figure 30

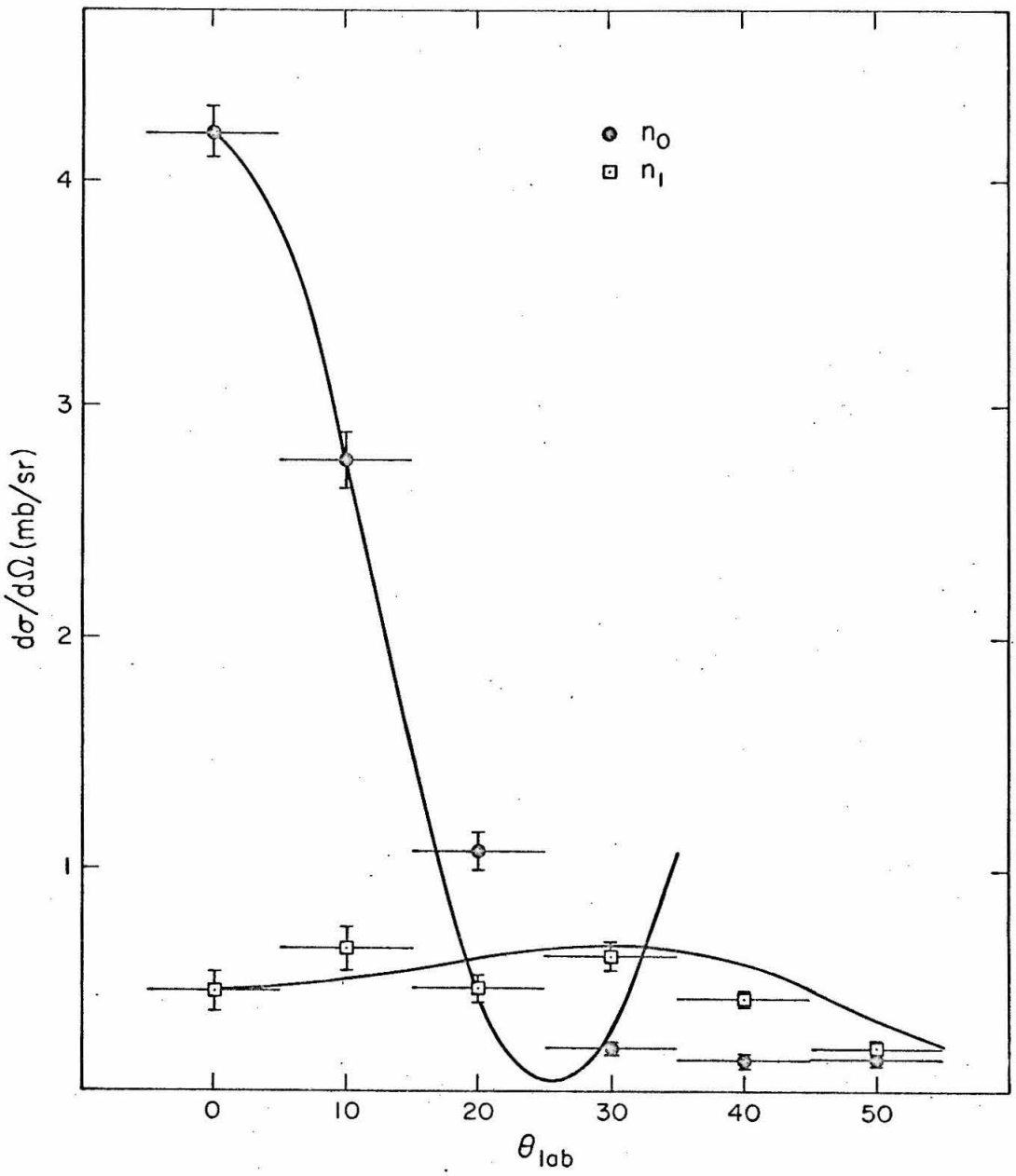

Figure 31

The proton spectrum from the reaction $Fe^{54}(He^3, p)Co^{56}$ at a bombarding energy of 11.50 MeV and laboratory angle of 15^{o}. Peaks C and E and the small peak at about 41.5 Mc did not appear at other angles. They are probably spurious peaks produced by bursts of noise in the array detectors. The remaining peaks correspond to levels in Co^{56}, except perhaps J which was not seen with certainty at other angles. See page 70 and table 9.

Figure 31

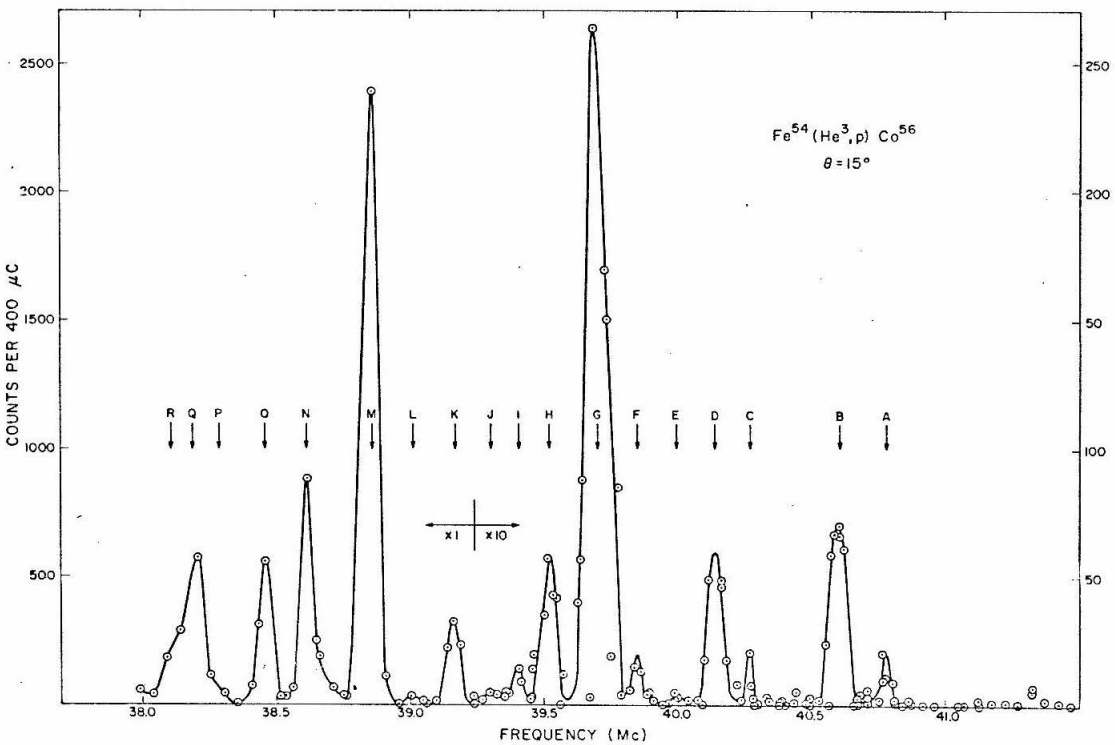
$Fe^{54}(He^3,p)\ Co^{56}$
$\theta = 15°$
COUNTS PER 400 μC
FREQUENCY (Mc)
R Q P O N M L K J I H G F E D C B A
x1 x10
2500
2000
1500
1000
500
250
200
50
100
50
38.0
38.5
39.0
39.5
40.0
40.5
41.0

Figure 32

The proton spectrum from the reaction $Ni^{58}(He^3, p)Cu^{60}$ at a bombarding energy of 11.50 MeV and laboratory angle of 15^{o}. Peaks J and Z are proton groups from the reaction $C^{12}(He^3, p)N^{14}$; peak Q is a proton group from a light target contaminant with A > 16. The remaining peaks correspond to levels in Cu^{60}. Peaks FF' are a closely-spaced doublet and peaks W may be up to 4 levels. See page 70 and table 10.

Figure 32

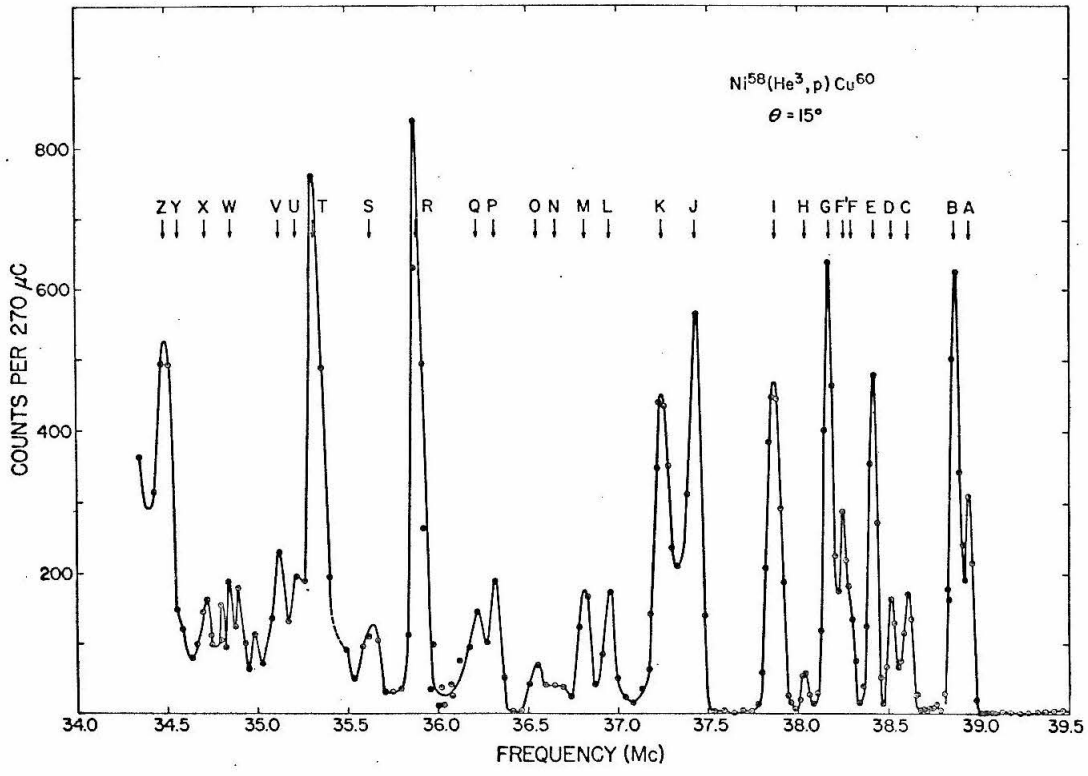
Ni58(He3,p) Cu60
θ = 15°
Z Y X W V U T S R Q P O N M L K J I H G F' F E D C B A
COUNTS PER 270 μC
800
600
400
200
34.0
34.5
35.0
35.5
36.0
36.5
37.0
37.5
38.0
38.5
39.0
39.5
FREQUENCY (Mc)

Figure 33

Summary of Q-value measurements for the mass-56 system. See pages 59-62 (Ni^{56}) and 70-71 (Co^{56}). All numbers are in MeV.

Figure 33

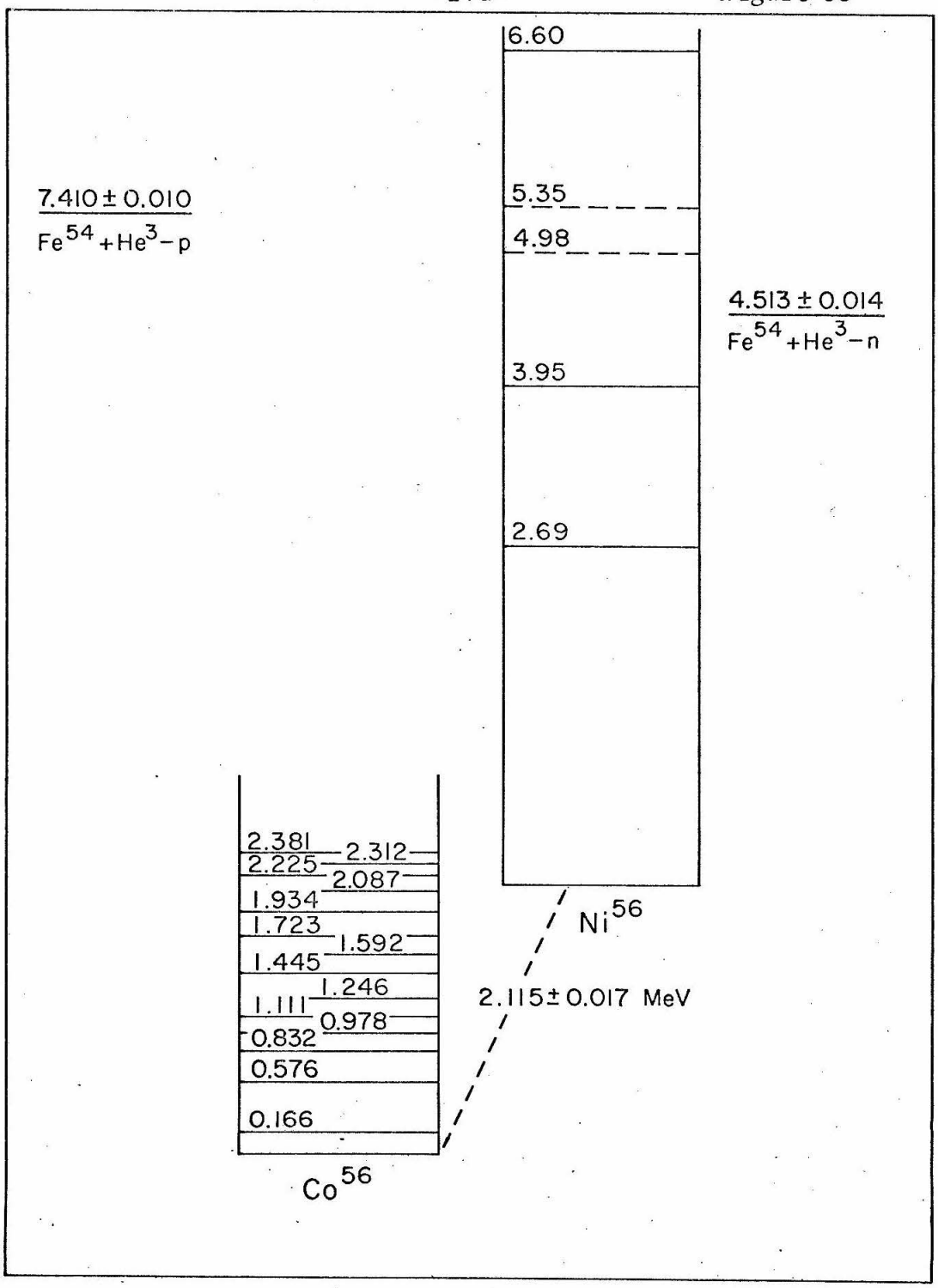
6.60
5.35
4.98
3.95
2.69
7.410 ± 0.010
Fe54 + He3 – p
4.513 ± 0.014
Fe54 + He3 – n
Ni56
2.115 ± 0.017 MeV
2.381
2.312
2.225
2.087
1.934
1.723
1.592
1.445
1.246
1.111
0.978
0.832
0.576
0.166
Co56

Figure 34

Summary of Q-value measurements for the mass-60 system. See pages 63 (Zn^{60}) and 70-72 (Cu^{60}). All numbers are in MeV.

Figure 34

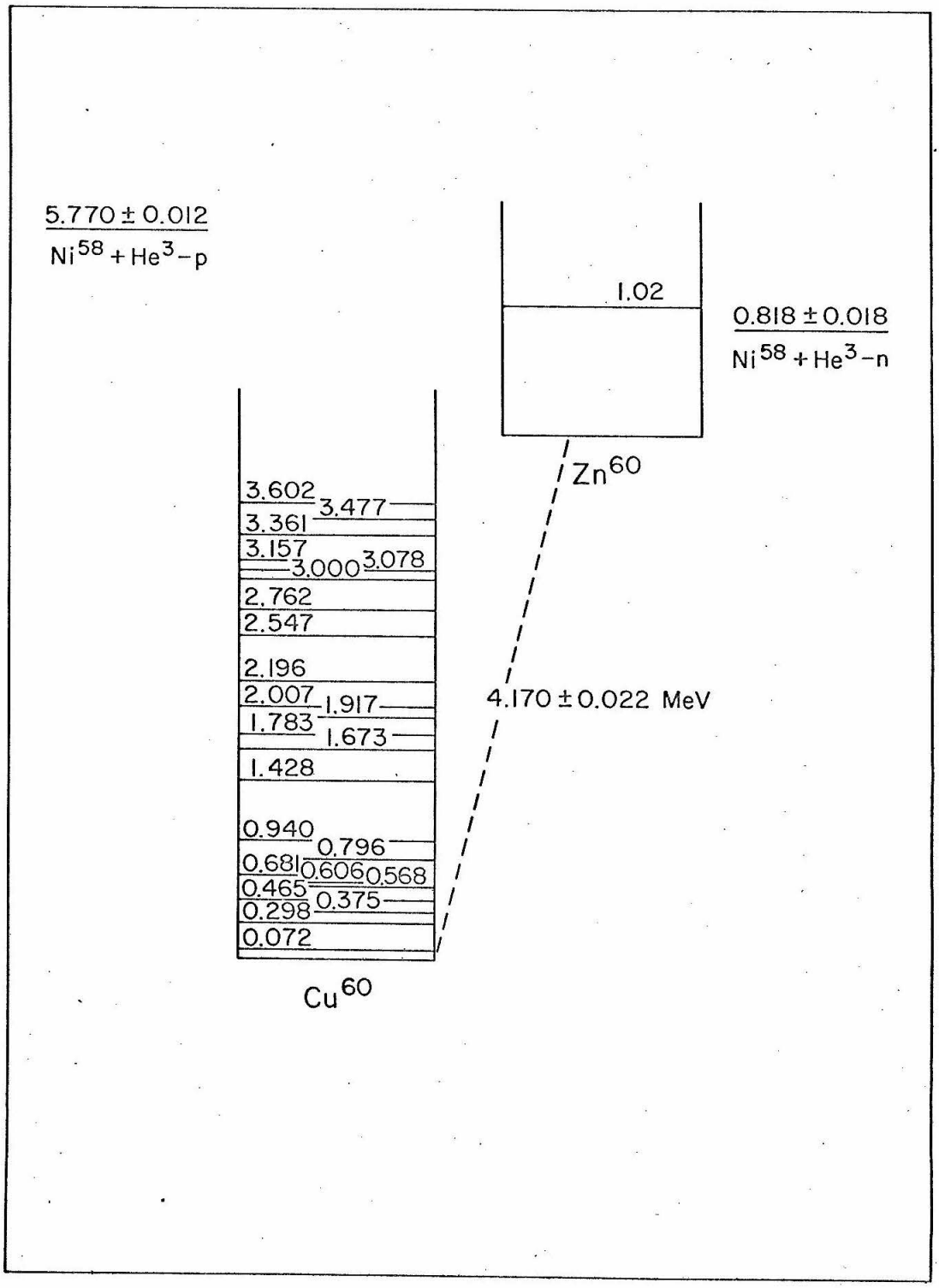
5.770 ± 0.012
Ni58 + He3 – p
1.02
0.818 ± 0.018
Ni58 + He3 – n
Zn60
3.602
3.477
3.361
3.157
3.000
3.078
2.762
2.547
2.196
2.007
1.917
1.783
1.673
1.428
0.940
0.796
0.681
0.606
0.568
0.465
0.375
0.298
0.072
4.170 ± 0.022 MeV
Cu60

Figure 35

Gamma rays seen in the first two seconds after the bombardment of Sb_2S_3 with 10-MeV He^3 summed over approximately 1000 bombardment cycles. The top curve is the total yield in the first two seconds; the bottom, the yield in the first minus the yield in the second. The following gamma rays (energies in MeV) are seen: 0.51 annihilation radiation; 1.17, 2.13, 3.30 and 4.11 all produced in S^{34} following the decay of $Cl^{34\,m}$; 1.46 and 2.62 from the decay of K^{40} and RdTh in the concrete walls of the target room; and 1.77 which may be due to the 1.77-MeV gamma ray which follows the beta decay of Al^{28} ($T_{1/2}$ = 2.28 m) to Si^{28}. The Al^{28} is presumably made by $Al^{27}(n,\gamma)Al^{28}$. See Chapter VII, section 2 (page 74) for a discussion of the results obtained from this spectrum.

Figure 35

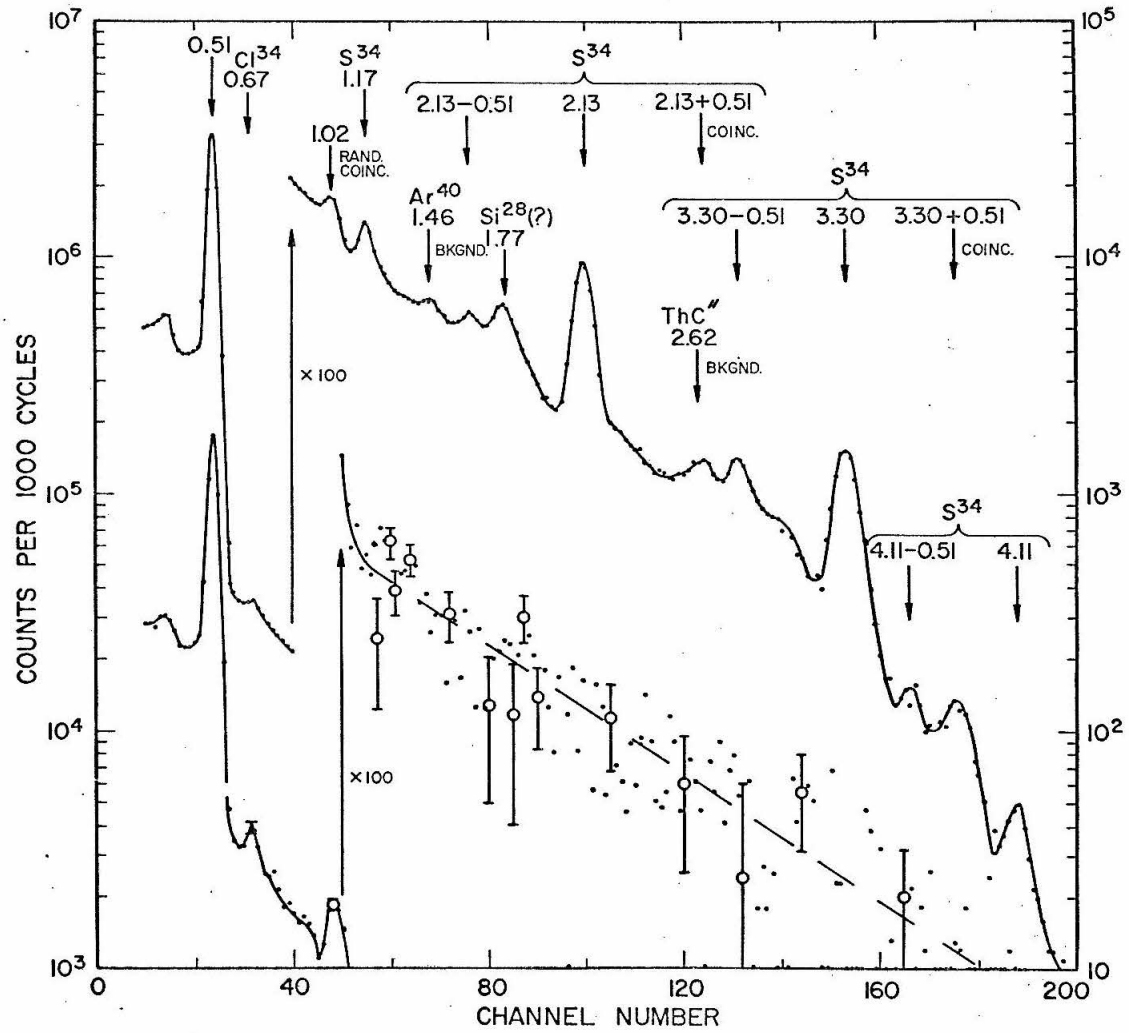
0.51
Cl34
0.67
S34
1.17
1.02
RAND. COINC.
S34
2.13−0.51
2.13
2.13+0.51
COINC.
Ar40
1.46
BKGND.
Si28(?)
1.77
S34
3.30−0.51
3.30
3.30+0.51
COINC.
ThC''
2.62
BKGND.
×100
×100
S34
4.11−0.51
4.11
COUNTS PER 1000 CYCLES
CHANNEL NUMBER
10⁷
10⁶
10⁵
10⁴
10³
10⁵
10⁴
10³
10²
10
0
40
80
120
160
200

Figure 36

The mass-34 system showing only those levels of interest to the work described here, which chiefly concerned Ar^{34} made via $S^{32}(He^3, n)Ar^{34}$. See page 55 for a description of the Q-value measurements of the ground and first-excited states of Ar^{34}, and pages 74-77 for the measurement of the positron branch to the 0.67-MeV level of Cl^{34} and the relative intensities of the gamma rays following the beta decay of $Cl^{34\,m}(0.143)$.

Figure 36

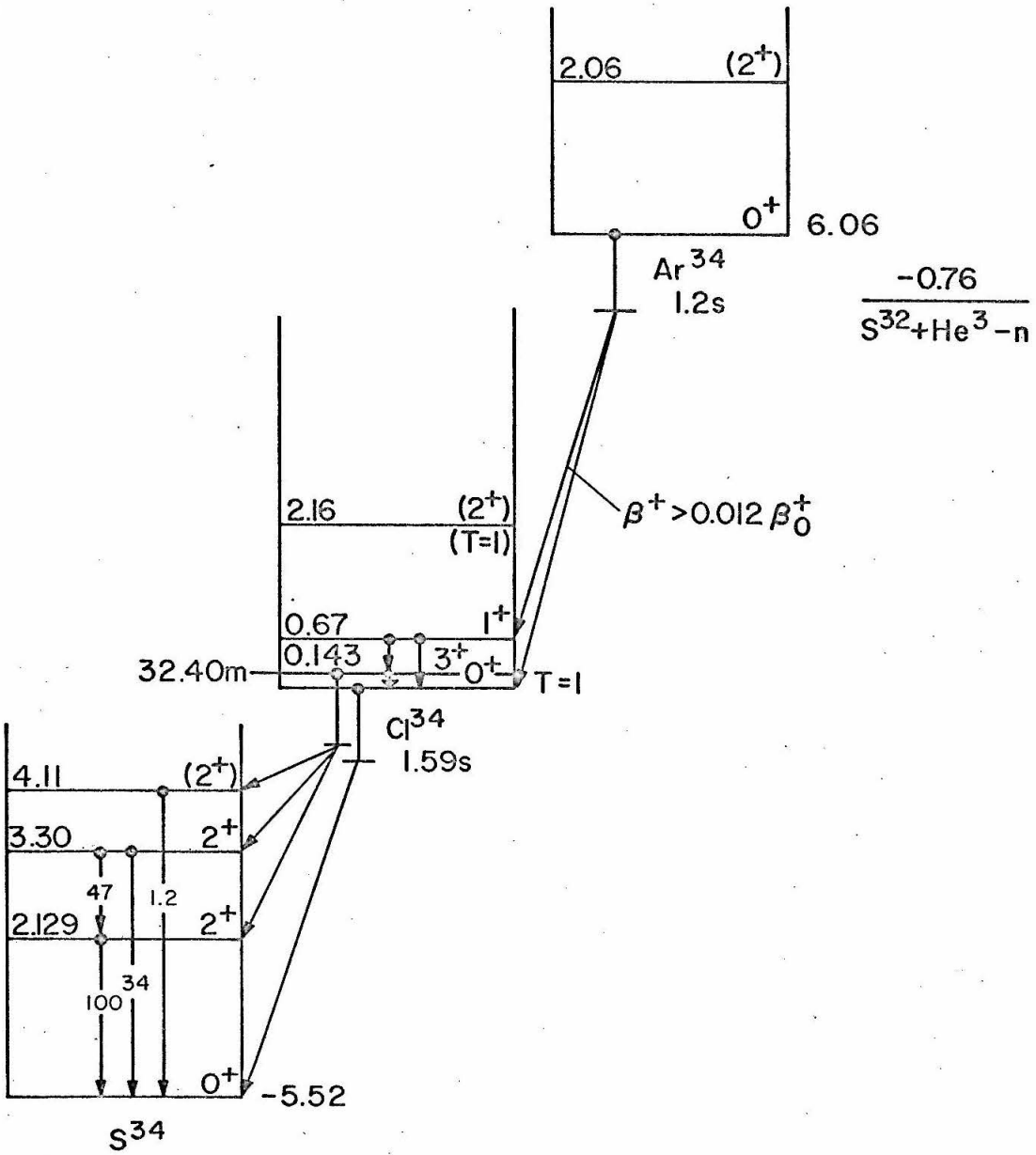
2.06
(2+)
0+
6.06
Ar34
1.2s
-0.76
S32+He3-n
2.16
(2+)
(T=1)
β+ >0.012 β+0
0.67
1+
0.143
3+
0+
32.40m
T=1
Cl34
1.59s
4.11
(2+)
3.30
2+
47
1.2
2.129
2+
100
34
0+
-5.52
S34

Figure 37

Gamma-ray spectrum observed in coincidence with neutrons from the reaction $Fe^{54}(He^3, n\gamma)Ni^{56}$. Peaks are seen corresponding to gamma rays of energy 1.28 ± 0.06 MeV and 2.66 ± 0.10 MeV. The apparent peak in channel 46 ($E_\gamma = 3.47 \pm 0.13$ MeV) is not statistically significant and, if it exists, does not correspond to a transition between known levels of Ni^{56}. See page 77.

Figure 37

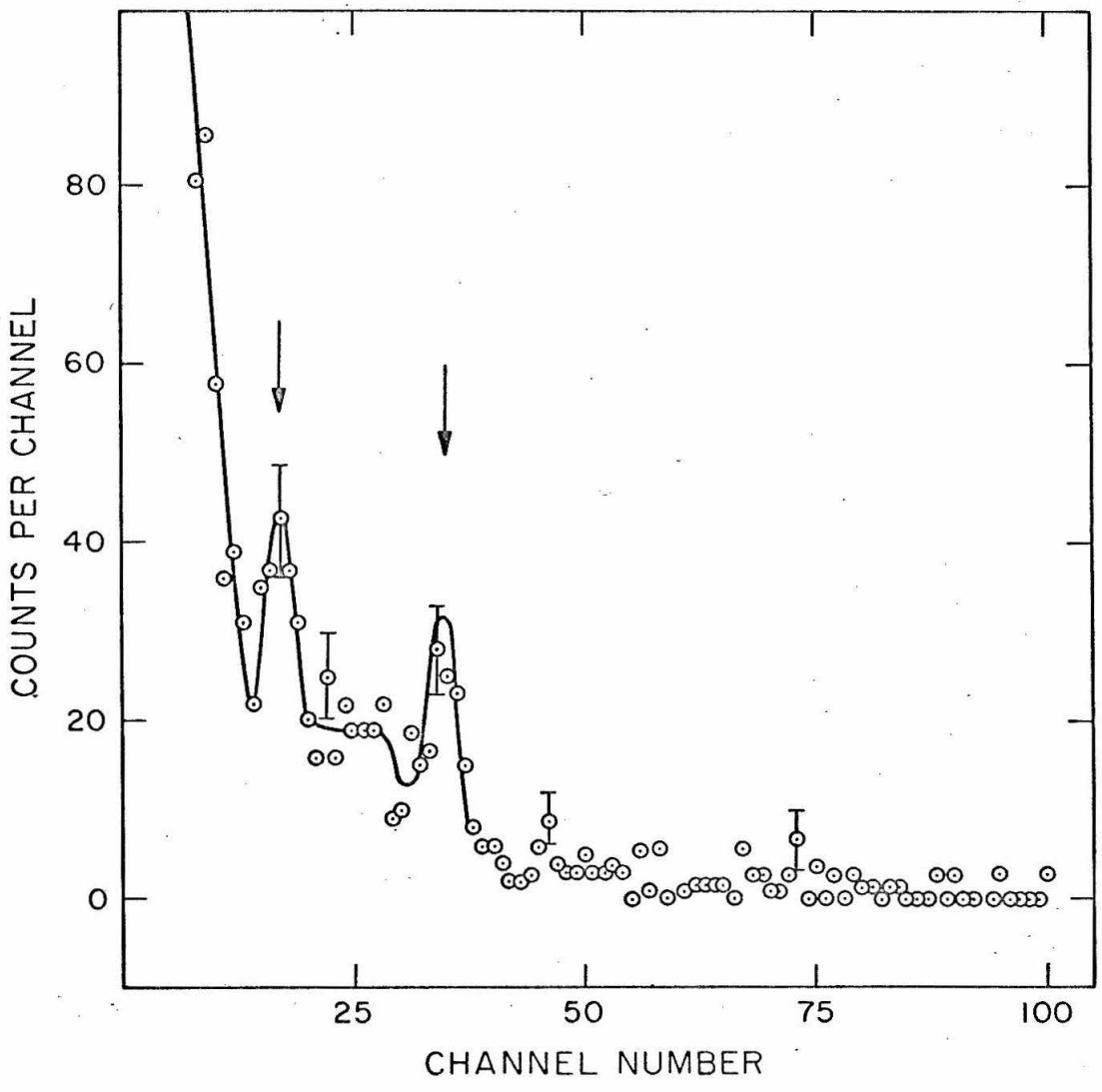

Figure 38

Known levels of Ni^{56} separated into a vibrational band built on the ground state and a vibrational or rotational band built on the state at 3.95 MeV. Evidence in favor of this interpretation is given on pages 78 and 79.

Figure 38

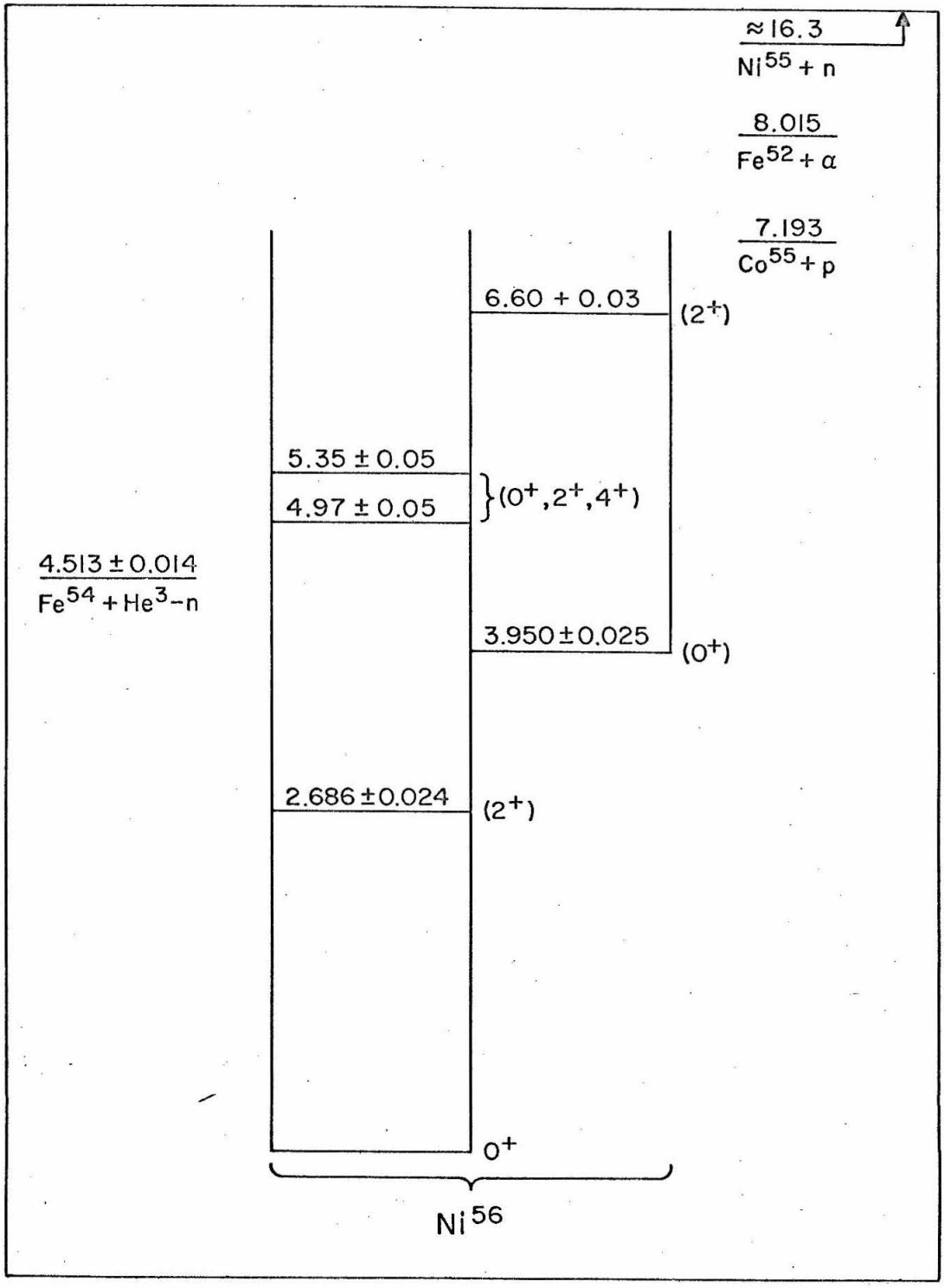
≈16.3
Ni55 + n
8.015
Fe52 + α
7.193
Co55 + p
6.60 + 0.03
(2+)
5.35 ± 0.05
4.97 ± 0.05
(0+,2+,4+)
4.513 ± 0.014
Fe54 + He3 - n
3.950 ± 0.025
(0+)
2.686 ± 0.024
(2+)
0+
Ni56

Figure 39

Left: Energy levels of Ca^{40} below 8.6 MeV.

Center: Levels in the proposed rotational band with their energies redefined with respect to the 0^+, 3.38 MeV level (see page 79). Experimental errors are given. The error on the 7.12-MeV state is an estimate of the error in the data of Bauer et al. (1965); the remaining errors are those quoted by Braams (1956).

Right: The rotational spectrum calculated from $E(J) = 0.092\,J(J+1)$ MeV.

Figure 39

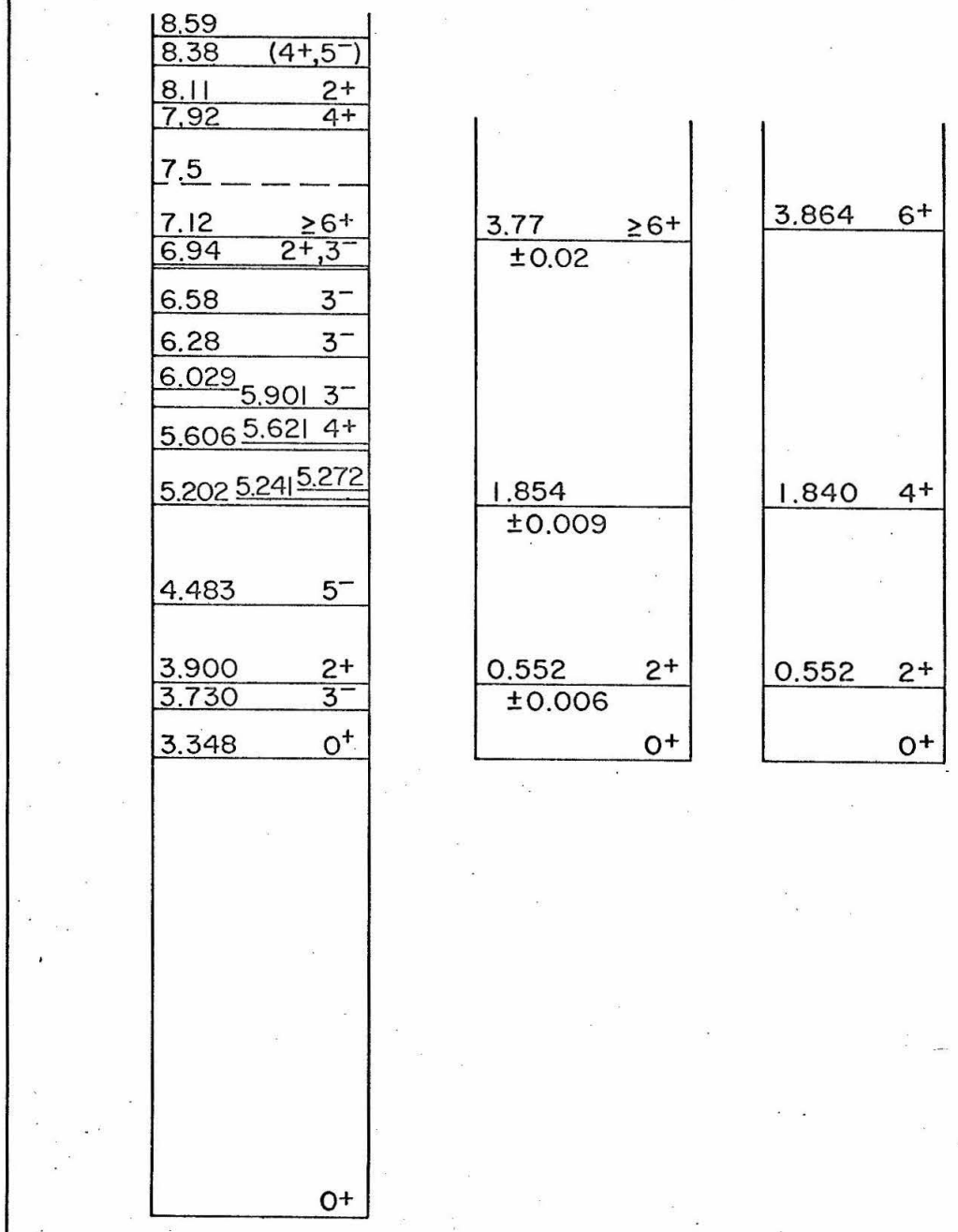
8.59
8.38 (4+,5−)
8.11 2+
7.92 4+
7.5
7.12 ≥6+
6.94 2+,3−
6.58 3−
6.28 3−
6.029
5.901 3−
5.606 5.621 4+
5.202 5.241 5.272
4.483 5−
3.900 2+
3.730 3−
3.348 0+
0+
Ca40
3.77 ≥6+
±0.02
1.854
±0.009
0.552 2+
±0.006
0+
3.864 6+
1.840 4+
0.552 2+
0+

Figure 40

Negative ion current at the LET vs 20^{o} magnet current measured with a mixture of 93% H_2 and 7% O_2 in the source, and H_2 in the exchange canal. The ion source controls were adjusted to maximize the beam labelled O^+/O^-. Useful oxygen beams have been obtained from the three broad peaks explicitly identified as being oxygen. Each peak is seen to have considerable fine structure, probably due to different combinations of oxygen and hydrogen. The maximum probable range for such structure is indicated for O^o/O^- and O^+/O^- peaks. See page 86.

The energies indicated on the graph were measured with an electrostatic analyzer.

The dotted curves are helium peaks found with a 50-50 mixture of He and O_2 in the source and H_2 in the exchange canal.

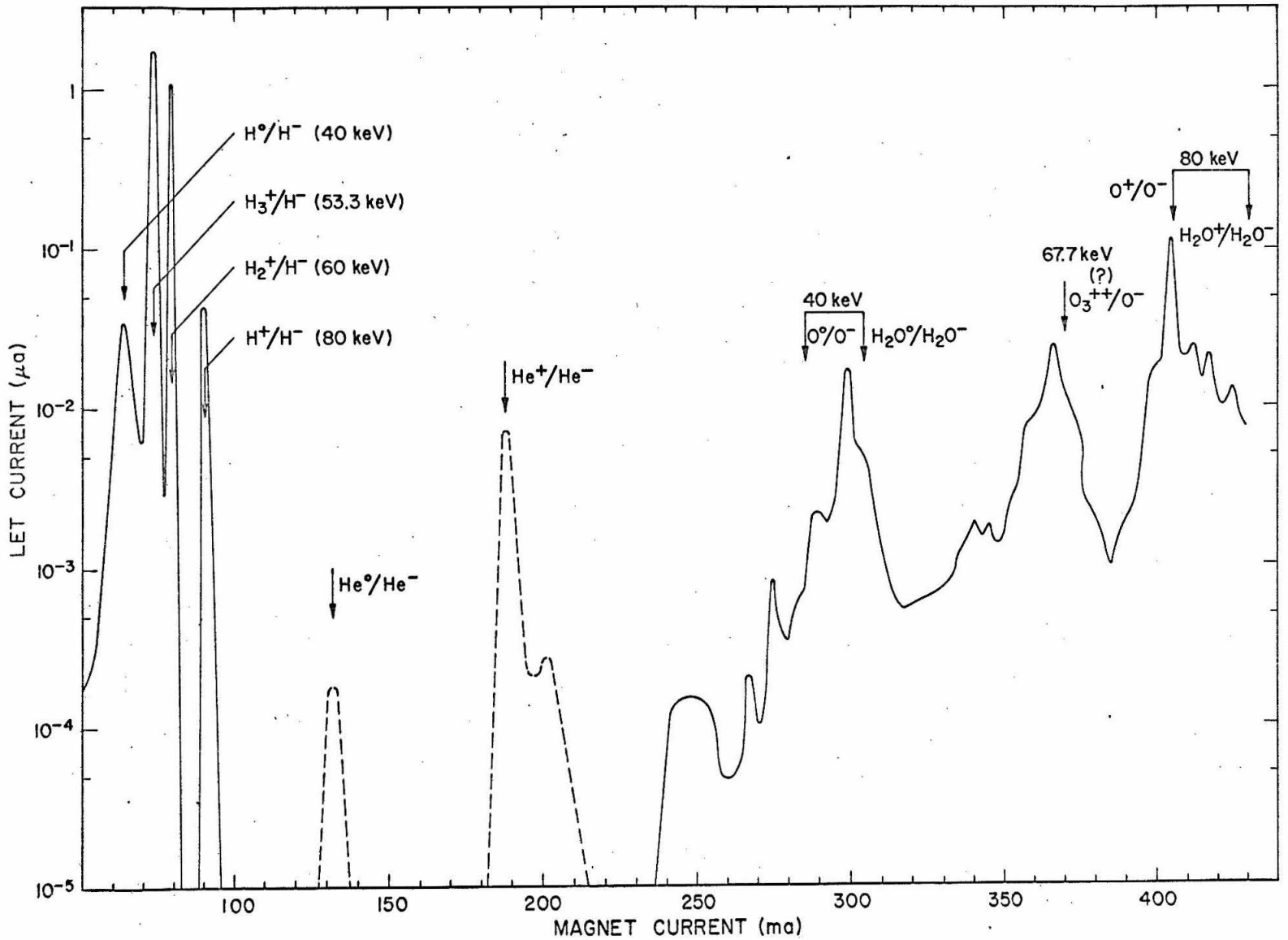
LET CURRENT (μa)
1
10⁻¹
10⁻²
10⁻³
10⁻⁴
10⁻⁵
100
150
200
250
300
350
400
MAGNET CURRENT (ma)
H°/H⁻ (40 keV)
H₃⁺/H⁻ (53.3 keV)
H₂⁺/H⁻ (60 keV)
H⁺/H⁻ (80 keV)
He°/He⁻
He⁺/He⁻
40 keV
O°/O⁻
H₂O°/H₂O⁻
67.7 keV
(?)
O₃⁺⁺/O⁻
80 keV
O⁺/O⁻
H₂O⁺/H₂O⁻

Figure 40

Figure 41

Energy spectrum of particles scattered through 30^{o} from a gold foil as seen in a semiconductor detector. The tandem was regulating on the S^{7+} beam and the terminal voltage was 5.30 MeV. See text (page 88) for explanation of the remaining peaks.

Figure 41

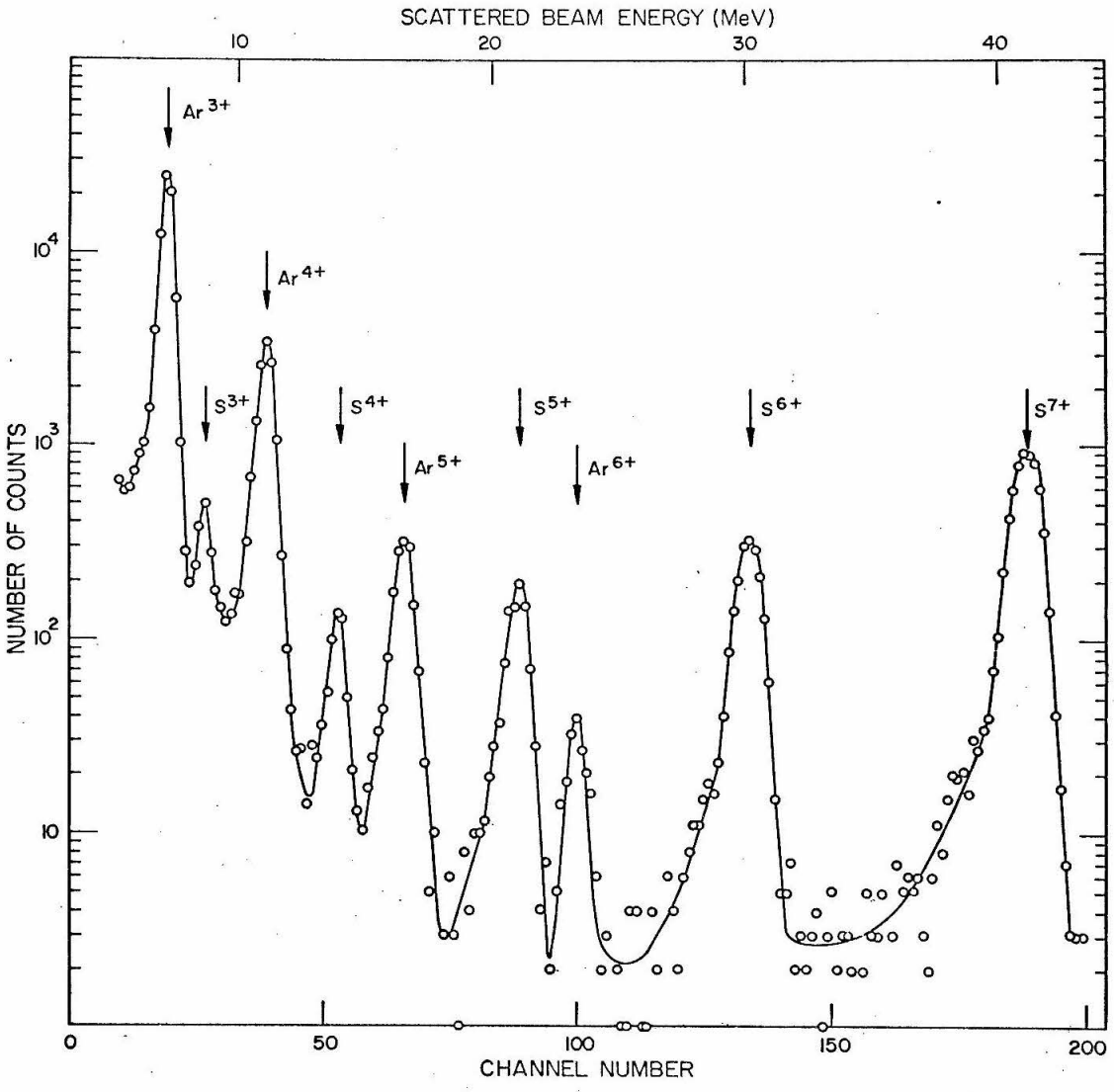
SCATTERED BEAM ENERGY (MeV)
10
20
30
40
Ar 3+
Ar 4+
S 3+
S 4+
Ar 5+
S 5+
Ar 6+
S 6+
S 7+
NUMBER OF COUNTS
10^4
10^3
10^2
10
0
50
100
150
200
CHANNEL NUMBER